Origin of the thermal structure recorded in metamorphic rocks of SW Japan: shear heating along the MTL and large-scale folding in the Sanbagawa belt

（西南日本に分布する変成岩に記録された温度構造の成因：
中央構造線の剪断熱と三波川帯の大規模褶曲）

MORI, Hiroshi

（森　宏）

A dissertation for the degree of Doctor of Science
Department of Earth and Environmental Sciences,
Graduate School of Environmental Studies, Nagoya University
（名古屋大学大学院環境学研究科地球環境科学専攻学位論文　博士（理学））

2014

CONTENTS

OVERVIEW

Oceanic plates flow into the mantle at convergent plate margins. This convergence causes surface and subsurface materials of the oceanic plate to subduct and undergo burial at relatively low thermal gradients. The presence of subduction type metamorphic domains shows that this once deeply buried material can return to the earth's surface representing large-scale cycling of rocks from the surface to depths of 100 km or more and back to the surface. They are also the site of the largest fault-generated earthquakes due to displacement along the subduction boundary and related large faults. These first-order geological phenomena are strongly affected by the thermal structure. Recent advances in our understanding of the thermal structure of subduction zones has been achieved both through an increase in the amount and precision of geophysical data and in particular through the increase in computing power. However, there are still considerable uncertainties in several of the key input parameters required for modeling.

One approach to improving the accuracy of thermal models is to incorporate information from metamorphic rocks. Studies of these rocks can reveal the *P–T* conditions occurring the deep inaccessible regions of subduction zones. However these metamorphic rocks generally undergo deformation during exhumation from their original location to the earth's surface. This deformation can strongly alter the original thermal structure. Therefore, knowledge of the late stage deformation of subduction metamorphic belts is important in to reconstruct the relationship between the present thermal structure and the original arrangement in the subduction zone.

One of the major unknowns in the thermal modeling of the subduction zones is the affect of shear heating—in other words the importance of heat generated by deformation. Estimates of shear stresses acting on plate boundaries vary from about 0 MPa to 100 MPa. This range corresponds to differences of several hundreds of degrees in the temperature estimated along the subduction boundary. The uncertainties in shear heating represent a general lack of consensus concerning the strength of large-scale faults. Metamorphic rocks exposed around major faults undergo deformation at a range of different depths in the crust. The ductile to brittle transition zone is expected to be the region where the rocks will exhibit the maximum strength and therefore be associated with the largest amount shear heating.

In this thesis I present the results of a combination of structural and petrological

analyses of metamorphic rocks that contribute to the debate about how to reconstruct the thermal structure from metamorphic rocks and the importance of shear heating. These results are augmented by thermal modeling.

In Part 1, I focus on deformation of the high-grade part of the Sanbagawa metamorphic belt. In order to use the *P–T* conditions of metamorphic belts to reconstruct the thermal structure where they formed, it is first necessary to examine the effects of deformation that occurred after the peak of metamorphism.

The Sanbagawa belt is a regionally coherent belt of subduction type metamorphism that formed in the mid-Cretaceous. High-pressure metamorphic rocks formed at mantle depths in a subduction zone are widely distributed in central Shikoku, and detailed studies for the estimations of peak metamorphism (peak temperature and the associated pressure) have been conducted in this region. These data show higher metamorphic grade is generally located at higher structural levels increasing towards ultramafic rocks originated in the overlying wedge mantle. Therefore, the thermal structure of the Sanbagawa belt may preserve the thermal structure formed within the slab. However, repetitions in the distribution of the metamorphic zones seen in central Shikoku clearly show the original thermal structure has also been affected by deformation after the peak of metamorphism. The Asemi-gawa section in central Shikoku lies roughly perpendicular to metamorphic zonation, and therefore is one of the key areas for looking at the large-scale structure of the Sanbagawa belt and its relationships to the metamorphism. Although the Asemi-gawa region has been the focus of many detailed studies, the cause of the metamorphic repetition, which causes the highest-grade units to be located at intermediate structural levels, has been interpreted both in terms of a large-scale recumbent fold and thrusting, and there is no good consensus for them. It is important to know how to relate the present structural sequence to the original arrangement in the subduction zone. I conducted a detailed structural analysis of the area including highest-grade zones to test the hypothesis that a large-scale fold exists in this area. I also expended this work to examine the large-scale structure of the high-grade Sanbagawa belt as a whole.

I conducted a field survey covering an area of about 3.5 km in a north-south direction and 7 km in the east-west direction. The area shows a well-developed schistosity and an east-west trending mineral lineation, which were formed during the

Ds deformation that took place during the exhumation of the Sanbagawa rocks. Folding structures formed by *Ds* and post-*Ds* (*Dt* and *Du*) are observed and these mainly have east-west trending axes. Two types of observations proved useful in helping to test the idea that the region contains a kilometer-scale fold: (1) the lithological boundary between basic and quartz schists as an indication of the original younging direction, and (2) the vergence of meter-scale *Ds*-folds. Major changes in the sense of asymmetry indicated by both types of observations occur at a thick east-west trending basic schist layer in the central level of the study area. These results clearly indicate the existence of a large-scale fold formed by *Ds* deformation with a north downward closure. The location of the fold axis corresponds to the inversion axis of the metamorphic zonation, and is in good agreement with the recumbent fold hypothesis, proposed to account for the structure of the Asemi-gawa area. Microstructural evidence shows this folding took place during *Ds* and caused inversion of the original thermal structure. Similar large-scale folds have also been reported in other areas of the Sanbagawa belt in central Shikoku, and constructing a series of cross-sections shows these structures can be continuously traced through the Sanbagawa belt. I constructed a three-dimensional diagram to illustrate the proposed fold structures in central Shikoku. This type of structural analysis can be used to help reconstruct the original thermal structure of the subduction zone from the recorded *P–T* conditions.

In Part 2, the Median Tectonic Line (MTL) is a key tectonic element in the geological evolution of SW Japan. It is also the largest on-land fault of the Japanese islands and a good candidate to examine the thermal effects of slip along large-scale long-lived faults. I report the results of new estimations of the peak metamorphic temperatures in the Sanbagawa belt nearby the MTL by using Raman carbonaceous geothermometry. The aim of this study was to detect and quantify any shear heating around this fault. I also discuss the fault strength by comparing the results with thermal modeling and assess the preservation potential of shear heating in rocks surrounding major faults.

Long-lived major faults extend over hundreds of kilometers and are widely distributed in a variety of crustal domains. These faults play a significant role in regional tectonic evolution and large-scale crustal deformation. Making reliable estimations of the strengths of major faults is an important part of developing a better

understanding of crustal strengths and the generation of large earthquakes, and the extent to which shear heating associated with movement on faults is a significant heat source for regional metamorphism. Deformation experiments show that mechanical work during fault movement is largely converted into heat energy. Although a single fault movement is a geologically instantaneous event and the associated shear heating causes rocks around the fault to experience high temperatures only during a very short period, long-lived major faults develop by repeated movements on geological time-scales and the associated thermal anomaly represents the gradual accumulation of numerous individual heating events, therefore widely spread thermal anomalies are expected around them.

Quantification of heating generated by fault movement (shear heating) on a major fault therefore has the potential to help in estimating shear stresses that operate on faults when they move. Rock deformation experiments suggest that the shear stress needed to cause displacement in fault zones is largely independent of rock type and predict significant amounts of shear heating along long-lived faults. Nevertheless, detailed studies for surface heat-flow measurements in the vicinity of the major San Andreas Fault (SAF) have not revealed any clear evidence for the expected shear heating. These results are commonly used to infer the SAF is a weak fault that supports lower shear stress than that expected based on rock deformation experiments. There is still no good consensus on the strength of these major tectonic boundaries. If shear heating can be recognized from long-lived major faults it would be clear evidence for the existence of relatively high stresses operating on major faults.

The MTL is the largest on-land fault in Japan with a long movement history from the Cretaceous to present, and is a good candidate for a comparison with the SAF. Previous thermochronological studies in the Ryoke belt to the north of the MTL indicate a broad thermal anomaly towards the MTL, which has been interpreted as evidence for shear heating. However, the detailed thermal structure around the fault and, in particular, in the Sanbagawa belt to the south of the MTL has not been determined. A semi-continuous borehole core passing through the MTL was recently drilled in the Kii peninsula. The availability of this core allows detailed analyses to be carried out in key samples close to the fault. Raman carbonaceous-material (CM) geothermometry can be used to estimate peak temperatures in metamorphosed pelitic rock, which is the main rock facies of the Sanbagawa belt in the study area. Therefore, I conducted a series of

Raman CM thermometry estimates to clarify the peak temperature attained in the Sanbagawa belt nearby the MTL, and used these results to investigate whether or not a thermal anomaly is present associated with the MTL.

I conducted detailed sampling from the core within 3 m from the MTL and more widely spaced sampling from field studies. The results of Raman spectral analyses show a consistent regional metamorphic temperature of ~340 ºC (low-*T* group) at distances between 4 km and 350 m from the MTL. There is a significant rise of up to ~60 ºC (high-*T* group) within 150 m from the MTL showing a significant amount of heating close to the fault. The close spatial association of the high-*T* group samples with the MTL strongly indicates that the rise in temperature is due to the effects of shear heating. In addition, the best-fit solution for these data shows that the displacement rates (V) of > ~80 mm/year are required to account for the thermal anomaly, and it is difficult to explain by using the generally observed range of values for V associated with strike-slip faults in convergent margins. The narrow thermal anomaly around the fault can be explained as the result of km-scale shortening of the footwall due to normal faulting after the formation of the thermal anomaly during strike-slip faulting. Assuming a temperature increase of 60 ºC at the fault plane and taking a maximum width of the original anomaly from the data of the Ryoke belt to the north of the MTL and ignoring the spatial distribution of the estimated thermal structure, gives results that imply a coefficient of friction, μ, along the fault greater than 0.4.

In Part 3, I conducted thermal modeling based on the thermochronological data set given by a previous study to the north of the MTL, and discuss the implications for fault strength and amount of displacement on the MTL.

In Part 2, I present evidence for shear heating in a limited zone to the south on the MTL in the Sanbagawa belt. To the north of the same MTL thermochronologic data of *Tagami et al.* [1988, JGR] reveal the presence of a broad thermal anomaly with a width of more than several kilometers in the Ryoke belt. This thermal anomaly is revealed by the presence of relatively young apatite fission track (Ap-FT) ages localized close to the MTL, and has been interpreted as evidence of shear heating. However, the potential for these data to investigate shear stresses acting on the MTL has not investigated. I used these data to calibrate possible one-dimensional thermal models of shear heating along the MTL and investigated the implications for fault strength and accumulated

displacement.

Far from the MTL, Ap-FT analyses yield consistent ages of ~54 Ma (old Ap-FT ages). In contrast, the Ap-FT ages close to the MTL yield younger ages of ~11–29 Ma (young Ap-FT ages). I examined the range of possible thermal models that could reproduce thermal profiles with temperatures above the Ap-FT annealing temperature of ~105 ºC at the locations of the young Ap-FT ages and temperatures below the apatite fission track annealing temperatures for the zone of old Ap-FT ages. I focused on the possible relationships between slip rates (V) and coefficients of friction (μ), and compared these to the range of values of V observed in convergent margins to constrain the range of possible values of μ on the MTL. The results imply that the thermal anomaly can be accounted for by shear heating that developed during strike-slip faulting with a coefficient of friction, $\mu > 0.22$ and total displacements of several hundreds of km on the MTL. These results are consistent with the results from the Sanbagawa belt discussed in Part 2, which also imply that the MTL is a major long-lived relatively strong fault.

Based on the results presented in Parts 2 and 3 and a compilation of information in the literature, I propose the following displacement history for the MTL in relation to the evolution of the Sanbagawa and Ryoke belts.

Stage 1 (> 20 Ma) Sinistral strike-slip movements took place along the MTL and formed km-scale thermal anomalies on both sides of the MTL due to shear heating.

Stage 2 (20–15 Ma) Dominantly strike-slip movements on the MTL changed to normal fault movements and assisted with a late stage in exhumation of the Sanbagawa rocks in the footwall. During this stage, parts of the Sanbagawa belt became attenuated causing parts of the original thermal anomaly to be lost and resulting in the presently observable thermal anomaly of a few hundreds of meters width to the south of the MTL.

Stage 3 (< 15 Ma) Erosion at rates of less than 1 mm/year led to the exposure of the asymmetrically distributed zones of shear heating north and south of the MTL. Modern strike-slip faulting has caused minor disruption to the belt of shear heating, but no observable thermal effects.

Part 1:
Large-scale folding in the Asemi-gawa region of the Sanbagawa belt

Abstract

The Sanbagawa belt represents metamorphism in a warm subduction zone. This belt generally shows higher metamorphic grade at higher structural levels. However, repetitions in the distribution of the metamorphic zones seen in central Shikoku exposed highest grade parts clearly show the original thermal structure has been affected by deformation after the peak of metamorphism. Lithological and structural data reveal the presence of a large-scale post-metamorphic fold in the central part of the highest grade. This folding has an axis that coincides with the thermal axis implied by the distribution of the metamorphic zonation. This result suggests the repetition of metamorphic zones in this area can be accounted for by folding without the need for major discontinuities and that the original metamorphic sequence is preserved intact.

1. Introduction

The Sanbagawa belt is a regionally coherent belt of subduction type metamorphism that formed in the mid-Cretaceous due to subduction of the Izanagi plate beneath the east Asian margin [e.g., *Wallis et al.,* 2009]. Numerous studies have documented the characteristics of deformation, metamorphism and chronology of this belt [e.g., *Wallis,* 1990; *Higashino,* 1990; *Itaya and Takasugi*, 1988]. In common with other subduction-type metamorphic belts, the Sanbagawa belt generally shows higher metamorphic grade at higher structural levels.

Petrological studies of the Sanbagawa belt have shown that the metamorphic grade can be divided into four zones based on the appearance of index minerals in metapelite: chlorite, garnet, albite-biotite, and oligoclase-biotite zones in increasing order of metamorphic temperature (Figure 1). Locally eclogite facies metamorphism is also present [e.g., *Takasu*, 1989; *Aoya*, 2001; *Aoki et al.*, 2009]. The overall inversion of metamorphic grade can be interpreted as reflecting an original inverted thermal structure characteristic in a subduction zone [e.g., *Enami et al.*, 1994]. However,

repetitions in the distribution of the metamorphic zones seen in central Shikoku clearly show the original thermal structure has also been affected by deformation after the peak of metamorphism (Figure 1). In addition, Sanbagawa metamorphic rocks experienced strong retrogression during exhumation.

One of the reasons for studying subduction-type metamorphic belts, such as the Sanbagawa belt, is to reconstruct conditions in otherwise inaccessible regions of subduction zones. For these studies, it is important to know how to relate the present structural sequence to the original arrangement in the subduction zone. Without this information it is difficult to identify the physical and chemical changes in the exposed rocks that correspond to similar changes at depth within a subduction zone.

The Asemi-gawa section is one of the key areas for looking at the large-scale structure of the Sanbagawa belt and its relationships to the metamorphism (Figure 1). This section lies roughly perpendicular to the metamorphic zonation and displays the highest metamorphic grade at intermediate structural levels (Figure 1). This region has been the focus for many detailed studies [e.g., *Kawachi*, 1968; *Hara et al*., 1977; *Banno et al.*, 1978; *Wallis*, 1990] and the metamorphic repetition has been interpreted both in terms of a large-scale fold [e.g., *Banno et al.*, 1978; *Wallis et al.*, 1992] and thrusting [e.g., *Hara et al.*, 1990]. Recently, another interpretation has been also suggested where their structure is accounted for by an extrusional wedge model [e.g., *Osozawa and Pavlis*, 2007; *Aoki et al.,* 2009]. In this contribution I present a detailed structural analysis of the area including the inversion axis of the metamorphism. The data presented in this study reveal the presence of a large-scale post-metamorphic fold, which can account for the repetition of metamorphic zones and suggests that the original metamorphic sequence is preserved intact. My results also imply that the large-scale deformation is caused by folding rather than some type of solid-state extrusion.

2. Main Phases of Ductile Deformation in the Asemi-gawa Region

Four main phases of ductile deformation are identified in the Asemi area. Following *Wallis* [1990] these are referred to as *Dr*, *Ds*, *Dt* and *Du*, with the alphabetical sequence corresponding to a time sequence recognized by overprinting stuctures. *Ds*, *Dt* and *Du* largely correspond to *D1*, *D2* and *D3* of other workers [e.g., *Kojima and Suzuki*, 1958; *Faure*, 1983, 1985]. Most structures in the Asemi area and

throughout the Sanbagawa belt can be ascribed to *Ds* or *Du* [*Wallis*, 1990]. Pre-*Ds* deformation phases are locally dominant in the highest grade regions of the Sanbagawa belt outside of the present study area [*Aoya*, 2002; *Mizukami and Wallis*, 2005].

Ds and all subsequent deformations postdate the peak of metamorphism [*Wallis et al.*, 1992] and, therefore, affect the distribution of the metamorphic zones. *Du* forms a series of upright folds and this phase clearly affects the kilometer-scale distribution of the metamorphic zones (Figure 1). The fold axes of both *Dt* and *Du* are roughly E-W and approximately parallel to the orientation of the *Ds* stretching lineation. If *Dt* or *Du* caused large-scale inversion of *Ds* structures and the metamorphic sequence this would also cause an inversion in the apparent sense of shear [e.g., *Wallis,* 1990]. However, consistent sense of shear associated with *Ds* [*Wallis*, 1990; *Takeshita and Yagi*, 2004] throughout the Asemi area and most of Shikoku shows that neither *Dt* nor *Du* caused large-scale inversion in this region. This implies that *Ds* is the most likely phase of ductile deformation that could explain the metamorphic repetition in the Asemi section. In my analysis of the structure of the region I, therefore, focused in particular on this phase of deformation.

2.1. Recognition of *Ds* Deformation

Throughout the Sanbagawa belt, *Ds* is the dominant phase of ductile deformation; it is characterized by the development of a strong generally northward to flat-lying schistosity and a less well-developed roughly east-west oriented stretching lineation. In this contribution, the schistosity and associated stretching lineation are referred to as *Ss* and *Ls*. The key microstructural feature that distinguishes *Ds* from other phases of deformation is the relationship with albite porphyroblasts (Figure 2). *Ds* deformation is the only phase of penetrative deformation that occurs after the development of albite porphyroblasts. This allows *Ds* to be identified in many individual outcrops where albite is developed. The main deformation in other neighboring outcrops can then be correlated on the basis of geometry and orientation of mesoscopic structures. These studies show the entire Asemi region has undergone strong penetrative *Ds* deformation. Before considering the structures of the region I first present the results of geological mapping (Figure 3). This mapping can also be used to discuss the large-scale structure of the region.

3. Lithological Mapping of the Central Asemi Area

3.1. Background

The study area covers the highest grade part of the Asemi section, the oligoclase-biotite zone, and also includes parts of the garnet and albite-biotite zones (Figures 1 and 3). This study presents not only a lithological map (Figure 3), but also the results of a detailed field survey including both outcrop patterns and structures (Figure 4). I believe it is important to include outcrop patterns to allow later workers to distinguish between observation and interpretation on the geological map and to enable future workers to build on preexisting data as new outcrops become available. In addition, many studies in high-strain metamorphic rocks such as those exposed in the Sanbagawa belt assume that bedding and schistosity are parallel. This is at best an approximation and is potentially misleading especially in areas of strong folding. In this study I use three point constructions to determine the orientation of lithological boundaries on scales relevant to my mapping and these are locally oblique to the main schistosity (Figure 3).

3.2. Lithologic Description

The dominant rock types of the study area are pelitic, basic and quartz schists with a small amount of serpentinite (Figure 3). They are generally distributed in an east-west direction. The most prominent lithological feature of the study area is a thick layer of basic schist at the intermediate structural levels. This layer can be traced in an east-west direction throughout the study area and my derived geological boundaries of this layer show a close correspondence to the independent mapping of *Shiota* [1991]. This layer is commonly referred to as the Shirataki spotted 5th amphibolite schist [*Hide*, 1954, 1961]. For simplicity, in this study I refer to this layer as the "Shirataki amphibolite".

Almost all the rocks in the study area have a well-developed schistosity and this is especially strong in pelitic schist. Pelitic schist is dominantly composed of graphite, mica, epidote, plagioclase, garnet, and quartz. Basic schist is dominantly composed of amphibole, epidote, plagioclase and mica. Garnet-bearing basic schist is also locally present. Microstructural observations of garnet amphibolite show garnet is present both as an inclusion in plagioclase porphyroblasts and as a matrix mineral. Some specimens only show garnet as an inclusion suggesting it has undergone strong retrogression in the matrix. Quartz is a minor but common component of the basic schist. Omphacite was

not observed. Basic schist is also locally associated with chlorite-rich schists (in this paper, these are referred as chlorite schists; Figure 3). These have a well-developed fissility schistosity.

Quartz schists are dominantly composed of quartz and exhibit various colors. Some of them show a distinct layered-structure interpreted as original sedimentary layering. In addition to quartz, the main minerals are mica, plagioclase, garnet and piedmontite. Sodic pyroxene is also locally present.

Serpentinite is generally massive with a weakly developed schistosity and is dominantly composed of serpentine minerals and chlorite. Serpentinite characteristically lacks any plagioclase-porphyroblasts.

Many of the lithologic contacts are locally gradational. In particular, quartz schists are interbedded with pelitic schists with gradational contacts. At two locations, basic schist alternates with pelitic schist at intervals of cm to tens-cm-scale (Figure 3). This suggests a sedimentary origin for the contacts and implies that not all pelitic-basic schist boundaries in the Sanbagawa belt are faults. Where they are developed, chlorite schists mark the boundary between basic and pelitic schists (Figure 3).

3.3. Protolith Stratigraphy

Accretionary complexes represent domains where oceanic material brought in by the subducting oceanic plate are mixed with continental material derived from the overriding plate. Continental material is dominantly sands and muds with a strong lithic component. In contrast, oceanic material is typically basalt, chert and siliceous mudstone in ascending order. When this stratigraphy is accreted to an active margin it will become deformed by thrusting and folding, but parts of the original stratigraphy are likely to be still preserved even after strong deformation [e.g., *Agar*, 1990; *Isozaki et al.*, 1990].

The protoliths of the Sanbagawa schists have lithological similarities to modern and ancient accretionary complexes [*Isozaki and Itaya*, 1990] and the original oceanic stratigraphy can commonly be recognized [e.g., *Okamoto et al.*, 2000]. Here I use the boundary between basic and quartz schist as an indication of the original younging direction: the basic schist is assumed to be part of the oceanic basement on which chert formed, which is now represented as quartz schist. In principle, the boundary between the pelitic and quartz schist could also be used in a similar way. However, they are

locally gradational and, therefore, not a reliable way to determine the original younging direction. The original oceanic stratigraphy suggests boundaries between basic and pelitic schist are likely to be fault contacts. The local presence of chlorite schist along these boundaries may represent the original fault rock. Intercalations of pelitic and basic schist are also observed. These suggest that locally there is sedimentary contact between the two rock types. Because of the variation in the nature of this contact, I do not use it to determine younging directions.

Contacts between basic and quartz schists suitable for determining younging directions are exposed in several locations in the study area. If a large-scale fold exists in this study area, the protolith stratigraphy should be overturned after crossing the fold axial trace.

The distribution of lithological boundaries where basic and quartz schist are in direct contact is presented in figure 3. This figure shows outcrops where basic schist structurally overlying layers of adjacent quartz schist (southward way-up structures) are dominant in the south sides of the Shirataki amphibolite and that layers of quartz schist overlying basic schist (northward way-up structures) are dominant in the north side. These observations suggest that protolith stratigraphy is inverted passing from the north to the south sides of the Shirataki amphibolite (Figure 3). This inversion implies the presence of a kilometer-scale fold. To determine when this fold formed with respect to the known deformation history of the area requires an analysis of the associated structures.

4. Structural Analysis of Ductile Deformation

4.1. Foliations and Lineations

Observation of the relationship between microstructures and the growth of albite porphyroblasts shows that *Ss* schistosity and *Ls* stretching lineation are well developed throughout the study area (Figures 3 and 5a). The *Ss* schistosity is particularly well developed in the pelitic schist (Figure 6b). An earlier schistosity, *Sr*, is also observed locally. This foliation can be observed in all lithologies but is particularly well-developed in basic schist (Figures 6a and 6c). *Ss* shows some variation in orientation, but dominantly trends east-west and dips at an angle of 30-60° to the north (Figure 5a). The associated stretching lineation, *Ls*, is dominantly oriented east-west with a shallow plunge.

The orientations of lithological boundaries determined by geometric constructions based on geological mapping are roughly east-west trending and northward dipping (Figures 3 and 5b). These lithological boundaries are generally almost coincident with the *Ss* foliation in the same area (Figures 5a and 5b). However, locally, the lithological boundaries and *Ss* schistosity are clearly oblique (Figure 3).

4.2. Folds

Many folding structures are observed in this study area (Figures 3, 5c-e, 6a,c-f). By observation of overprinting patterns and microstructures, folds are divided into three distinct stages. Following *Wallis* [1990] these stages are referred to as *Fs*, *Ft* and *Fu*-folds. Locally, multiphase folding structures are developed, which show that the upright *Fu*-folds, developed after the *Ft*-folds with gently dipping axial-planes (Figure 6d). These folds were all formed after the peak of metamorphism [e.g., *Wallis et al.*, 1992] and, therefore, affected the thermal and present geological structure in the study area. The tectonic significance of each phase is likely to be distinct and I describe the features for each phase separately.

Fs-folds are distributed widely throughout the study area (Figure 3). At outcrops of *Fs*, two foliations, *Sr* and *Ss*, are observed; *Sr* is folded by *Fs* and *Ss* is developed parallel to the *Fs* axial-plane (Figure 6a). Mesoscopic-scale *Fs*-folds are dominantly observed within layers of basic schist (Figures 6a and 6c), and much more rarely in pelitic schists. This may reflect the high-strain *Ds* deformation within the relatively weak pelitic layers that resulted in almost complete transposition of the earlier *Sr*. *Fs* are close to tight, and dominantly have east-west trending axes and northward dipping fold-axial-planes (Figure 5c). Within individual outcrops, *Fs* can be directly observed on centimeter to meter scales.

Ft-folds are locally present (Figure 3) and have open to close geometries with dominantly east-west trending fold-axes and gently dipping fold-axial-planes (Figures 5d and 6e). In individual outcrops *Ft*-folds are observed on centimeter to meter scales.

Fu-folds are also locally developed but are present throughout the study area (Figure 3). Similar to *Fs* and *Ft*, *Fu* show open to tight geometries and have east-west trending fold-axes, but *Du* can be distinguished by their steeply dipping fold-axial-planes (Figures 5e and 6f). In individual outcrops *Fu* folds are observed on centimeter to meter scales.

4.3. Faults

Bedding or schistosity are cross-cut by faults on outcrop scale. Fault rocks are not well developed along these faults, and there are no obvious sudden changes in stretching lineation or foliation orientation. At some lithological boundaries of basic-pelitic schist, chlorite schist—which may represent fault rocks—are distributed and their foliations are parallel to the *Ss* schistosity developed in nearby basic and pelitic schist. This implies that these structures were formed during *Ds* to pre-*Ds* deformation stages. Locally, these foliations are folded together with the schistosity.

4.4. Construction of Five Cross Sections and Documentation of Structures

To show the geological structure of the study area, five representative cross sections were constructed based on the above lithological and structural data. These cross-sections are shown in figure 7a-e and include a series of field sketches. These cross sections show that *Ds* structures are well developed, and *Ss* schistosity can be observed semi-continuously throughout the study area regardless of rock types. Post-*Ds* structures are also observed, but they are sporadically developed and associated foliations were not observed in this study area. Therefore, *Ds* deformation is the only stage of high-strain penetrative deformation and later deformation phases are of secondary importance in the study area. Nevertheless, post-*Ds* structures, especially *Fu*, are developed over a wide area, and these structures cause a clear warping of the *Ss* schistosity. *Ss* has a dominant northward dip throughout the study area. There are however, significant local differences. At the east side of the study area, low-angle foliations are developed, especially, at the north side of the Shirataki amphibolite (Figures 7d and 7e). In contrast, at the west side of the study area, foliations change to high-angle dips (Figures 7a and 7b). Post-*Ds* deformation, therefore, has a significant affect on the final geometry of geological units in this study area.

5. *Fs*-fold Vergence and Large-scale Folding

In cases where direct observation of large-scale folds is difficult, description of the sense of the fold vergence can help to reveal their presence [*Weijermars*, 1985]. In general, large-scale folds contain smaller-scale asymmetric partial structures in their limbs. When the axial-trace of a large fold is traversed during a field study, it is

expected that the sense of asymmetry (vergence) of outcrop-scale folds will change after crossing the fold-axial-trace. I determined fold vergence of *Ds* structures in the study area as a means of searching for larger scale folds. Changes in vergence of folds can occur on a variety of different scales and it is important to compare similar scale structures. In practical terms, I limited myself to describing meter-scale structures with the expectation that changes in vergence should correspond to the presence of folds on 100 meter to kilometer scales. Fold vergence on smaller scales is not included in the present analysis. The presence of curvilinear folds can complicate vergence analysis, and sheath folds have been described in quartz schists to the south of the present area [*Wallis*, 1990]. However, no strongly curvilinear folds were observed in the present study area and vergence analysis has shown to be an effective tool for examining the geological structure in other parts of the Sanbagawa belt [*Aoya*, 2002; *Mizukami and Wallis*, 2005].

5.1. Correlation of Deformation Phases

In this study area three main stages of folding are recognized (*Fs*, *Ft* and *Fu*). Meter-scale *Fs*-folds with clear vergence are widespread but not common (Figure 3). For this type of study it is imperative to distinguish *Fs* from post-*Fs* folds to ensure that the vergence analysis is only applied to folds formed during the same stage.

The schistosity folded by post-*Ds* folds is dominantly *Ss* formed by *Ds*, and the schistosity folded by *Fs* is *Sr* formed by *Dr*. Therefore, deformation stages of folds can be identified by determining whether the folded schistosity is *Sr* or *Ss*. One of the clearest ways to distinguish between *Dr* and *Ds* is the timing of deformation with respect to growth of plagioclase (Figure 2d) [*Wallis*, 1990, 1998]. *Sr* is overgrown by plagioclase porphyroblasts (Figure 2a), whereas *Ss* postdates the growth of plagioclase (Figures 2b and 2c). The appropriate stages of deformation for all of the m-scale *Fs*-folds used in the vergence analysis of this study were identified by microstructural analysis.

5.2. Inversion of *Ds* Fold Vergence

The distribution of m-scale *Fs* folds with clear vergence in this study area is presented in figure 3. This figure shows the structurally lower part of the Shirataki amphibolite contains south vergent folds whilst the structurally upper part contains

north vergent folds (Figure 6c). The change in the sense of m-scale *Fs*-fold vergence occurs near the central level of the Shirataki amphibolite. These data suggest that in the study area the axial-trace of a large-scale *Fs*-fold is present in the central part of the Shirataki amphibolite (Figure 3).

6. Discussion

6.1. Verification of Large-scale Folds in the Study Area

6.1.1. Correlation of Structural and Lithological Analyses

The distribution of observed *Fs*-fold vergence and the original younging direction is shown in figure 7a-d. The locations of major changes in both types of data are in good agreement with each other. This shows the existence of a large-scale fold with a northward closure in the central part of the Asemi-gawa area is shown by two independent data sets and the large-scale fold revealed by analysis of lithological boundaries was formed during *Ds* deformation (Figure 7c). Pre-*Ds* deformation could have caused inversion of the original stratigraphy, but this study shows protolith stratigraphy of basic-quartz schists is a useful tool for large-scale structural analysis of high-grade zones, in which it is difficult to observe sedimentary structures.

6.1.2. Possibility of the Existence of a Second Large-scale Folding

At higher structural levels above the Shirataki amphibolite, meter-scale *Fs* folds with south-vergence are recognized (Figure 3). This represents a second inversion of the fold vergence and it is possible that a second large-scale *Fs*-fold with a southward closure may exist in the study area (Figure 7c). But, at these higher structural levels, basic schist is less common and m-scale *Fs*-fold vergence, which is best preserved in basic schists, cannot be identified over a wide area. Therefore, it is difficult to clearly demonstrate the existence of this large-scale fold.

6.2. Correlation with the Thermal Structure in the Asemi-gawa Region

The analyses of *Ds*-fold vergence and sedimentary younging directions show there is a large-scale fold in the central part of the study area with a north downward closure (Figure 7c). The implied location of the fold-axis corresponds closely to the inversion axis of the metamorphic zonation, and is in good agreement with the interpretation of the present thermal structure in the Asemi-gawa region reported by *Wallis et al.,* [1992] (Figure 8; A-A'). The present thermal structure in the Asemi region can be explained by

large-scale folding and there is no need to introduce large thrusts, which have been proposed in previous studies [e.g., *Hara et al.,* 1990].

Osozawa and Pavlis [2007] also examined fold vergence in the Asemi region. These workers include a large variety of different scale structures and do not provide a clear framework for relating metamorphism and deformation and so direct comparison with my results is difficult. Despite these differences in methodology, these workers also identified a change in fold vergence in the same region as the one reported here. However, in contrast to my study, *Osozawa and Pavlis* [2007] interpret the change in vergence in terms of a change of sense of shear and relate this to a wedge extrusion model.

Fold vergence is a very unreliable indication of sense of shear in high-strain tectonites. A clear example is given by the Morcles Nappe in the European Alps [*Ramsay et al.*, 1983] where the fold vergence in the lower limb of a nappe is opposite to that of the transport direction. In addition, the wedge extrusion model requires synmetamorphic N–S stretching lineations to be developed throughout the region. This is clearly at variance with the observed lineation pattern both in my present study and throughout the Sanbagawa belt [e.g., *Wallis et al.*, 2009]. A region of strong N–S oriented movement is recorded close to the MTL [*Fukunari and Wallis*, 2007]. This deformation is related to brittle faulting and represents deformation at shallow levels in the crust.

For the above reasons, I consider that my observations in the Asemi area do not concur with the proposed model of *Osozawa and Pavlis* [2007] and the observed change in vergence is better interpreted as reflecting the presence of a large-scale fold.

6.3. Comparison with Large-scale Folds in Other Parts of Central Shikoku

Some large-scale *Fs*-folds have also been reported in other areas of the Sanbagawa belt in central Shikoku, and their axes are closely associated with main regions of higher-grade metamorphic zones [e.g., *Aoya*, 2002]. These observations suggest the possibility that the present distribution of the thermal structure of the Sanbagawa belt of central Shikoku is largely controlled by large-scale *Fs*-folds (Figure 8).

One of the clearest kilometer-scale folds in the central Shikoku area of the Sanbagawa belt is in the Shirataki area [*Hide*, 1954, 1961], which is located to the west of the Asemi-gawa section studied in this contribution. In the Shirataki area, basic schist

layers are sufficiently well defined and exposed to define a kilometer-scale fold with an antiformal structure (Figure 8; B-B'). Further to the west, interpretation of borehole data suggest that the Tonaru and western Iratsu are included in the core of a large fold (Figure 8; E-E') [*Hara et al.*, 1990]. In addition, studies of changes in the vergence of meter-scale *Ds*-folds suggest the presence of km-scale folds in the Besshi area (Figure 8; C-C', D-D') [*Aoya*, 2002; *Mizukami and Wallis*, 2005].

The large-scale folds are defined by the geometries of well-defined basic layers and tracing these suggests that most of the major folds can be linked structurally. The Shirataki amphibolite, which has a synform in the study area, is closest to the Shirataki area and tracing this layer present in the Asemi area suggests it links with a layer structurally above the Shirataki fold, which shows an antiformal structure (Figure 8; A-A', B-B') [*Hide*, 1954, 1961; *Hara et al.*, 1990]. The basic schist layers that comprise the Shirataki fold extend to the north-west. It seems likely that these are the same layers that form another large-scale fold with a synform including the Tonaru and western Iratsu mass at the core (Figure 8; B-B', E-E') [*Hara et al.*, 1990]. In addition, to the south, the Seba fold has been recognized [*Aoya*, 2002] and this also has a synformal structure (Figure 8; C-C'). The necessary link between these two structures is documented by *Aoya* [2002] and *Mizukami and Wallis* [2005] and consists of an antiformal structure (Figure 8; C-C', D-D'). This connection of these large-scale folds with each other implies that the large-scale structures of the central Shikoku can be mainly explained by the large-scale *Ds*-folds and the highest grade zone originally formed as a continuous sheet many 100km^2 in extent (Figure 8).

7. Conclusions

Analysis of lithological distributions, phases of ductile deformation and in particular fold vergence suggest the presence of kilometer-scale folding in the central part of the Asemi area. This folding has an axis that coincides with the thermal axis implied by the distribution of the metamorphic zonation and can explain the repetition of metamorphic zones in this area without the need for major discontinuities or extrusion type models.

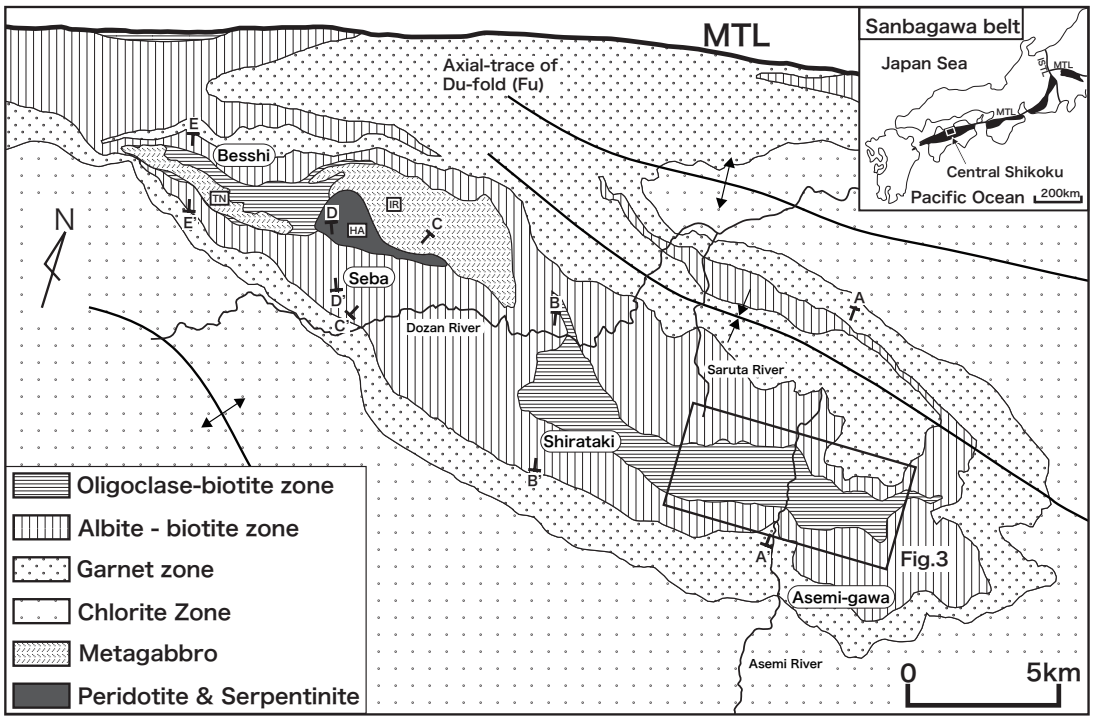

Figure 1. Metamorphic zone map of the Sanbagawa belt, in central Shikoku [Higashino, 1990]. Interpretational axial-traces of Du-fold are based on Hara et al. [1990]. Cross-sections along the five lines (A-A', B-B', C-C', D-D' and E-E') are shown in Figure 8. HA = Higashi-Akaishi mass; IR = Iratsu mass; ISTL = Itoigawa-Shizuoka Tectonic Line; MTL = Median Tectonic Line; TN = Tonaru mass.

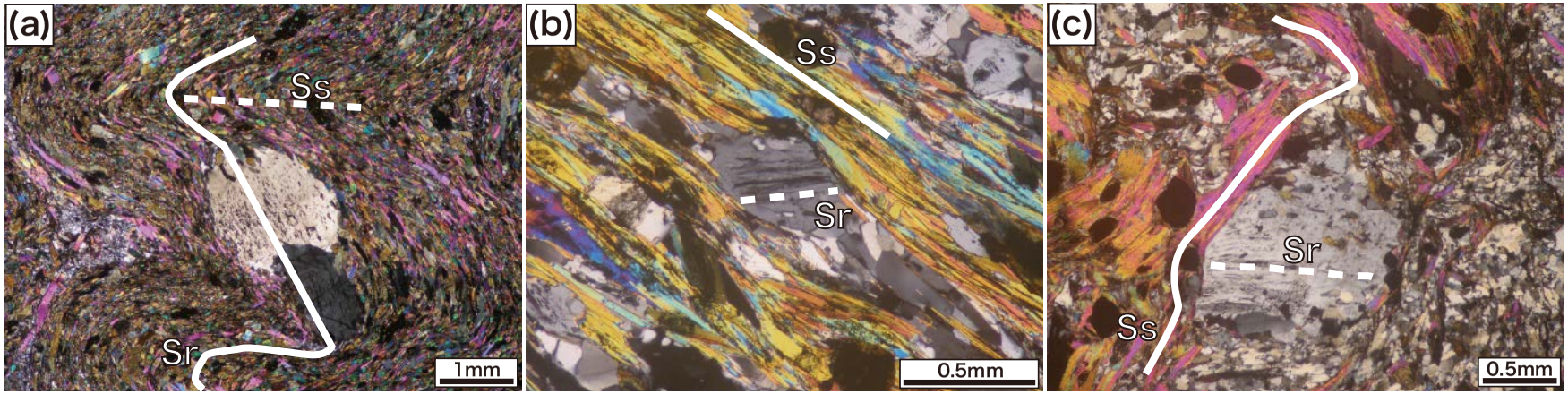

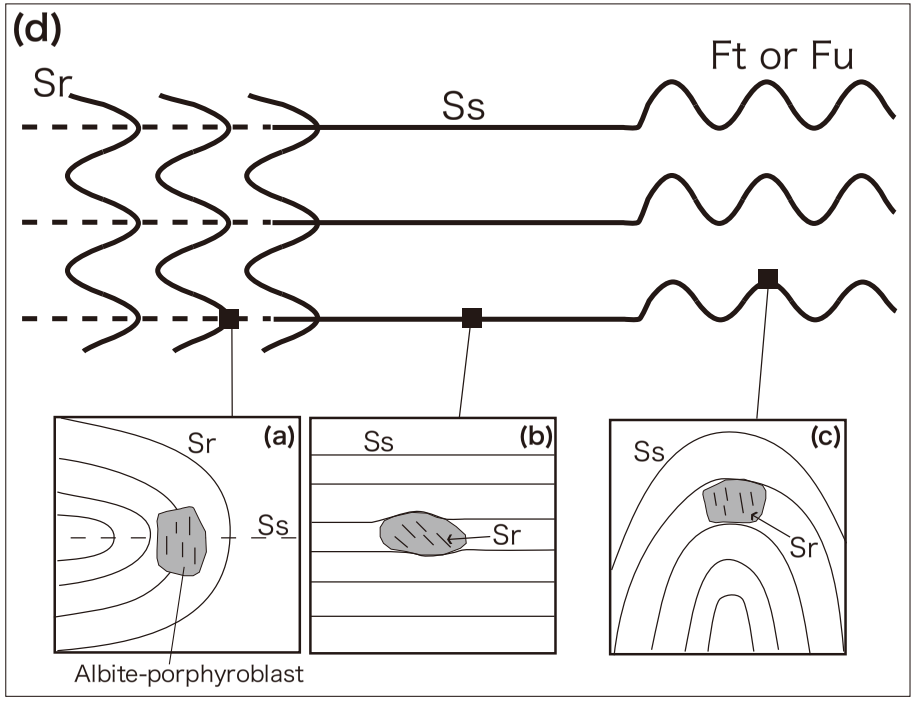

Figure 2. (a)-(c) Photomicrographs of albite porphyroblasts in basic and pelitic schists from the study area. (a) Albite porphyroblast(s) with straight inclusion trails show a continuous relation with the surrounding schistosity, confirming the folded schistosity to be Sr (broken line) and the folds themselves to be Fs; basic schist; crossed nicols. (b) Albite porphyroblast with straight inclusion trails which are at a high angle to the surrounding schistosity, confirming that the schistosity is Ss; pelitic schist; crossed nicols. (c) Albite porphyroblast within post-Ds folds; the straight inclusion trails within the albite porphyroblast (Sr) are at a high angle to the surrounding folded schistosity, confirming that the folded schistosity is Ss and the folds are post-Ds structures (Ft or Fu); pelitic schist; crossed nicols. (d) Schematic diagrams showing mesoscopic deformation structures (above), and microscopic occurrences of albite spots observed in several parts of mesostructures (below)—correlated to those shown in the photomicrographs of (a) to (c)— modified after Wallis [1998] and Aoya [2002].

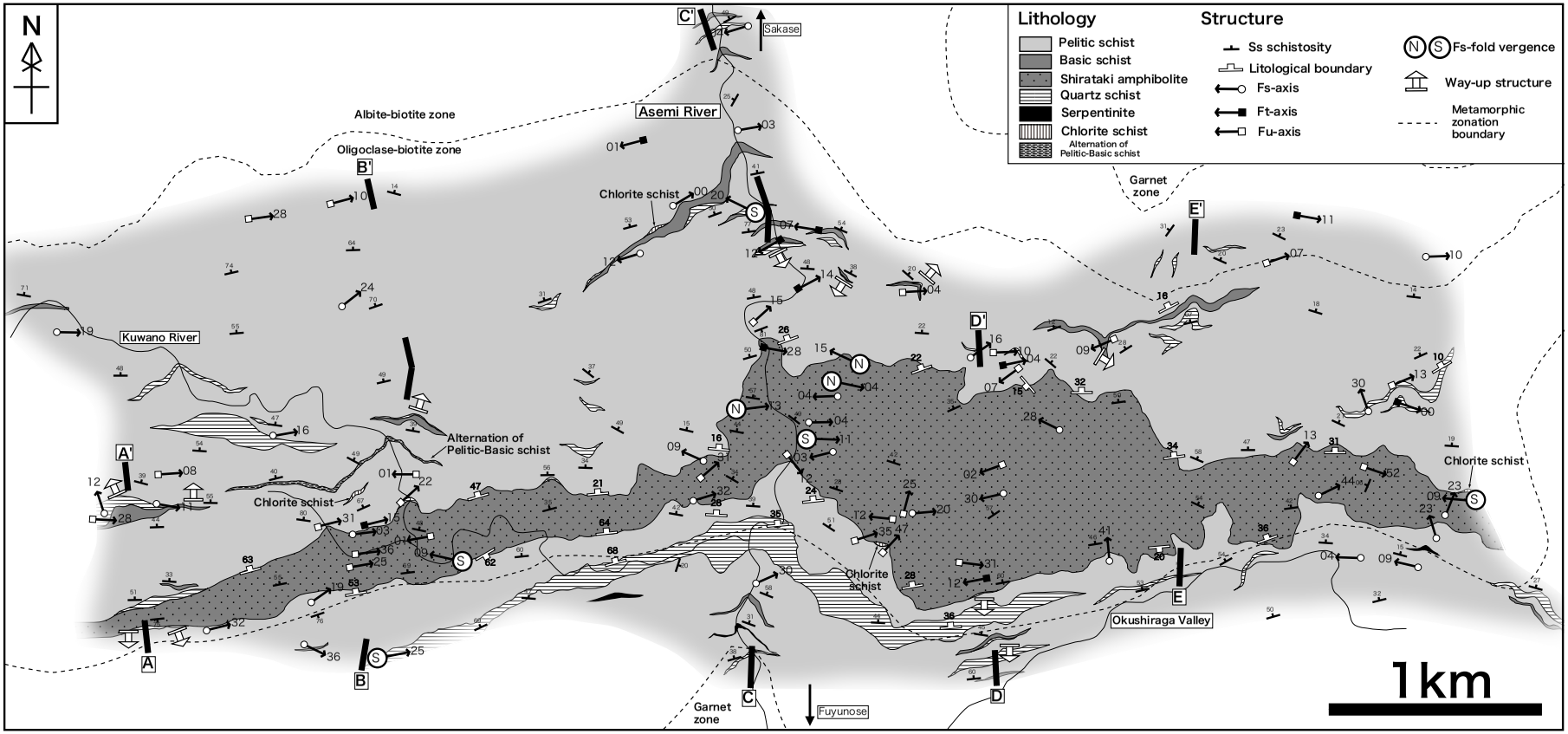

Figure 3. Lithological map of the study area with distribution of structures observed by field study and orientation of lithological boundary measured by geological mapping. Metamorphic zonation boundaries are taken from Higashino [1990]. Cross-sections along the five lines (A-A', B-B', C-C', D-D' and E-E') are shown in Figure 7.

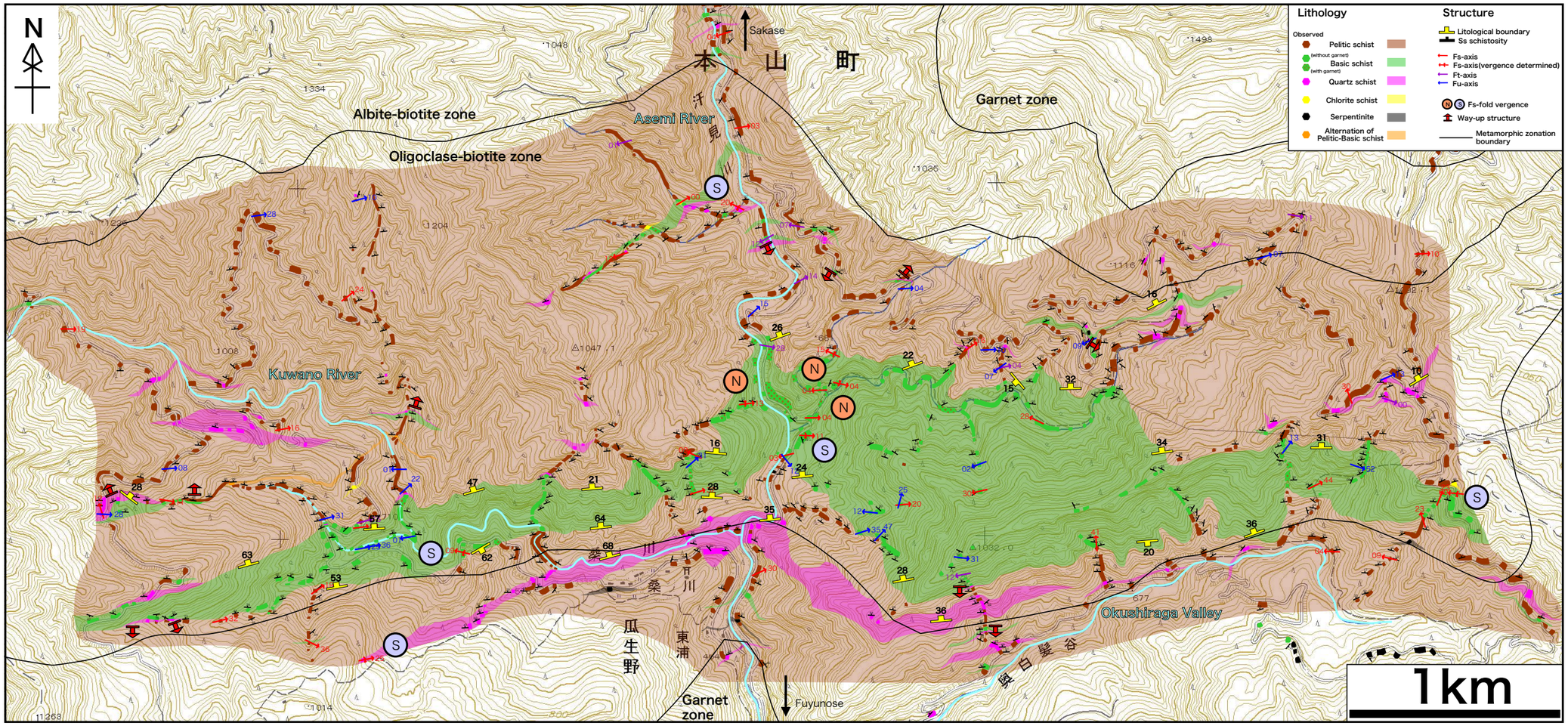

Figure 4. Lithological map of the study area with distribution of rocks and structures observed by field study and orientation of lithological boundary measured by geological mapping, which is drawn over topographical map. The outer frame shows as same size and location as that of Figure 3. Metamorphic zonation boundaries are taken from Higashino [1990].

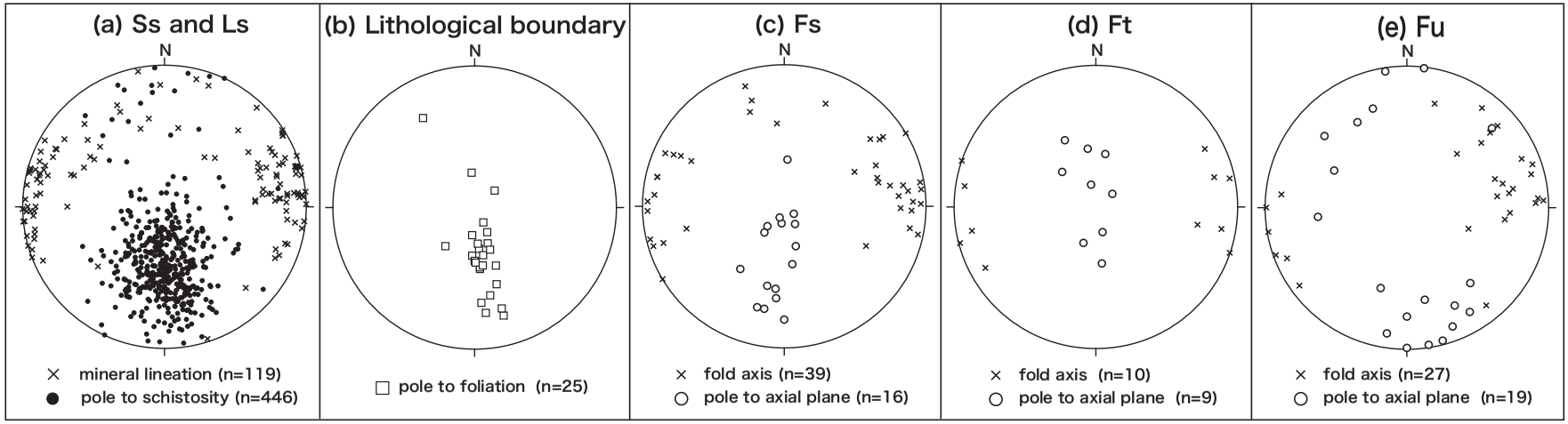

Figure 5. Stereographic plot (equal-area lower-hemisphere projection) of mesoscopic orientation data of Ss schistosity, Ls mineral lineation, Fs, Ft and Fu-folds from the study area. Data used for each plot are taken from the structures shown in Figure 4. (a) Poles to Ss schistosities and Ls mineral lineations. (b) Poles to lithological boundaries. (c) Fs-fold axes and poles to fold-axial-planes. (d) Ft-fold axes and poles to fold-axial-planes. (e) Fu-fold axes and poles to fold-axial-planes.

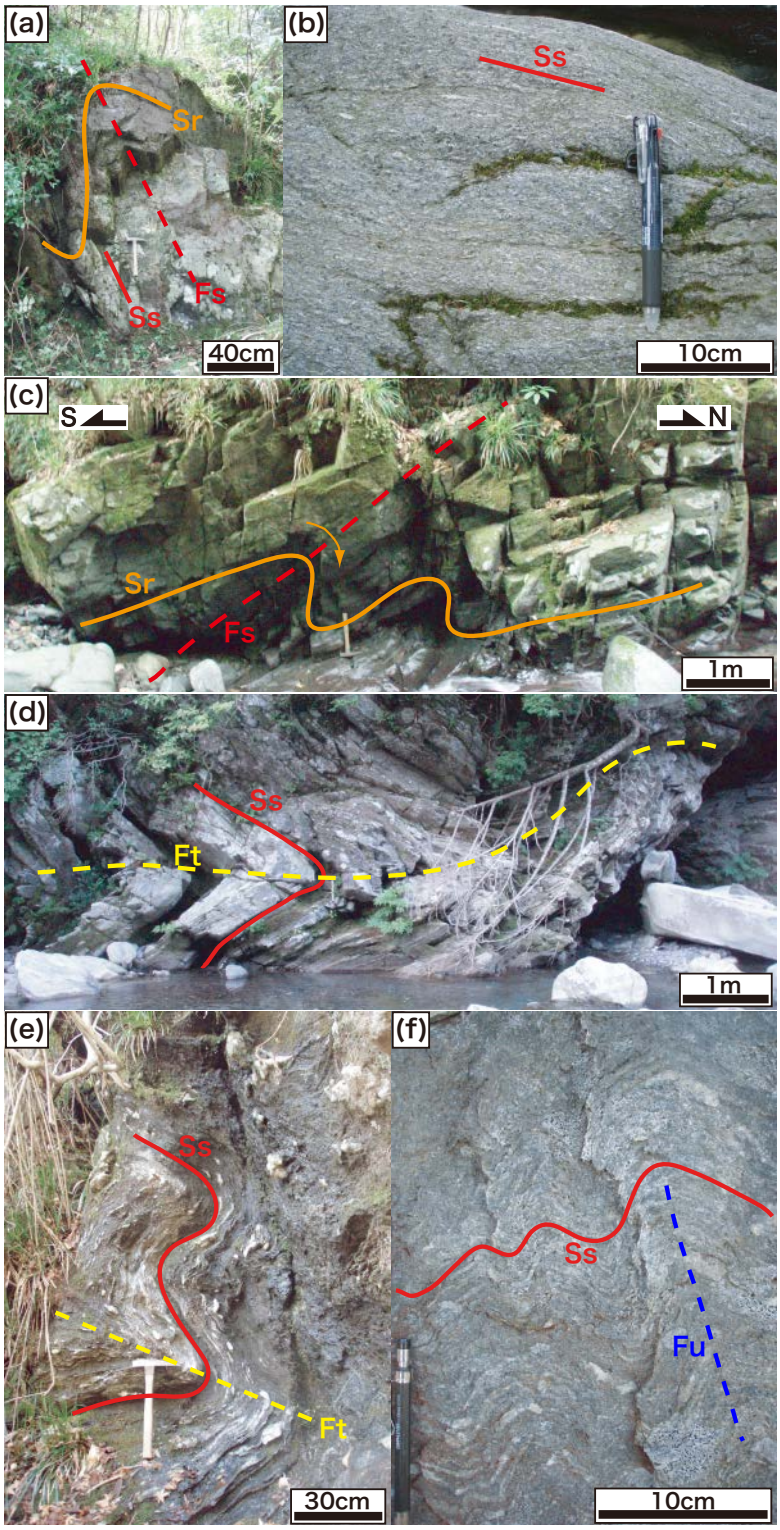

Figure 6. Outcrop photographs of Ds, Dt and Du structures in the study area. (a) Fs-fold in basic schist. Sr is preserved and Ss is observed parallel to Fs-fold axial-planes. (b) Well developed Ss schistosity in pelitic schist. Mesoscopic pre-Ds structures are not observed. (c) m-scale Fs-fold with north vergence in basic schist. (d) Overprinting structures in basic and quartz schist. The upright Fu-fold developed after the Ft-folds with gently dipping axial-planes. (e) Ft-fold in pelitic schist. (f) Fu-fold in pelitic schist.

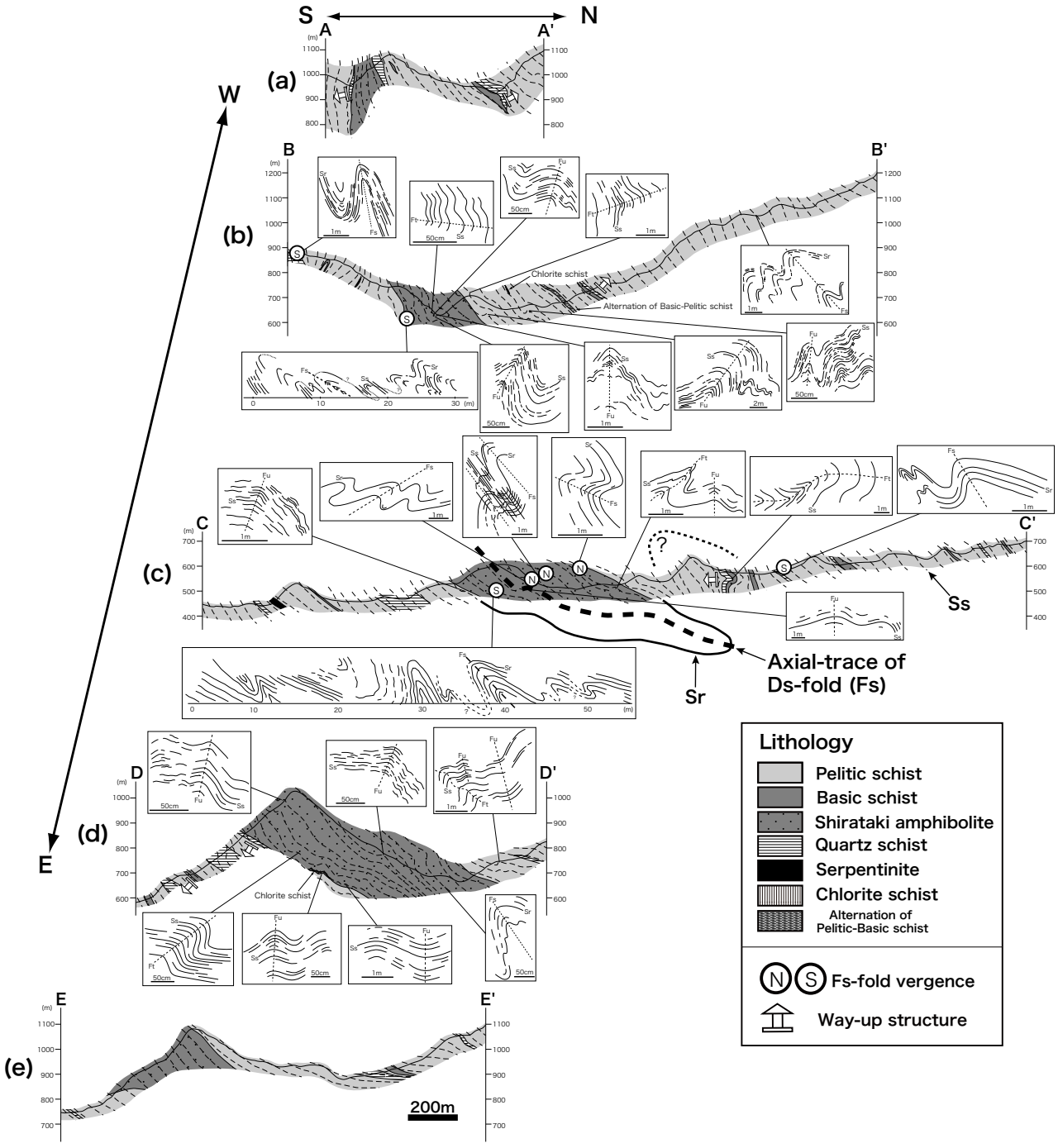

Figure 7. Cross-sections along the lines shown in Figure 3. Field sketches of Fs, Ft and Fu-folds from the sectional area drawn looking west, are also shown.

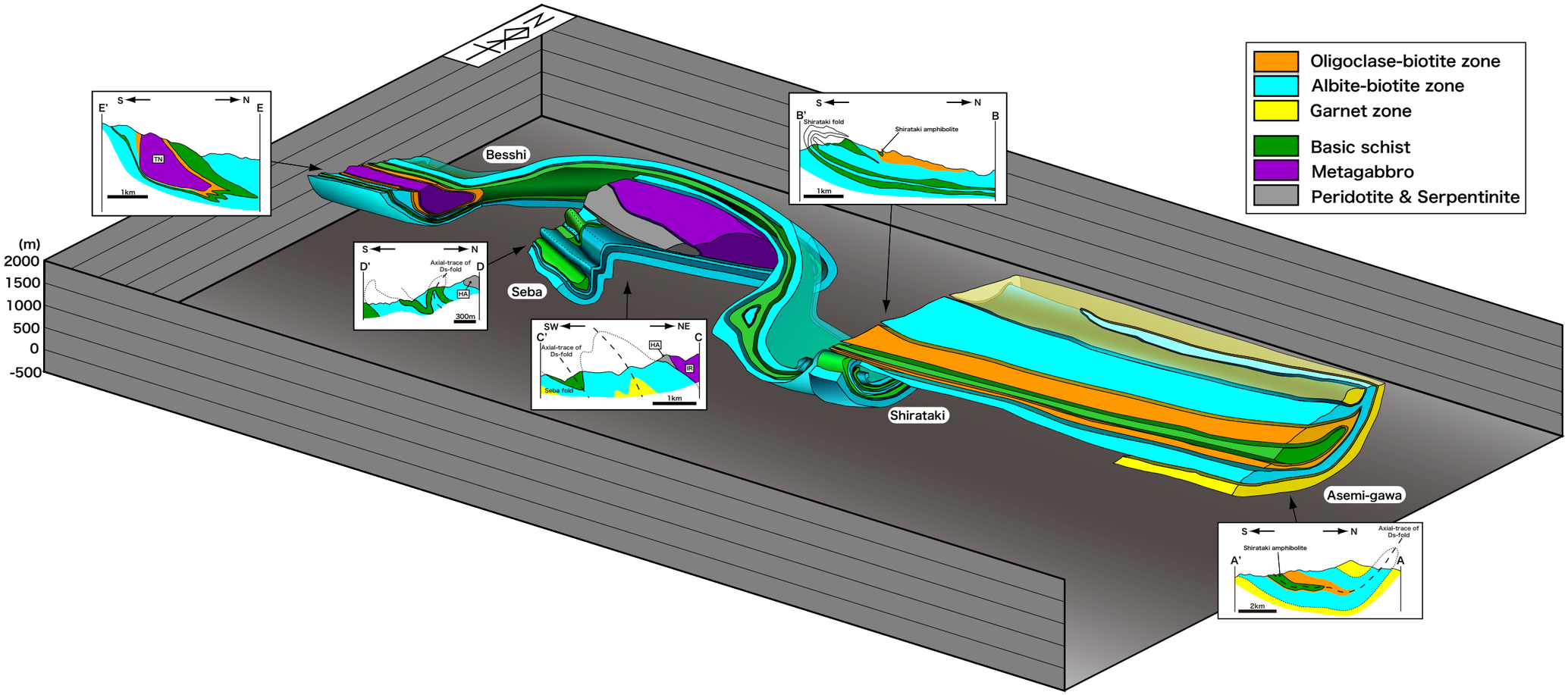

Figure 8. Cross-sections and three-dimensional diagram illustrating the proposed fold structures and their relationships in the Sanbagawa metamorphic belt of central Shikoku. Cross-sections are simplified from Hara et al. [1990], Wallis et al. [1992], Aoya [2002] and Mizukami and Wallis [2005]. Locations of the sections (A-A', B-B', C-C', D-D' and E-E') are shown in Figure 1. The three-dimensional diagram is drawn based on and compiled from the above cross-sections, the metamorphic zonation map of Higashino [1990] and the lithological map of Hara et al. [1990]. Horizontal scales and vertical scales are equal. The locations of the metamorphic zones and the mafic and ultra-mafic rocks follow previous studies as closely as possible. HA = Higashi-Akaishi mass; IR = Iratsu mass; TN = Tonaru mass.

Part 2:
Recognition of shear heating on a long-lived major fault using Raman carbonaceous material thermometry: implications for strength and displacement history of the MTL

Abstract

Documentation of thermal structures around major faults can help constrain the shear stresses operating when they move. Comparing the results of experimental work on the kinetics of crystallization of carbonaceous material with results of thermal modeling show that the Raman carbonaceous material (CM) geothermometer is well suited to studying shear heating on geological time scales in suitable lithologies of exhumed long-lived major fault zones. The Median Tectonic Line (MTL), SW Japan, is the largest on-land fault in Japan with a length of >800 km. Application of Raman CM thermometry to pelitic schist adjacent to the fault reveals the presence within a perpendicular distance of ~150 m from the MTL fault plane with T_{max} values about 60 ºC greater than the regional metamorphic temperature. The spatial association of this thermal anomaly with the fault implies it is due to shear heating. Thermal modeling shows the recorded thermal anomaly is compatible with very high rates of displacement over times scales of a few thousand years. However, such displacement rates are outside generally observed ranges. The narrow thermal anomaly around the fault can be explained as the result of km-scale shortening of the footwall due to normal faulting after the formation of the thermal anomaly during strike-slip faulting. Constraints on displacement rate, width of the original anomaly, duration of heating and peak temperature imply a coefficient of friction, μ, greater than 0.4.

1. Introduction

Long-lived major faults extend over hundreds of kilometers and are widely distributed in a variety of crustal domains such as continental strike-slip faults, oceanic transform faults, and subduction boundaries. These faults play a significant role in regional tectonic evolution and large-scale crustal deformation. Making reliable estimations of the strengths of major faults, in other words, the shear stresses acting on

them, is an important part of developing a better understanding of crustal strengths and the generation of large earthquakes, and the extent to which shear heating associated with movement on faults is a significant heat source for regional metamorphism [e.g., *Scholz*, 1980; *Molnar and England*, 1990].

Deformation experiments show that mechanical work during fault movement is largely converted into heat energy typically with an efficiency (e) of more than 90% [e.g., *Lockner and Okubo,* 1983]. The amount of heat energy can be expressed as

$$\dot{Q} = e\tau V = e\mu\sigma_n V \quad (1)$$

where $\dot{Q}$ is the heat flow per unit area by a fault movement ($Jm^{-2}s^{-1}$), τ is the average shear stress (Pa), V is the slip rate of the fault movement (ms^{-1}), μ is the coefficient of friction, and σ_n is the normal stress (Pa). Quantification of heating generated by fault movement (shear heating) therefore has the potential to help in estimating shear stresses that operate on faults when they move.

Rock deformation experiments suggest that the shear stress needed to cause displacement in fault zones is largely independent of rock type [*Byerlee*, 1978] and predict significant amounts of shear heating along long-lived faults. Nevertheless, detailed studies for surface heat-flow measurements in the vicinity of the major San Andreas Fault (SAF) have not revealed any clear evidence for the expected shear heating [*Brune et al.*, 1969; *Lachenbruch and Sass*, 1980]. These results are commonly used to infer the SAF is a weak fault that supports lower shear stress than that expected based on *Byerlee's Law*. This mismatch between experimental work and observation of natural faults is commonly referred to as the *Stress–Heat flow Paradox*, and there is still no good consensus on the strength of these major tectonic boundaries despite considerable research on this important topic.

If shear heating can be recognized from long-lived major faults it would be clear evidence for the existence of relatively high stresses operating on major faults. The presence of pseudotachylite, formed as the result of frictional melting, demonstrates that single phases of movement on faults may be associated with a major increase in temperature. However, such large rises in temperature will rapidly decay as the thermal energy is conducted away to the surrounding rocks. Here I am concerned with longer-term effects developed over geologically extended periods of time. These reflect the long-term strength of faults and if *Byerlee's Law* is correct should be associated with temperature rises of 100 °C or more developed on kilometer-scales, possible

examples are given in *Scholz et al.* [1979] and *Johnston and White* [1983].

In studies of shear heating along ancient faults, one of the most commonly encountered problems is how to recognize the temperature increase. In many cases geothermometry based on phase petrology is difficult to apply due to the lack of appropriate minerals and insufficiently large temperature rises. Thermochronology can provide good evidence for temperature rises above a certain critical value [e.g., *d'Alessio et al.,* 2003; *Yamada et al.*, 2007; *Tagami,* 2012], but these techniques provide much less information about the peak temperature experienced around the fault—which is important for calibrations with thermal modeling to estimate fault strength. Vitrinite reflectance of carbonaceous material has good potential to record detailed thermal structures around faults [e.g., *O'Hara*, 2004; *Sakaguchi et al.*, 2011]. However, the short time scales for equilibrium to be reached and the limited temperature range that can be recorded mean that these studies are best suited to studying single movements along relatively shallow faults. In this contribution, I examine the utility of the Raman carbonaceous material (CM) geothermometer [*Beyssac et al.*, 2002; *Rahl et al.*, 2005; *Aoya et al.*, 2010] for recognizing the long-term effects of shear heating around long-lived faults. I apply this technique to estimate the thermal structure in the Sanbagawa metamorphic belt around the Median Tectonic Line (MTL), SW Japan (Figure 1). Finally I combine these results with thermal modeling to constrain the fault strength of the MTL and discuss preservation potential of shear heating halos around major faults such as the MTL. This is important in view of the evidence for km-scale attenuation (by ductile thinning and normal faulting) of rock units adjacent to major faults [e.g., *Harms and Price*, 1992; *Argles et al.*, 1999].

2. Outline of the Median Tectonic Line and Geological Setting

The MTL stretches over a distance of >800 km and separates the Sanbagawa and Ryoke belts (Figure 1) that formed in the east Asian Cretaceous convergent margin [*Isozaki and Itaya*, 1990; *Takasu and Dallmeyer*, 1990; *Nakajima*, 1994; *Suzuki and Adachi*, 1998; *Wallis et al.*, 2009]. The oldest recorded movements on the MTL are sinistral strike-slip in the Cretaceous [e.g., *Ichikawa*, 1980; *Miyata et al.*, 1980; *Takagi*, 1986; *Shimada et al.*, 1998]. A significant phase of normal faulting occurred in the middle Miocene (~20-15 Ma) [e.g., *Takagi et al.*, 1992; *Takahashi et al.*, 2006; *Fukunari and Wallis*, 2007]. The most recent movements are dextral strike-slip [e.g.,

Huzita, 1980; *Okada*, 1980]. In this paper, I use the term "Median Tectonic Line" (MTL) to describe the tectonic boundary between the Sanbagawa and Ryoke belt irrespective of its age of formation.

The Sanbagawa belt extends continuously from the Kyushu district eastward to the Kanto Plain along the south side of the MTL (Figure 1) and represents the deeper parts of an accretionary complex [e.g., *Isozaki and Itaya*, 1990; *Takasu et al.*, 1994; *Wallis*, 1998]. The main lithologies are pelitic, mafic and quartz schists. Multiple phases of ductile deformation have affected the Sanbagawa belt [e.g., *Faure*, 1983; *Wallis*, 1990; *Hara et al.*, 1992; *Wallis et al.*, 1992; *Takeshita and Yagi*, 2004]. The dominant phase is characterized by stretching in an approximately E–W direction and is associated with formation of the main schistosity [e.g., *Wallis et al.*, 1992].

Three boreholes were recently drilled by the Geological Survey of Japan, AIST, at Matsusaka-Iitaka (ITA) in the eastern Kii peninsula (Figures 1 and 2) [*Shigematsu et al.*, 2009; *Shigematsu et al.*, 2012). One of the boreholes (Hole 1) passes through the MTL which was analyzed in the present study (Figure 2b). The MTL in the eastern Kii peninsula around the ITA dips approximately 56º to the north (Figure 2b) [*Shigematsu et al.,* 2012]. The total depth of the Hole 1 is 600 m and it encounters the MTL at a depth of 473.9 m (Figure 2b). In the study area, the northern side of the MTL consists of the Hatai tonalite, which is part of the Ryoke belt whereas the southern side consists mainly of pelitic schists of the Sanbagawa belt (Figures 2a and 2b). The Sanbagawa schists show a penetrative schistosity referred as *Ss* [e.g., *Wallis*, 1990]. *Ss* is commonly folded about E–W trending fold axes [*Fukunari and Wallis*, 2007]. A systematic change in the orientation of the axial planes of these folds is observed: relatively flat-lying axial planes near the MTL and steeply dipping axial planes further away. This change is best explained as the effects of ductile normal shear on the MTL [*Fukunari and Wallis*, 2007]. Brittle and semi-brittle shear structures related to movement on the MTL are also common in the Sanbagawa belt around ITA [e.g., *Wibberley and Shimamoto*, 2005; *Fukunari and Wallis*, 2007]. *Shigematsu et al.,* [2012] use mineral assemblages in the fault rocks close to the MTL to show that much of the mineralogical alteration related to displacement on the MTL occurred at temperatures of ~200 ºC.

3. Samples Used

3.1. Sampling Strategy

A common difficulty of thermal studies of fault zones is the lack of suitable exposure to collect a full suite of samples in the key areas close to the fault plane where the maximum effects of shear heating are expected. Therefore I combine the results of detailed sampling from the semi-continuous borehole core (Hole 1) at ITA with more widely spaced sampling from field studies (Figures 1 and 2). This combination allows us to estimate both the background temperature and the thermal structure near the MTL.

3.2. Lithology and Geological Structure in the Sanbagawa Belt

Figure 2c shows the results of a field survey carried out in the Sanbagawa belt around ITA. Layers or elongate lenses of mafic and quartz schists occur within the dominant pelitic schist. The lithological layering is sub-parallel to the dominant tectonic foliation (schistosity) in the adjacent pelitic schists. The main schistosity (*Ss*) dominantly strikes E–W and is associated with a roughly horizontal mineral lineation (Figure 3a) parallel to a later set of fold axes (Figure 3b). Figure 2d shows a cross-section that was constructed based on the above lithological and structural data. Minor faults were observed in the field on scales of several cm to tens-cm. However, none was associated with large fracture zones such as that observed around the borehole of the MTL as documented below.

Shigematsu et al. [2012] classify rocks affected by faulting in the borehole (Hole1) through the Sanbagawa belt (Figures 4a and 4b) into protolith (schist), damaged rock (Figures 4d and 4f), fault breccia (Figures 4c and 4e), and fault gouge (Figure 4d). In addition to fault rocks derived from pelitic and mafic schists, the core also contains several small serpentinite bodies with a total thickness of ~16 m (drilling depths of ~510–520 m and ~580–586 m; Figures 4a and 4b); similar serpentinite bodies were not recognized in the field work. The rocks below 555 m show the same penetrative schistosity (*Ss*) as recognized in the regional studies with relatively minor fracturing and disruption. At shallower depths than about 555 m, the Sanbagawa rocks show extensive fracturing except a zone of less-intense fracturing at depths of 495-520 m (Figure 4a). Fault gouge and fault breccia are dominant between drilling depths of 477.2 m to 473.9 m (Figure 4b). A clear distinction can be made between ultramylonite derived from the Ryoke granitic rock in the hanging-wall of the MTL and fault breccia derived from the Sanbagawa rock in the footwall at a depth of 473.9 m (Figures 4a to 4c).

3.3. Samples for Temperature Estimations

Samples of pelitic schist for temperature estimation by Raman carbonaceous-material (CM) geothermometry were collected both from the region in the south of the ITA (FIT1-13; Figures 2c and 2d; Table 1) and from the borehole core (Hole1) (CIT1-8; Figures 2d, 4a and 4b; Table 1). The pelitic schist samples referred as protolith above descriptions of the borehole core (FIT1-13 and CIT1,2) are dominantly composed of quartz, graphite, mica, and plagioclase. The main schistosity is defined by the alignments of graphite, mica and quartz and the alternation of graphite-rich and quartz-rich layers (Figure 5a). Samples consisting of damaged rocks or fault breccia were collected from the borehole core between 478.7 m and 474.35 m (CIT3-8). These samples are mainly composed of rock fragments and quartz- and plagioclase-clasts in a fine-grained matrix (Figure 5b). The rock fragments mainly consist of quartz, plagioclase, calcite, graphite, and mica, and many of these grains show a well-developed schistosity (Figure 5c). The fine-grained matrix consists mainly of graphite, clay minerals and calcite.

4. Raman Carbonaceous-Material Geothermometry

4.1. Method of Estimating Peak Temperature

Discriminative bands of the Raman spectrum of carbonaceous-material (CM) appear at around 1350 cm^{-1} (D1-band), 1580 cm^{-1} (G-band) and 1620 cm^{-1} (D2-band) (Figure 6). Poorly ordered carbon also has a D3-band at around 1530 cm^{-1} [e.g., *Beyssac et al.*, 2002] and D4-band at around 1250 cm^{-1} [e.g., *Lahfid et al.*, 2010]. Several different Raman CM thermometers have been proposed based on various methods of quantifying and combining these characteristic peaks reflecting the degree of graphitization [*Beyssac et al.*, 2002; *Rahl et al.*, 2005; *Aoya et al.,* 2010]. In this study, I adopt the calibration and methodology given by *Aoya et al.* [2010], which is applicable to metamorphic effects on a wide range of timescales. Following the original suggestion of *Beyssac et al.* [2002] this method uses an area ratio, R2, of the D1, D2, and G peaks, where R2 = D1/(G+D1+D2). R2 can be converted to temperature by using the following quadratic equation:

$$T\,(^{\circ}\mathrm{C}) = 221.0\,R2^2 - 637.1\,R2 + 672.3. \quad (2)$$

This equation is valid for the temperature range of 340–655 ºC, and estimated errors are about ± 30 ºC [*Aoya et al.*, 2010].

4.2. Recognition of Shear Heating

A single fault movement is a geologically instantaneous event, and the associated shear heating causes rocks around the fault to experience high temperatures only during a very short period (Figures 7a-1 and 7a-3). In contrast, long-lived faults develop by repeated movements (Figure 7a-3) on geological time-scales, and the associated thermal anomaly represents the gradual accumulation of numerous individual heating events (Figures 7a-4 and 7a-5). Therefore, rocks around long-lived faults may undergo a series of pulses of heating on short time-scales (Figures 7a-1 and 7a-3) and a lower temperature more widely spread heating on longer time scales (Figures 7a-4 and 7a-5). The Raman CM thermometer assumes that after a sufficiently long heating duration, the degree of graphitization—which is reflected to the R2 value—reaches a steady state, i.e. there is no further increase in the degree of graphitization, and this state only depends on the peak temperature attained (Figure 7b). Before sufficient time has elapsed for steady state to be achieved, the degree of graphitization (R2) is a function of both temperature and the duration of heating. To apply the Raman CM thermometry to shear heating requires a consideration of the time-scales of heating compared to those required for CM crystallization to reach a steady state. Previous work has shown that Raman CM thermometry is an effective tool for estimating the peak temperature of regional metamorphism with time-scales of >10 million years (Figure 7b) [*Beyssac et al.*, 2002; *Rahl et al.*, 2005]. *Aoya et al.* [2010] shows that a similar methodology can be applied to contact metamorphism around large intrusions associated with heating time-scales >0.1 million years (Figure 7b). In contrast, heating experiments of CM show no clear change of the R2 values of CM at a temperature of 1000 ºC maintained for 580 hours (~3.5 weeks; Figures 7b and 7c) [*Beyssac et al.*, 2003]. This implies that temperature increases on similar short time-scales will not be recorded by Raman CM studies.

To investigate the potential for pulses of shear heating to be recorded by Raman CM thermometry, I carried out a set of thermal calculations (Figures 7c and 7d). Assuming heat dissipation is solely by conduction around a planer heat source, the thermal structure around a fault after each fault movement can be represented by the following one-dimensional equation [e.g., *Carslaw and Jaeger,* 1959],

$$T(x,t) = \frac{Q}{2c\rho_r\sqrt{\pi\kappa t}} e^{-\frac{x^2}{4\kappa t}} + T_0 \tag{3}$$

where Q is the amount of heat generated per unit area by a single fault movement, c is specific heat, ρ_r is rock density, κ is thermal diffusivity, and T_0 is the initial temperature. Q is given by the following equation:

$$Q = e\tau D = e\mu\sigma_n D \tag{4}$$

where D is the slip displacement and the other variables are defined in the explanation of equation (1). On geological time scales, the cumulative effects of these individual pulses can be represented by the following equation (derived from equation (3)) assuming the time interval between slip events and the associated displacements are constant:

$$T(x,t) = \sum_{i=1}^{N} \left(\frac{Q}{2c\rho_r\sqrt{\pi\kappa\left(t - I\left(i-1\right)\right)}} e^{-\frac{x^2}{4\kappa\left(t-I(i-1)\right)}} \right) + T_0 \tag{5}$$

Here I is the slip interval, i is the number of slip order (index of summation), and N is the total number of occurrences of slip events (N is an integer; $t/I < N \leq t/I+1$). In addition, if a fault acts with a continuous slip rate the thermal structure around a fault is represented by the following equation:

$$T(x,t) = \frac{\dot{Q}}{c\rho_r}\left(\frac{t}{\pi\kappa}\right)^{\frac{1}{2}} e^{-\frac{x^2}{4\kappa t}} - \frac{\dot{Q}|x|}{2c\rho_r\kappa} erfc\frac{|x|}{2\sqrt{\kappa t}} + T_0 \tag{6}$$

where $\dot{Q}$ is the heat flow per unit area caused by a fault movement with a constant slip rate (equation (1)). Although values of shear stresses (τ) and coefficients of friction (μ) of a fault plane are not constant during fault movements, for simplicity I treat τ and μ as average shear stresses and coefficients of friction without changing their values over the timescale of heat generation (during faulting) for calculations $\dot{Q}$ and Q of equations (1) and (4) respectively.

Figures 7c and 7d show the temperature increases ($T–T_0$) calculated by using equations (3), (5) and (6). I assume τ = 100 MPa, D = 5 m for the calculations of equations (3) and (5), and other parameters are shown in Table 2. To maintain the same total heat for both calculations using equations (5) and (6), I used an average slip rate of V = 5 mm/year, and values of D = 5 m and I = 1000 year ($V = D/I$).

The results for single fault movements show clear temperature increases nearby the fault (x = 0.1 m) of over 100 ºC within a few minutes after slip, however, the temperature drops to less than 60 ºC within a few weeks and the temperatures over 1 m from the fault plane never exceed 60 ºC (Figure 7c). These short pulses of temperature rise occur on time scales much less than the total history of movement on long-lived faults and, importantly, also much less than the time scales needed for the effects to be recorded by Raman CM thermometry. The long-term temperature profiles due to shear heating can, therefore, be approximated by the results of continuous slip of equation (6) (broken lines in figure 7d).

Many previous studies that use geothermometers to detect shear heating have focused on heat generated by a single fault movement, such as vitrinite reflectance [e.g., *Sakaguchi et al.*, 2011] and fission track analyses [e.g., *d'Alessio et al.*, 2003]. In contrast, my study shows that the Raman CM thermometer is a useful tool to extract the longer-term accumulated shear heating on long-lived faults: heating related to single phases of secondary faulting will be too short lived to be recorded by the Raman CM thermometer. It is the long term heating effect that has been at the root of the whole problem about estimating fault strengths from heat anomalies that have been argued over the years, referred as "*Stress–Heat flow Paradox*".

5. Application of Raman CM Geothermometry and Derivation of Thermal Structure

5.1. Sample Preparation and Selection of Carbonaceous-Material for Measurement

Measurements were carried out using polished thin sections. For intact schist samples (Figure 5a), I cut the thin sections perpendicular to the schistosity and parallel to the mineral lineation. Assuming the (0001) plane of CM is aligned parallel to the schistosity, the laser will be at a high angle to the graphite c-axis for most measurements. Although some dependence on the orientation of the laser with respect to the crystal axes has been reported for Raman spectra of CM [e.g., *Katagiri et al.*, 1988; *Wang et al.*, 1989], *Aoya et al.* [2010] show that direction of irradiation of CM grains results has a negligible effect when compared to other sources of error in the geothermometer. Samples of fault breccia and damaged rock are strongly affected by brittle shearing (Figure 5b) and clasts show a wide range of orientations of the

schistosity. *Aoya et al.* [2010] suggest deformation can form dislocations in CM and this leads to a higher R2 ratio and lower estimated peak temperature than in less deformed rocks. To avoid the secondary effects of post-peak deformation, the measurement of CM in samples from the fault damage zone was therefore conducted only within CM-bearing clasts that preserve a clear schistosity (Figure 5c).

Following the procedure recommended in *Aoya et al.* [2010], ~30–90 spots were analyzed for each sample (Table 1) in order to adequately reflect the full natural range of intersample variation; this is important to obtain a reliable temperature estimate.

5.2. Measurement Conditions for Raman Spectral Analysis

An Almega XR (Thermo Nicolet) micro-Raman system with a green 532 nm, Nd-YAG laser combined with an Olympus, BX51 optical microscope was used for the measurements. A ×100 objective lens with a numerical aperture of 0.90 was used and the laser irradiation power at the sample surface was 3 mW. Scattered light was collected by a backscattered geometry with a 25-μm pinhole and a holographic notch filter. The limit of spectral resolution is about 1 cm^{-1}, determined by measurement with a mercury lamp. The Raman spectrum was acquired with a single polychrome spectrometer equipped with a CCD detector with 1024 × 256 pixels. The acquisition time for each analysis was 30 s. The wavenumber resolution is ~1 cm^{-1} in the spectral range using 2400 lines per mm grating. The spectrometer was calibrated using neon lines. The relative intensity of the Raman spectrum was corrected using a white-light illuminant calibrated by National Institute of Standards and Technology (NIST), USA. Peak position and band area (integrated area) were determined using the computer program Peak Fit 4.12 ver. (SeaSolves Software Inc.) with a Voigt function on the assumption that the original spectrum consists of up to five peaks on a linear baseline (Figure 6).

5.3. Results of R2 Values and Estimated Temperatures

The results of the Raman spectral analyses are summarized in Table 1. Figure 8 shows representative Raman spectra and the corresponding R2 histograms, which are arranged in order of increasing distance from the MTL from top to bottom (Figures 2d, 4a and 4b; Table 1). All of the Raman spectra have clear G, D1 and D2 peaks with their peak positions at around ~1580, ~1350, and ~1620 cm^{-1} (Figure 8a). Histograms were

constructed for all samples (Figure 8b). There is a general change in the shapes of the R2 distributions from sharp to broad peaks associated with a change in the average values of R2 from high (~0.67) to low (~0.55) with decreasing distance from the MTL. The histograms of CIT4 and CIT7 show bimodal distributions (Figure 8b). However their peaks are not sharp and the data do not greatly deviate from the overall trend. Therefore, I include the data of these two samples for temperature estimations, and treat them in the same way as those of the other samples.

Figure 9 shows the derived temperatures and associated 1σ errors. The results show a consistent regional metamorphic temperature of 341–348 ºC at distances between 4 km and 350 m from the MTL (FIT1–11; Figure 9a; Table 1). This I refer to as the low temperature (low-*T*) group. Within 150 m of the MTL (FIT12, 13 and CIT1–8) there is a significant rise in temperature to 362–408 ºC (Figure 9a and 9b; Table 1), and the highest value is obtained at a distance of 0.6 m from the MTL (CIT7; Figure 9b; Table 1). I refer to this as the high temperature (high-*T*) group. The high-*T* group includes schist (protolith) samples without intense fracturing (FIT12,13 and CIT1,2; Figures 2c, 4a and 9a; Table 1). Within 5 m from the MTL, there is no clear dependence of the estimated temperatures to the fault structures between fault breccias and damaged rocks (CIT3-8; Figures 4b and 9b; Table 1).

5.4. Interpretation of the High Temperature Group in Terms of Shear Heating

The close spatial association of the high-*T* group samples with the MTL strongly indicates that the rise in temperature (thermal anomaly towards the MTL; Figure 9) is due to the effects of shear heating. Further evidence in support of this interpretation is given by the close relationship between the extent of the damaged domain that has undergone suffered intense brittle shearing and the distribution of the high-*T* group samples (Figures 4 and 9; Table 1).

Other explanations for the presence of a high-*T* zone close to the MTL can be considered. Some intrusions in the Ryoke belt are synchronous with cooling ages in the Sanbagawa belt [e.g., *Takasu and Dallmeyer*, 1990; *Nakajima*, 1994; *Suzuki and Adachi*, 1998; *Wallis et al.*, 2004], and the Sanbagawa rocks may have suffered their thermal effects. However the MTL cuts metamorphic zonation in both the Sanbagawa and Ryoke metamorphic belts [e.g., *Higashino*, 1990; *Nakajima*, 1994], and my study data show no evidence of intrusions during exhumation of Sanbagawa rocks. These suggest

the high-*T* group was not affected by magmatic activity.

The other possible explanation is that a high-grade part of the Sanbagawa belt has been juxtaposed against the lower grade region due to fault movements with large displacements. However, regions of the Sanbagawa belt that are of sufficiently high grade are exposed ~30 km away from the present field area [*Takeuchi*, 1996]. To juxtapose this higher grade material would require kilometer-scale lateral movements, which would be reflected in the development of a major fault zone with a wide fracture zone [e.g., *Otsuki*, 1978; *Scholz et al.*, 1993]. No broad damage zone was recognized outside of the high-*T* domain. These observations suggest that the major lateral displacement was concentrated in the MTL fault zone and lateral transport of high-grade material can also be excluded as a cause of the juxtaposition between the high-*T* and low-*T*.

6. Thermal Modeling and Fault Strength

To evaluate the frictional property (coefficient of friction) of the fault based on the above mentioned thermal anomaly by shear heating, I conducted thermal modeling to account for the estimated thermal structure. As discussed in the previous section, the Raman CM geothermometer should reflect the accumulated thermal effects due to shear heating, and the associated thermal history can be adequately calculated by considering continuous slip governed by equation (6) (Figure 7d). I therefore employ equation (6) for my thermal calculations.

As strategies for evaluating the shear heating, I determined the data sets of $\dot{Q}$ and t required to reproduce the thermal structure by using equation (6) and then seek the relationships between V and μ (or τ) that are required to reproduce the appropriate value of $\dot{Q}$ by using equation (1).

6.1. Parameter Constraints and Estimates

The material parameters and initial conditions for calculations are shown in Table 2. The regional metamorphic temperature is estimated to be ~340 ºC (low-*T* group). The deformation close to the brittle-ductile transition in the Sanbagawa metamorphic rocks is suggested to have occurred in this range with associated temperatures between 200 and 380 ºC [*Fukunari and Wallis*, 2007; *Fukunari et al.*, 2011]. In my calculations I therefore use this value for the initial temperature (T_0), and estimated the corresponding

depth (h) by using T_0 and a geothermal gradient (G) of 25 ºC/km: $h = T_0/G$ (Table 2).

Both strike-slip and normal displacements has been reported along the MTL [e.g., *Ichikawa*, 1980; *Miyata et al.*, 1980; *Fukunari and Wallis*, 2007; *Kubota and Takeshita*, 2008]. Therefore, I constrained shear stress (τ) and coefficient of friction (μ) by constructing Mohr's circle diagrams for both cases. I make the following assumptions.

(1) One of the principal stresses is vertical and equal to the overburden pressure ($\rho_r gh$, where g is the acceleration due to gravity; Table 2); for strike-slip faulting this is the intermediate principal stress (σ_2) assumed to be equal to the average of the maximum and minimum principal stresses ($\sigma_2 = \bar{\sigma} = (\sigma_1 + \sigma_3)/2$), and for normal faulting this is the maximum principal stress (σ_1) (Figure 10).

(2) The angle between σ_1 and the orientation of the fault plane (θ) was assumed to be 45 º for strike-slip faulting (Figure 10a) and taken to be 56 º—the present attitude of the MTL—for normal faulting (Figure 10b).

(3) The pore fluid pressure (P_f) to be hydrostatic pressure at the depth (h): $P_f = \rho_f gh$, where ρ_f is the density of fluid (Figure 11; Table 2). *Fukunari et al.* [2011] suggest that fluid pressure was significantly below lithostatic pressure during brittle deformation of the MTL based on a significant discrepancy between fluid inclusion isochores and retrograde *P–T* paths.

I estimated the values of τ for a possible range of μ from 0.1 to *Byerlee's Law* ($\tau = 0.85 \times (\sigma_n - P_f)$ for $\sigma_n - P_f > 200$ MPa and $\tau = 0.6 \times (\sigma_n - P_f) + 50$ for $\sigma_n - P_f \leq 200$ MPa) as shown in Figure 11. For strike-slip faulting, values of τ were estimated to be from 23 MPa for μ = 0.1 to 186 MPa for *Byerlee's Law* (Figure 11a). For normal faulting, values of τ were estimated to be from 19 MPa for μ = 0.1 to 78 MPa for *Byerlee's Law* (Figure 11b).

6.2. Thermal Modeling Results

Figure 12 shows the best-fit solution to all the estimated temperature data (determined by minimizing the sum of the squared differences between data and model). The results indicate that values of $\dot{Q}$ = 0.47 $Jm^{-2}s^{-1}$ and a duration of movement of t = 4.47×10^{-3} million years since the onset of fault movement can adequately account for the temperature difference in the vicinity of the MTL. Figure 13 shows the relationships between V and μ that need to be satisfied to account for this $\dot{Q}$ calculated by using equation (1). If I adopt *Byerlee's Law* for strike-slip faulting (μ = 0.82 for the maximum

estimated shear stress of τ = 186 MPa in figure 11a), a value of V = 89 mm/year is required to obtain the value of $\dot{Q}$ (green broken line in figure 13). Larger values of V are required both in the cases of strike-slip faulting associated with lower μ and in the case of normal faulting (Figure 13). Varying the different calculation parameters (Figure 14) does not alter the conclusion that the temperature rise close to the MTL still requires relatively high rates of movement along the fault.

Although the rise in temperature can be easily modeled, it is difficult to account for the details of the thermal structure including both the rise in temperature close to the fault and the steep thermal gradient between the low-T and high-T groups of results. For instance, reducing the shear stress results in a broad thermal anomaly with no steep temperature gradients (Figure 14a). Reducing V results in a similar broad thermal anomaly and also requires greater time for the same temperature rise close to the fault zone (Figure 14b). Reducing the value of T_0 does not significantly reduce the rate of movement required to account for the recorded anomaly (Figure 14c).

7. Discussion

7.1. Affects of Secondary Deformation

Some samples within the high-T group yield relatively low temperatures (FIT13, CIT1, 2, and 8; Figure 9; Table1). One explanation that can account for both the narrow zone of high-T and the scatter in the data is that there has been significant shear heating but that this domain has been disrupted and attenuated by post-heating faulting. Normal faulting associated with rotation of the underlying material can result in excision of parts of the sequence [e.g., *Buck,* 1988]. In my field studies I did not recognize any significant faults south of the MTL. However, a seismic profile does show a possible fault [*Yamaguchi et al.*, 2009] near the location of FIT12—where slightly higher temperatures were recorded than those of the surrounding samples (Figure 9a)—that can be correlated with the normal faulting that occurred along the MTL observed from the field around the present study area [*Fukunari and Wallis*, 2007] and from the same borehole samples [*Shigematsu et al.,* 2012]. Therefore the scatter of temperature estimates with temperatures deviated from the overall trends of the temperature increases towards the MTL may reflect effects of such minor faulting disrupting the peak temperature structure. In this case my results will underestimate the width of the original thermal anomaly.

7.2. Constraint of the Coefficient of Friction along the MTL

The values of $V > 80$ mm/year estimated by thermal modeling are much greater than the present-day slip rate of 5 mm/year along the MTL (gray broken line in figure 13) [*Tabei et al.*, 2002, 2003]. These values also exceed observed rates of strike-slip motion along major strike-slip faults in the rear of accretionary margins such as Sumatra (~36 mm/year) and Chile (~7 mm/year) [e.g., *Jarrard*, 1986] and even the highest slip-rates (~10 mm/year) of normal faulting reported from other regions [e.g., *Hodges et al.*, 1998]. These suggest that if realistic μ–V relationships are used, none of the results of thermal modeling adequately account for the estimated thermal structure (Figure 13).

Weak faults can produce significant shear heating effects if they slip at a high rate over a geologically long period of time. The resulting thermal anomaly will be broader than that recognized in this study before the peak temperature structure is disrupted by normal faulting as discussed in the section above. Thermochronological studies in the Ryoke belt to the north of the MTL show a region of elevated temperatures with a varying thickness. This high-T zone is interpreted as the result of shear heating during strike-slip faulting [*Tagami et al.*, 1988]. The maximum extent of this zone is ~20 km and because shear heating is expected to develop symmetrically around faults, I can use this as a guide to the upper limit of the domain of raised temperature in the Sanbagawa belt. It is also possible to place some general constraints on the rate of displacement of displacement on large strike-slip faults such as the MTL. The review by *Jarrard* [1986] shows that strike-slip faults at the rear of convergent margins move at rates dependent on the degree of obliquity of convergence with a maximum of around 20 mm/year. It is also possible to look at horizontal displacement by combining rates of movement with the time constraints from the Ryoke belt given by *Tagami et al.* [1988], which show the zone of high-T in the Ryoke belt was formed within ~43 million years (~54 Ma–11 Ma).

As a lower estimate of the long-term fault strength of the MTL, I now seek the lowest value of μ that is compatible with an increase of > 60 °C above the background temperature under the conditions that the associated thermal anomaly is no more than 20 km and is developed over a time period no more than 43 million years (Figure 15a). In addition, the long-term strike-slip rate on the MTL should be no more than 20 mm/year (Figure 15b).

Figure 15a shows that the width constraint provides a limit of about one million years on the time scale of heating (areas filled with light yellow). In combination with the constraint on slip rate (≤ 20 mm/year), this time scale requires that the coefficient of friction on the fault be greater than ~0.4 (shaded areas in figure 15b).

7.3. Tectonic Evolution of the MTL and Implications for Tectonic Development of The Sanbagawa and Ryoke Belts

Based on the results of previous studies and the present study, I propose the following history for the MTL and the Sanbagawa and Ryoke belts (Figure 16). Sinistral strike-slip movements took place in the MTL from the Cretaceous (Figure 16a) to the Paleogene (> ~20 Ma; Figure 16b). During the period of strike-slip faulting of the MTL, the Sanbagawa rocks were at depths corresponding to conditions between the peak metamorphic conditions (ductile zone) and the brittle-ductile transition zones. In contrast, the Ryoke rocks were at shallower depths (Figures 16a and 16b) [*Tagami et al.,* 1988]. The strike-slip faulting formed km-scale thermal anomalies on both sides of the MTL due to shear heating. The effects of shear heating are expected to be less in the present exhumed level of the Sanbagawa rocks undergoing ductile deformation where shear stresses are likely to be significantly lower (Figure 16a).

After strike-slip faulting, movements on the MTL changed to normal fault movements in the Miocene (~20 Ma; Figure 16c) [e.g., *Takagi et al.*, 1992; *Takahashi et al.*, 2006; *Fukunari and Wallis*, 2007; *Shigematsu et al.*, 2012]. If normal faulting propagates from the footwall toward the hanging-wall with rotation of fault planes from high to low-angles [e.g., *Buck*, 1988] parts of the original sequence will become attenuated (Figures 16c-f). This attenuation will cause parts of the original thermal anomaly in the footwall block to be lost (Figure 16g). This combination of normal faulting and erosion can account for the asymmetric distribution of the zones of shear heating north and south of the MTL.

8. Conclusions

1. Raman carbonaceous-material geothermometry is an effective tool for studying shear heating on geological time scales in exhumed long-lived major fault zones, that is, the geothermometer can only record longer-term accumulated thermal anomalies generated by shear heating.

2. Application of Raman CM thermometry reveals a thermal anomaly in the Sanbagawa belt with a width of 150 m adjacent to the MTL and a peak temperature ~60 ºC higher than the surroundings. The spatial association of the thermal anomaly with the fault zone implies that the cause is shear heating.
3. The narrow zone of shear heating recognized in the Sanbagawa belt is compatible with the MTL being a strong fault broadly in accordance with *Byerlee's Law*. However the predicted associated slip rates are unreasonably high. Constraints on maximum slip rate, time scale of heating and width of thermal anomaly suggest a minimum coefficient of friction around 0.4.
4. The narrow belt of shear heating recorded in the Sanbagawa belt has probably undergone substantial thinning due to normal faulting.

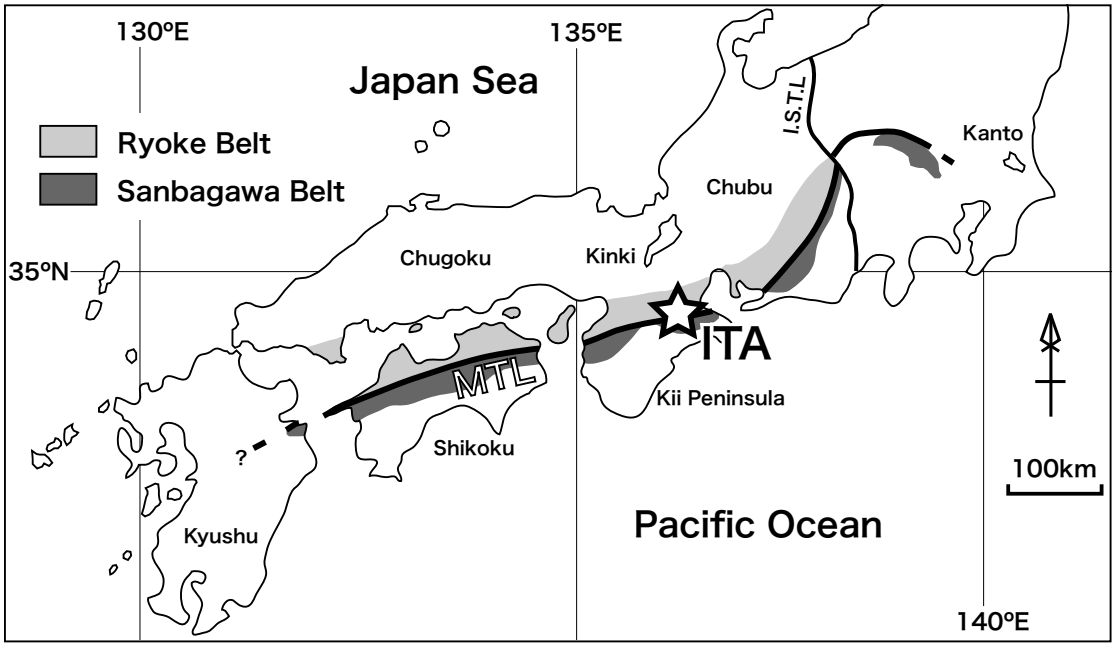

Figure 1. Distribution of the Median Tectonic Line, the Sanbagawa and Ryoke belts modified after Isozaki [1996]. Star symbol indicates the location of the borehole, ITA. MTL, Median Tectonic Line; I.S.T.L, Itoigawa-Shizuoka Tectonic Line.

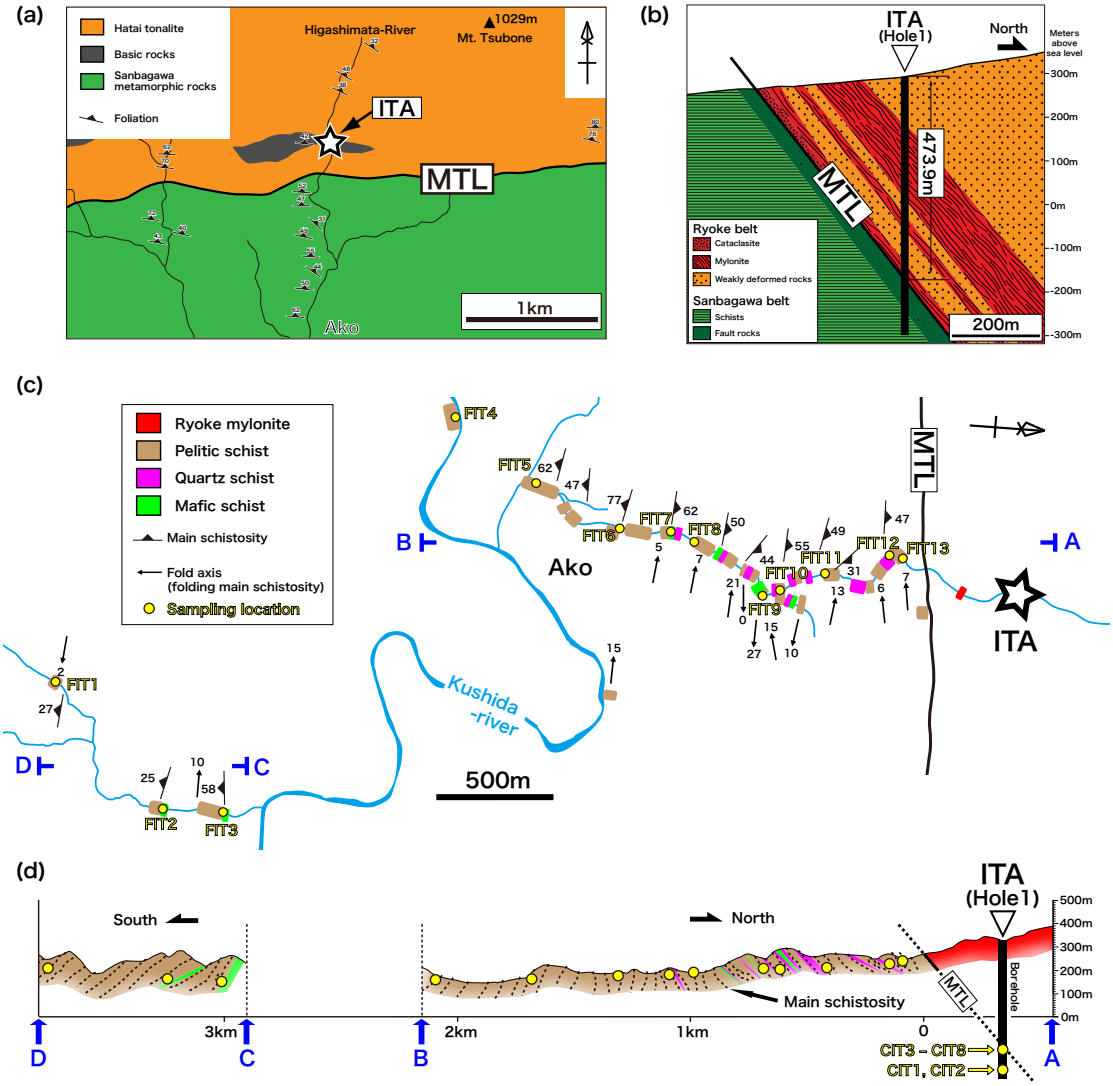

Figure 2. (a) Geological map of the area around ITA (star symbol) modified after Shimada et al. [1998]. Structural data for the Sanbagawa metamorphic rocks were obtained in our field studies. Those for the Hatai tonalite and mafic rocks are after Shimada et al. [1998]. (b) Schematic geological cross section around ITA. The borehole (Hole1; vertical bold line) passes through the MTL at a depth of 473.9 m. Modified after Shigematsu et al. [2012]. (c) Route map in the Sanbagwa belt around ITA with structural data for the main schistosity, fold axes of folds deforming the main schistosity, and sampling locations. (d) Cross section along the line A–B and C–D of (c) with the borehole (Hole1) and traces of sampling locations including those corrected from the borehole core.

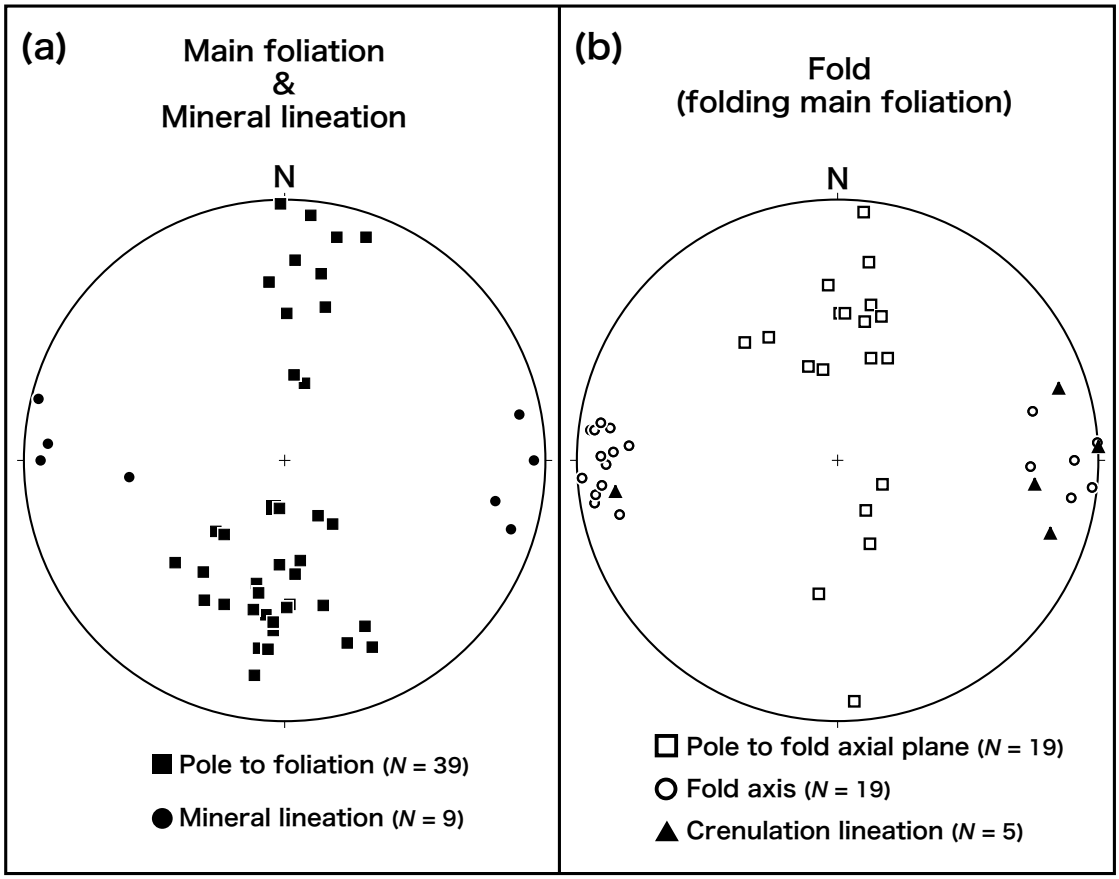

Figure 3. Stereographic plot (equal-area lower hemisphere projection) of mesoscopic orientation data of the main schistosity, mineral lineation, and folds observed in the field study area. (a) Poles to main schistosity and associated mineral lineations. (b) Poles to fold axial planes, and their axes—including crenulations. These folds deform the main schistosity. The number of measurements is indicated by N.

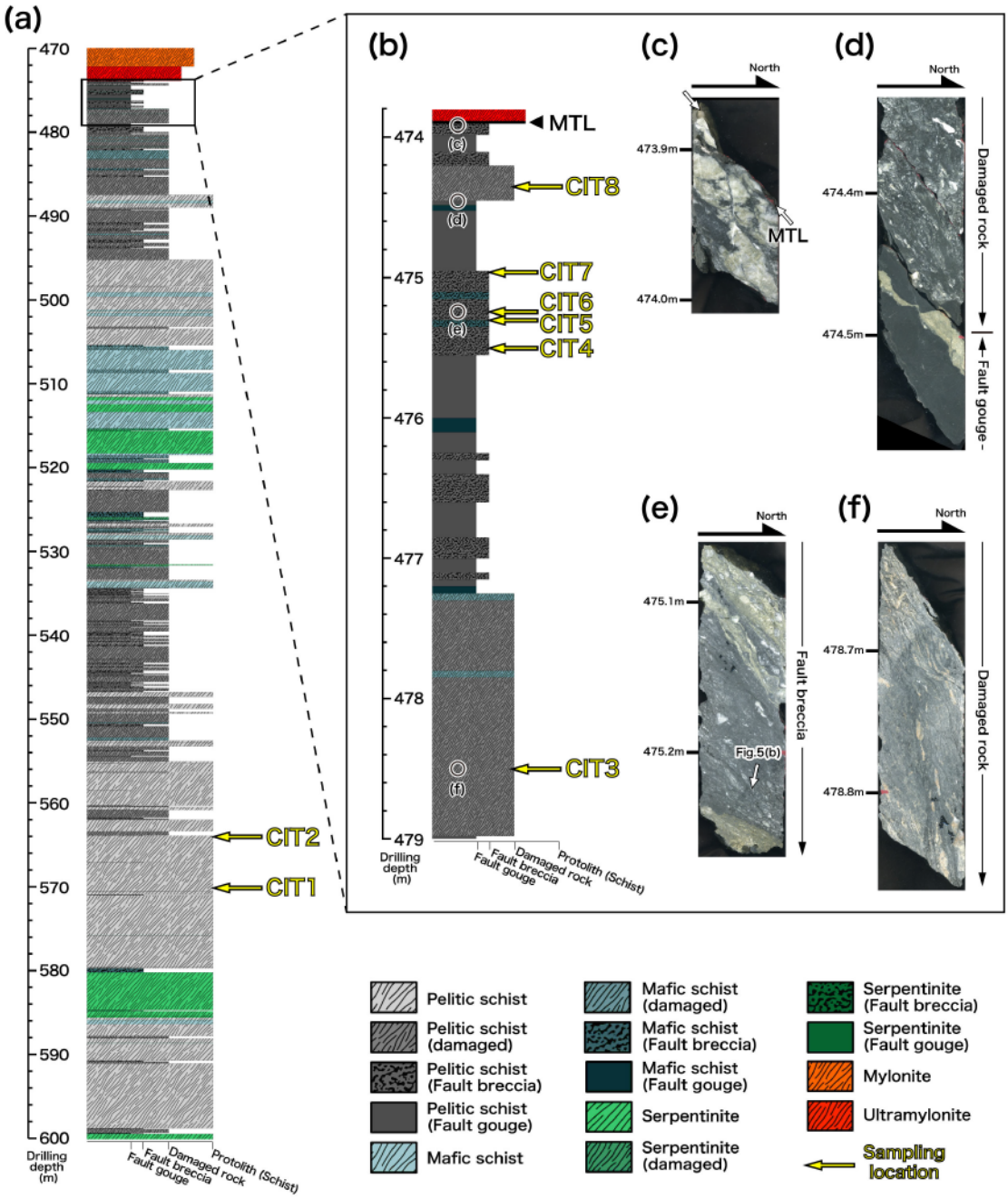

Figure 4. (a), (b) Columnar sections of the borehole (Hole1) core in parts of the Sanbagawa belt deeper than the MTL with sampling locations modified after Shigematsu et al. [2012]. (a) Log of the borehole core between drilling depths of 470 m to 600 m. (b) Detailed log between drilling depths of 473.8 m to 479.0 m. Photograph of borehole core samples between drilling depths of 470 m to 475 m, cross cutting the MTL at a depth of 473.9 m. (c)-(f) Photographs of borehole core samples in parts of the Sanbagawa belt nearby the MTL: Drilling depth of (c) 473.9 m to 474.0 m (immediately below the MTL), (d) 474.35 m to 474.55 m, (e) 475.1 m to 475.25 m, (f) 478.65 m to 478.8 m.

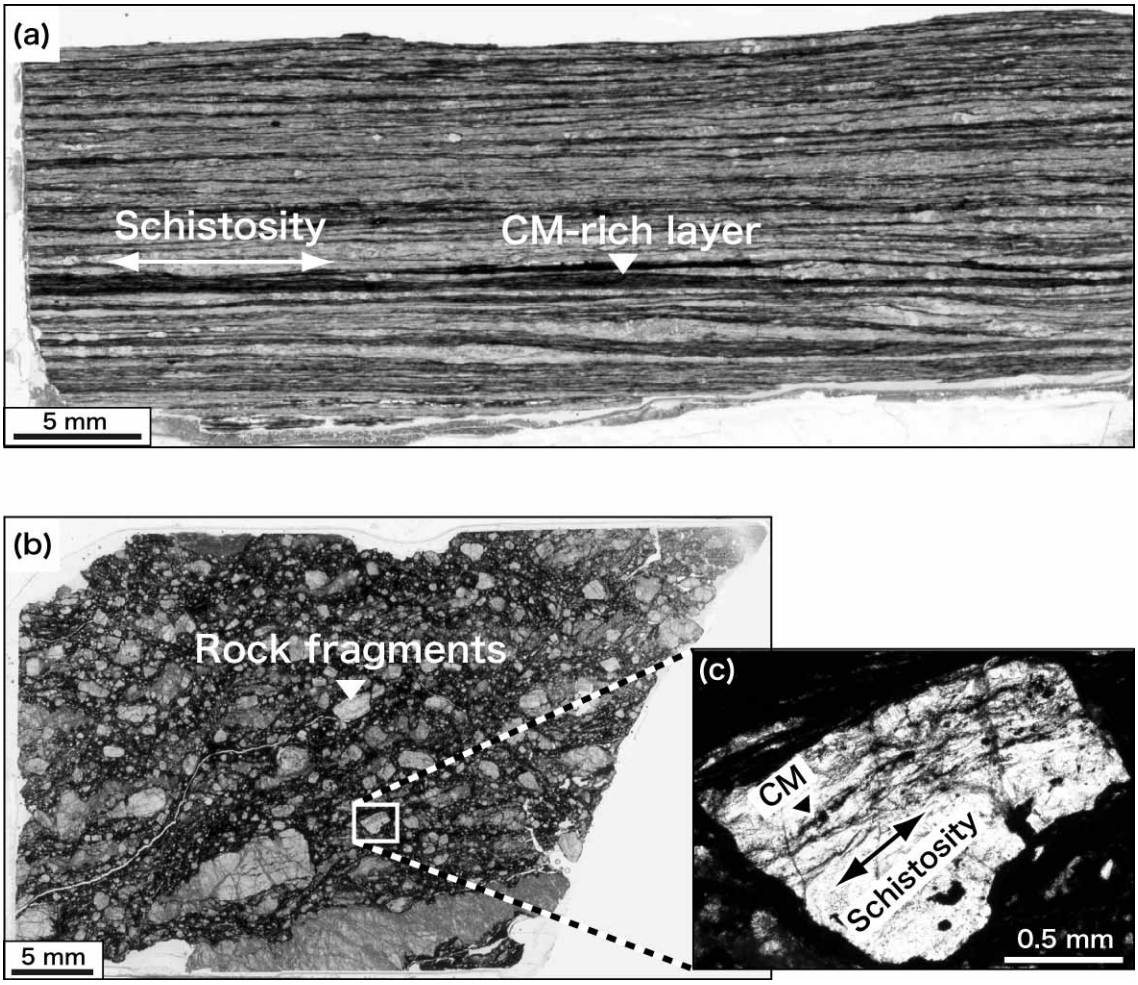

Figure 5. Photomicrographs of pelitic rocks. (a) Pelitic schist. (b) Fault breccia. The sampling point of (b) is shown in Figure 4e. (c) Close up of (b) showing rock fragment preserving schistosities. CM, carbonaceous-material.

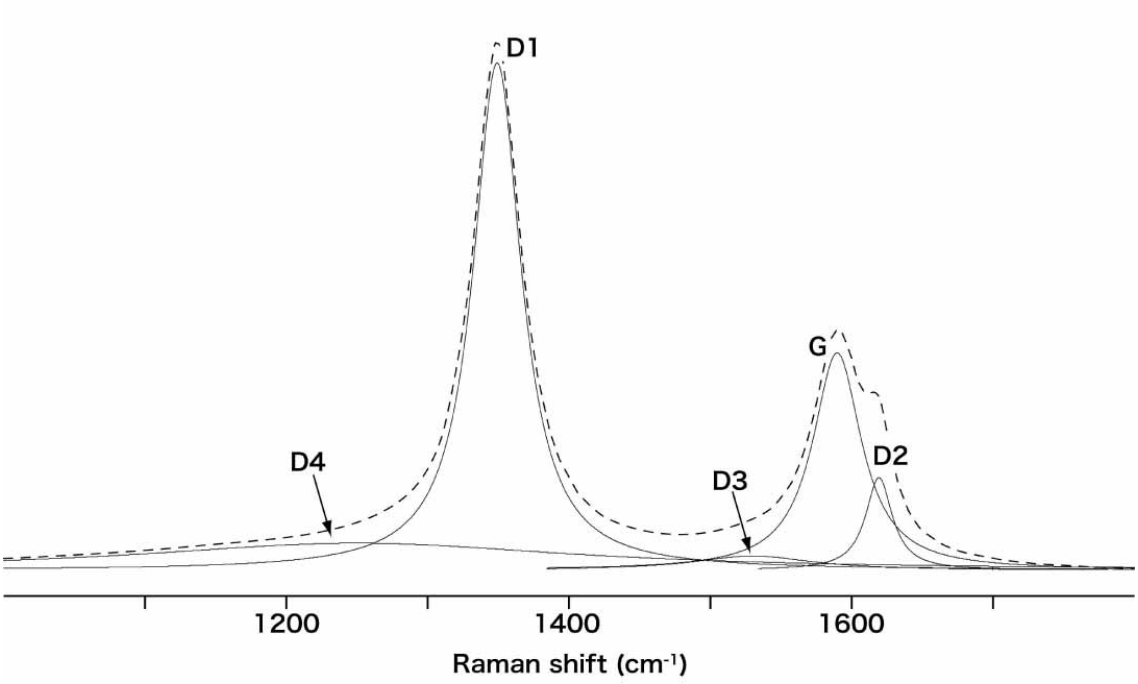

Figure 6. Schematic illustration showing an example of peak separation from a measured Raman spectrum (dashed line).

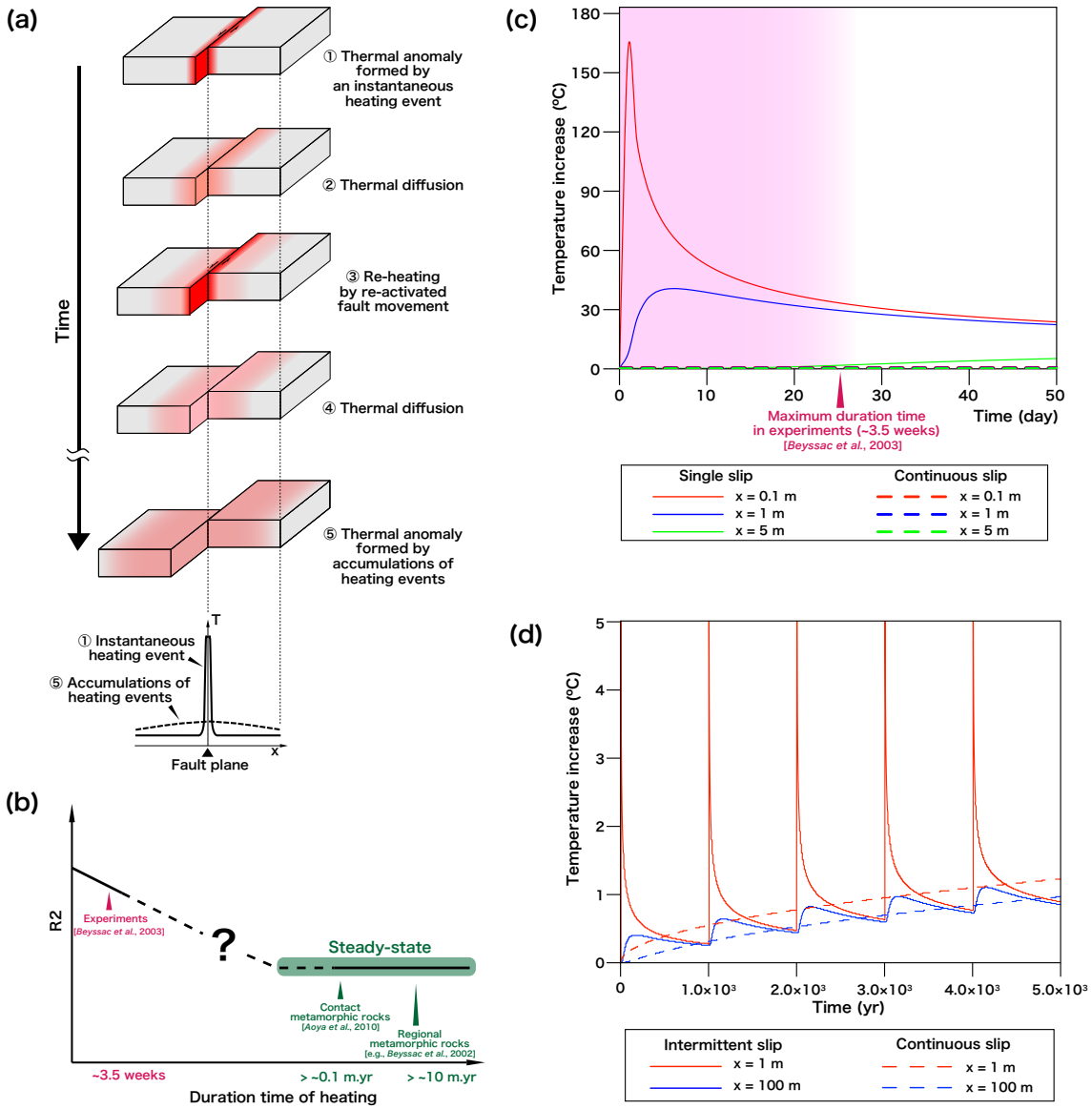

Figure 7. (a) Schematic diagrams showing formation histories of thermal anomalies around a fault formed by shear heating with instantaneous (a-1 and a-3) and accumulated thermal effects (a-4 and a-5), and the associated thermal structures perpendicular to the fault plane. (b) Schematic diagrams showing the relationships between R2 values and duration time of heating. (c), (d) Temperature profiles calculated by using equations (3), (5), and (6). (c) Temperature distributions versus time after a fault movement by using equation (3) and (6). Solid lines show the profiles calculated by using equation (3) and broken lines show the profiles by using the equation (6). Pink colored areas correspond to the range of time scales covered by of CM heating experiements (< ~3.5 weeks). No clear change in the R2 values of CM was observed in these experiments [Beyssac et al., 2003]. (d) Temperature distributions versus distance from the fault calculated by using equations (5) and (6). Solid lines show the profiles calculated by using equation (5) and broken lines show the profiles calculated by using the equation (6).

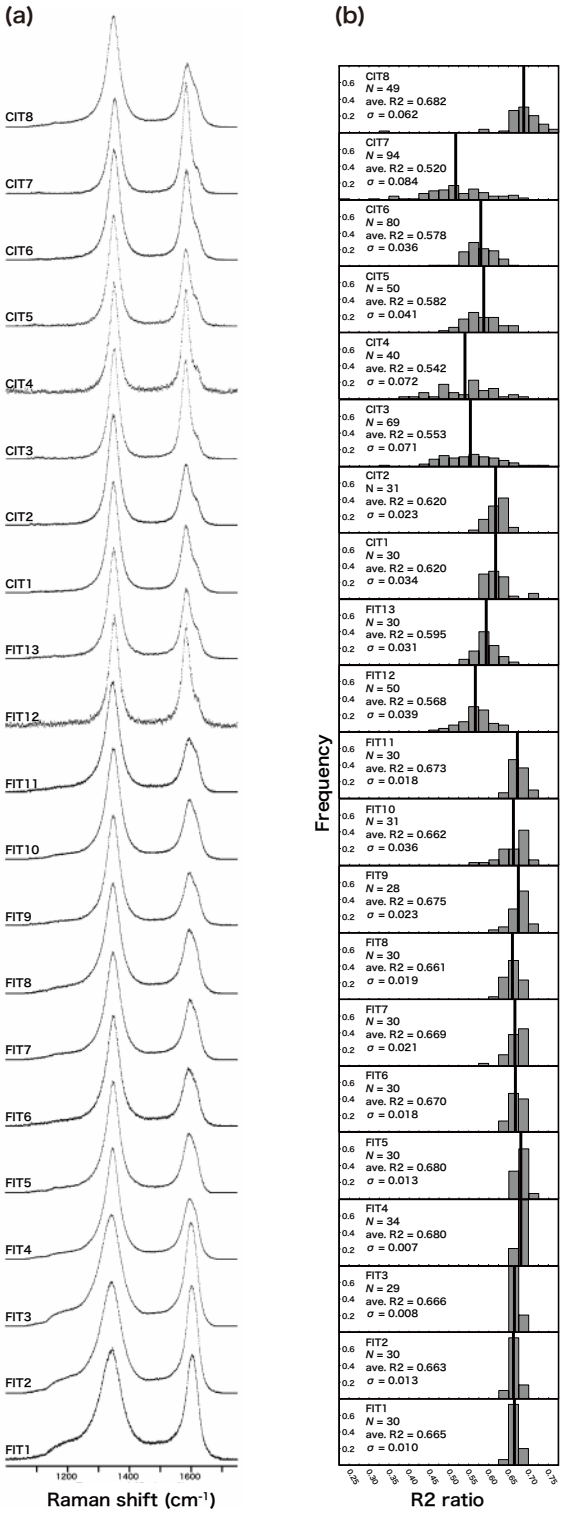

Figure 8. Raman spectra and R2 ratio. (a) Examples of Raman spectra obtained from all samples. (b) Histograms show the frequency distribution of R2 values in all samples. The average R2 values are indicated by solid lines. The total number of measurements is indicated by N. The vertical axis (normalized frequency) shows the proportion of measurements with respect to N.

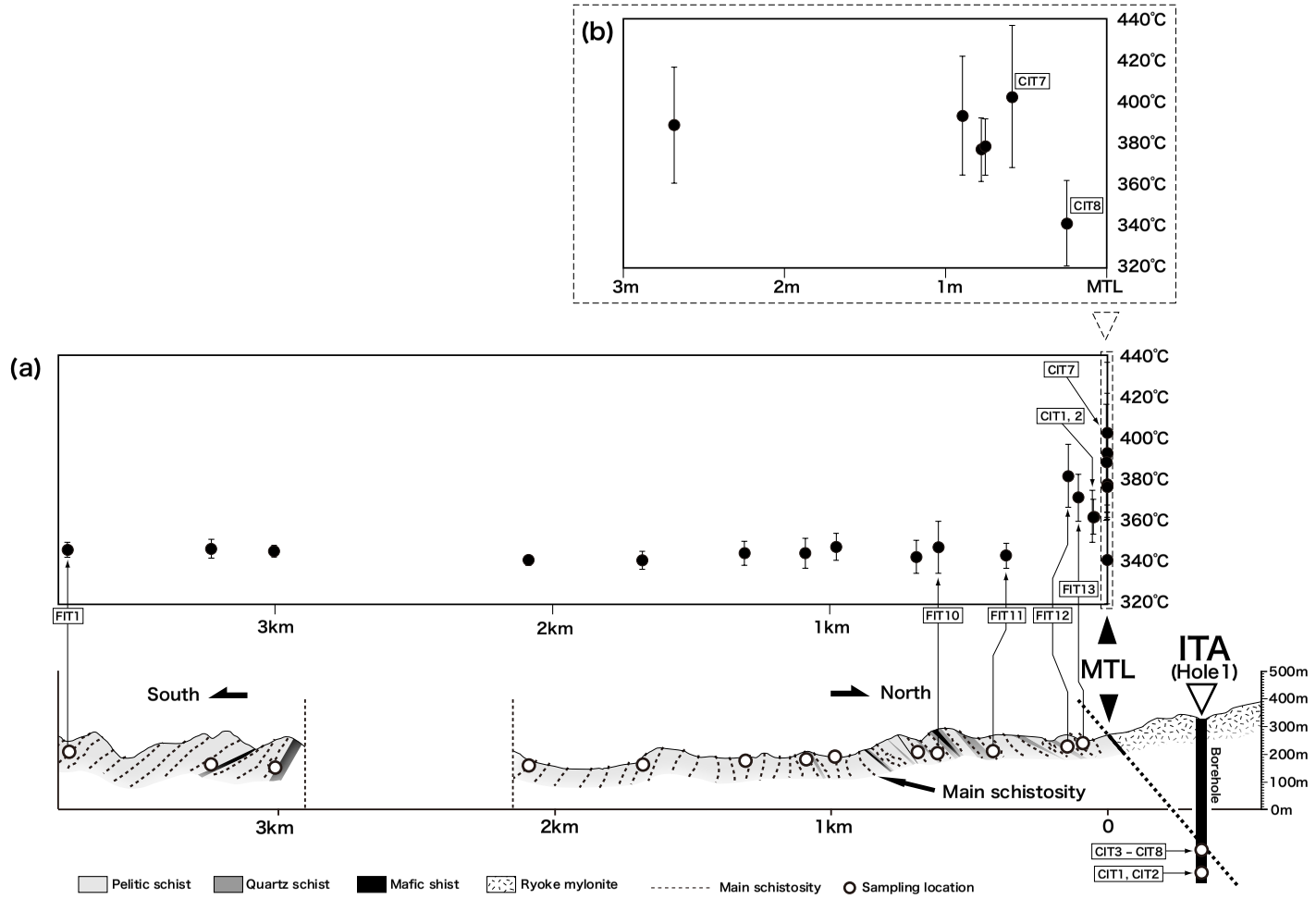

Figure 9. (a) Estimated temperatures of all samples versus distance from the MTL with the cross section of Figure 2d. (b) Close up of (a) showing plots within 3 m from the MTL (CIT3–8). Plots of estimated temperatures and their error bars represent the average and the standard deviation (1σ) of R2 converted to temperature, respectively. The locations of the samples over 600 m from the MTL (FIT1–10) in figure (a) are plotted as the horizontal distance from the trace of the MTL, and those of the samples within 600 m (FIT11-13, CIT1–8) in both of figures (a) and (b) are plotted as vertical distance from the fault plane as shown in Table 1.

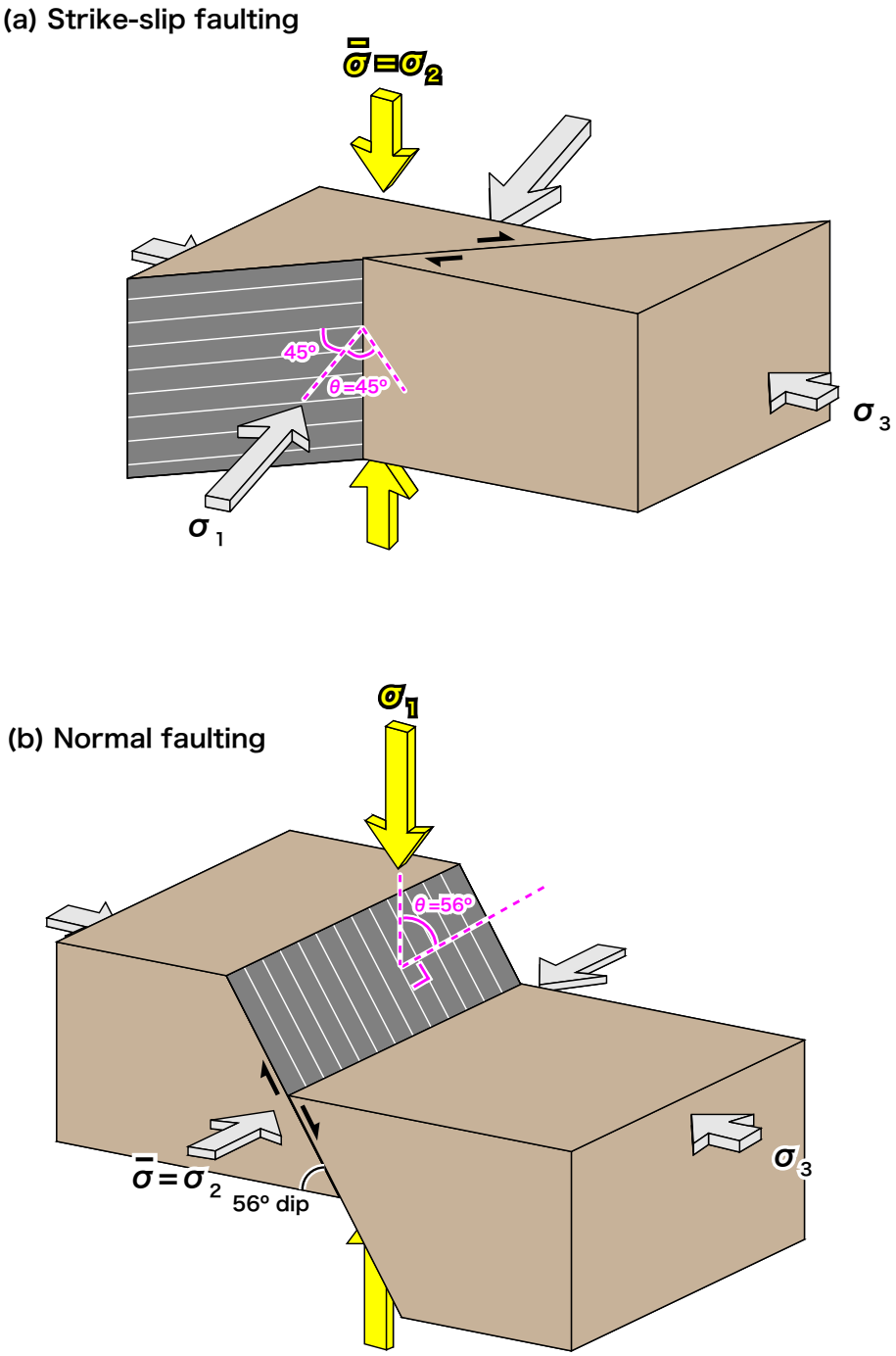

Figure 10. Schematic diagrams showing relationships between principal stresses and faulting types using Mohr's circle diagrams. (a) Strike-slip faulting. (b) Normal faulting.

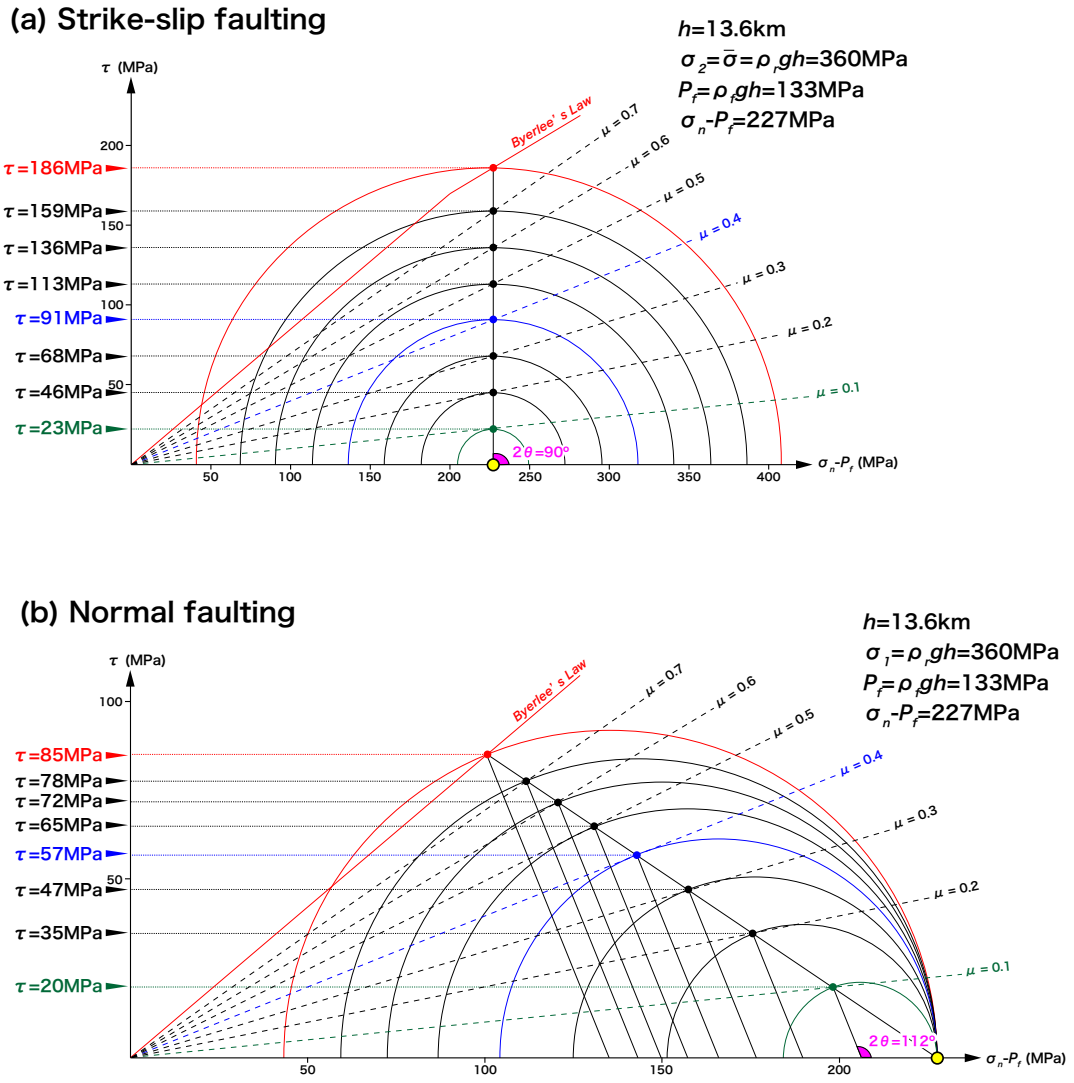

Figure 11. Mohr's circle diagrams used to estimate relationships between coefficients of friction and shear stresses for (a) strike-slip faulting, and (b) normal faulting.

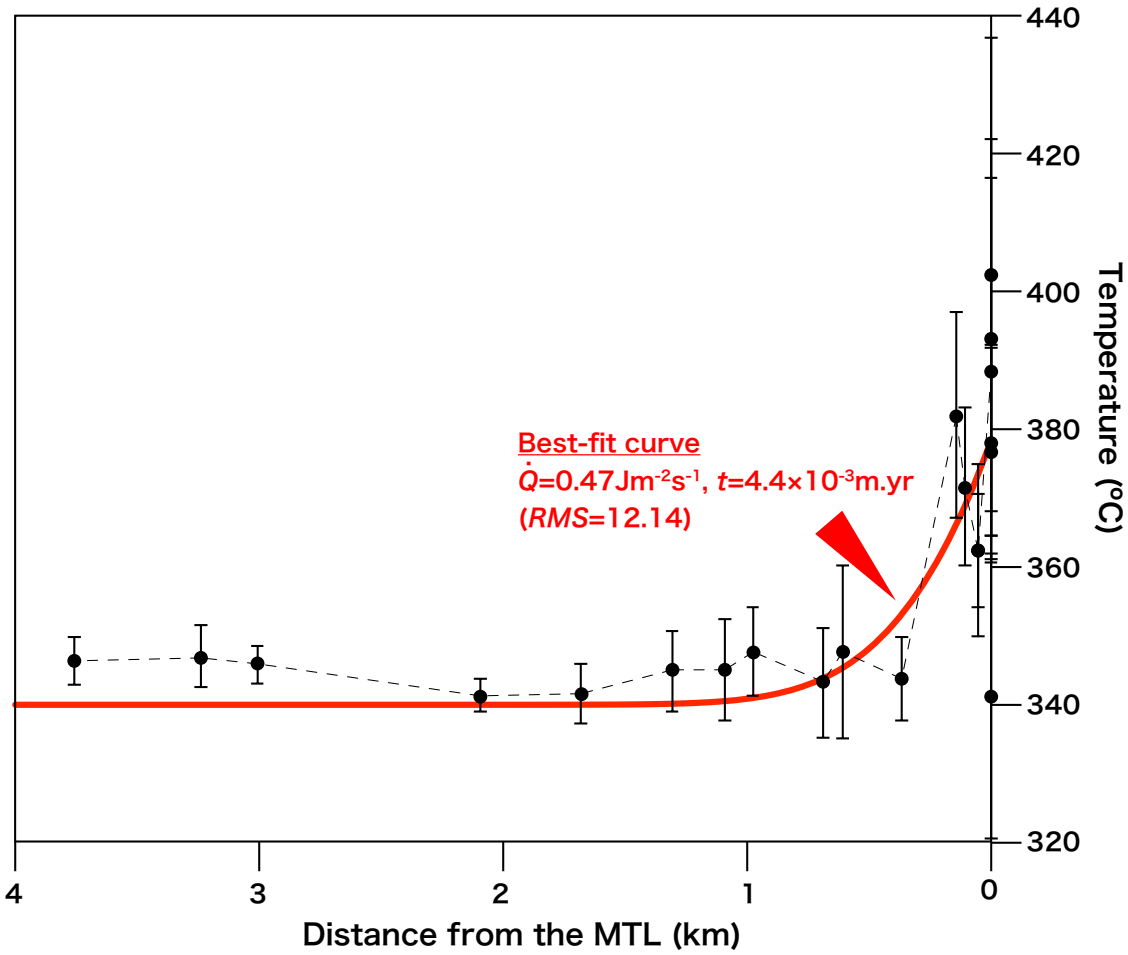

Figure 12. Temperature distributions versus distance from the fault calculated by using equation (6) with plots of estimated temperatures. The red line shows the profile of the best-fit solution for the values of estimated average temperatures, calculated by using a variety of values of and t. The plotted locations of the samples about the distances from the trace of the MTL are the same as Figure 9 as shown in Table 1.

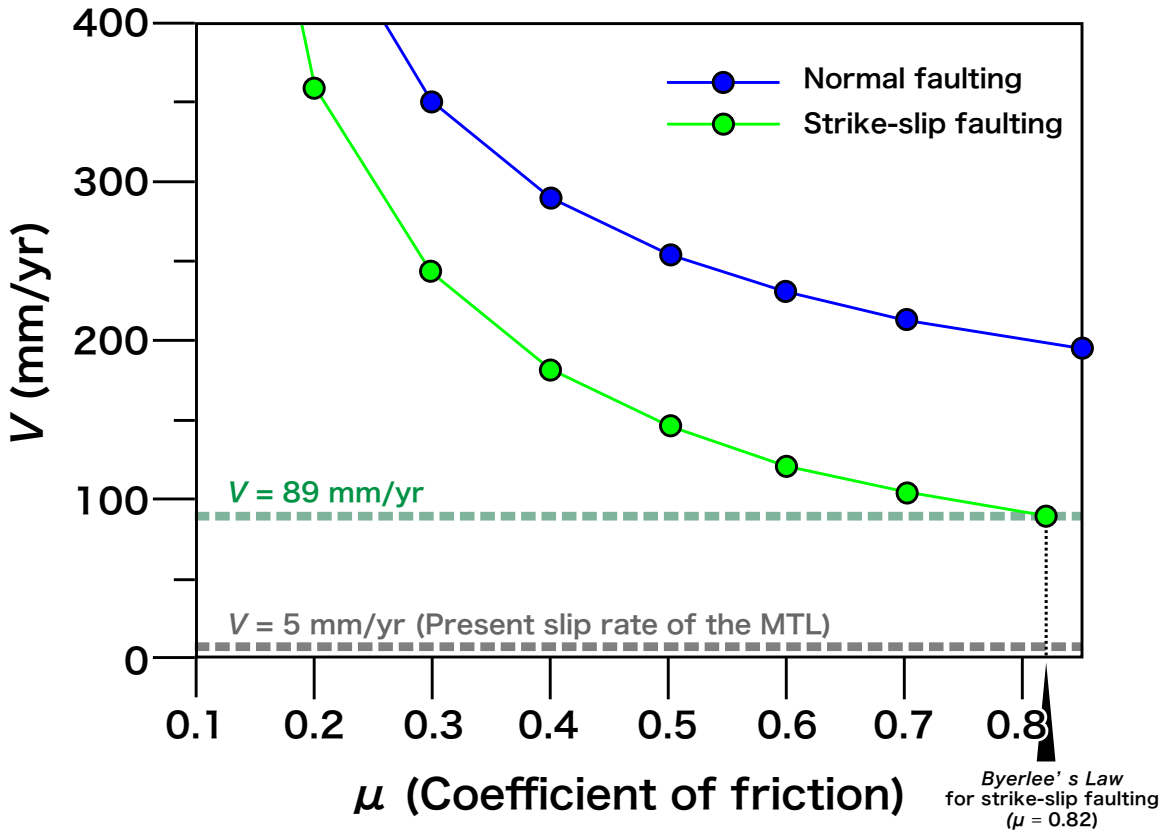

Figure 13. Relationships between μ and V calculated by using equation (1), which are required to fit the best-fit curve of Figure 12 for cases of both strike-slip and normal faulting. Green and gray broken lines show the minimum value of slip rate required to fit the best-fit curve for strike-slip faulting (V = 89 mm/year) and the present slip rate of the MTL (V = 5 mm/year), respectively.

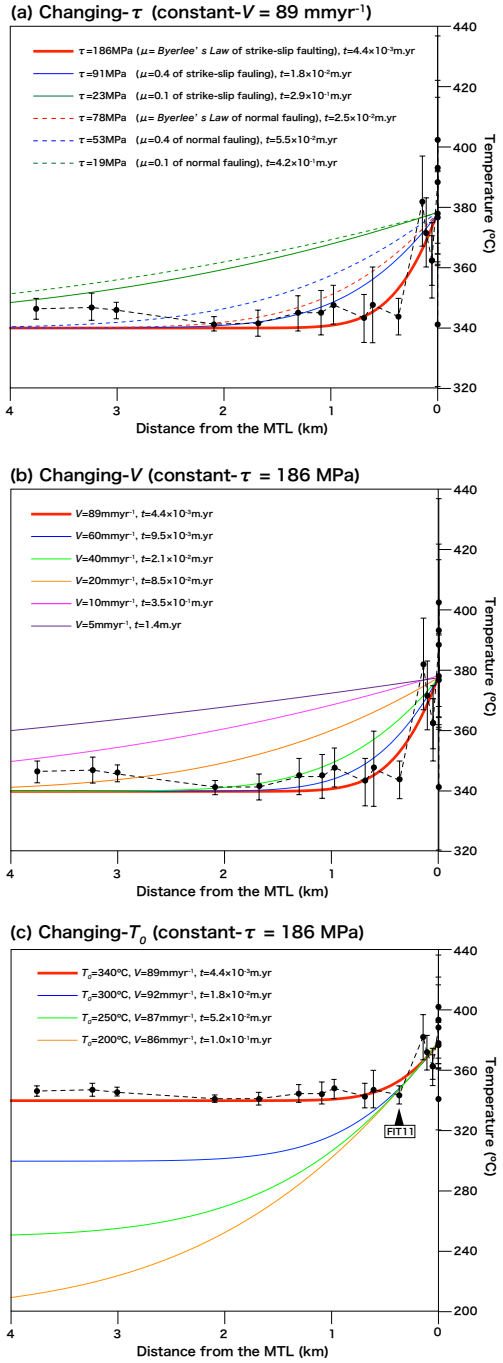

Figure 14. Temperature distributions versus distance from the fault calculated by using equation (6) with plots of estimated temperatures. (a) Profiles changing values of τ and t with a constant value of V = 89 mm/year to produce the same temperature rise of the best-fit solution (red line) nearby the fault. (b) Profiles for different values of V and t selected to produce the same temperature rise as shown by the best-fit solution (red line) nearby the fault. (c) Profiles of the best-fit solutions, calculated by using a variety of values of T0, V, and t for the values of estimated average temperatures. In order to fit the curves for T0 = 200 ºC, 250 ºC, and 300 ºC, we used the data for the high-T group and the temperature obtained from the low-T group closest to the MTL (FIT11–13, CIT1–8).

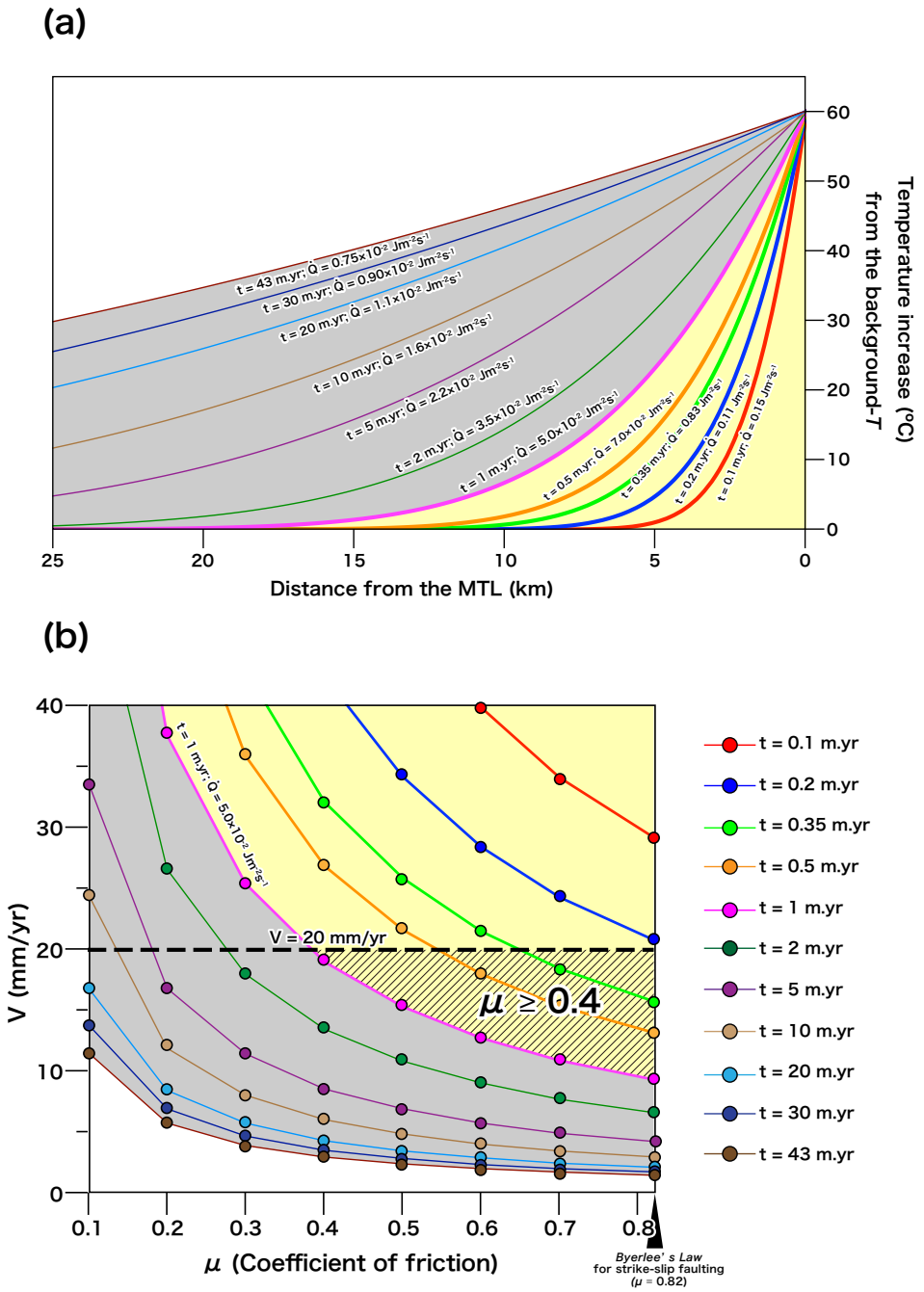

Figure 15. (a) Distributions of temperature increases from the background T (T0 = 340 ºC) versus distance from the fault calculated by using equation (6) with plots of estimated temperatures. All profiles are calculated to produce a temperature increase of 60 ºC from the background T at the fault plane (x = 0). Boundary between light yellow and gray areas is a profile of t = 1 million years which form a thermal anomaly with a width of ~20 km around the fault. (b) Relationships between μ and V calculated using equation (1), which are required to fit the profiles of Figure 15a for strike-slip faulting. Colors of lines and plots and filled areas are correlated to those of Figure 15a. Shaded areas show crossover rages between light yellow areas (t ≤ 1 million years, that is, widths of thermal anomalies are less than 20 km) and slip rates below 20 mm/year.

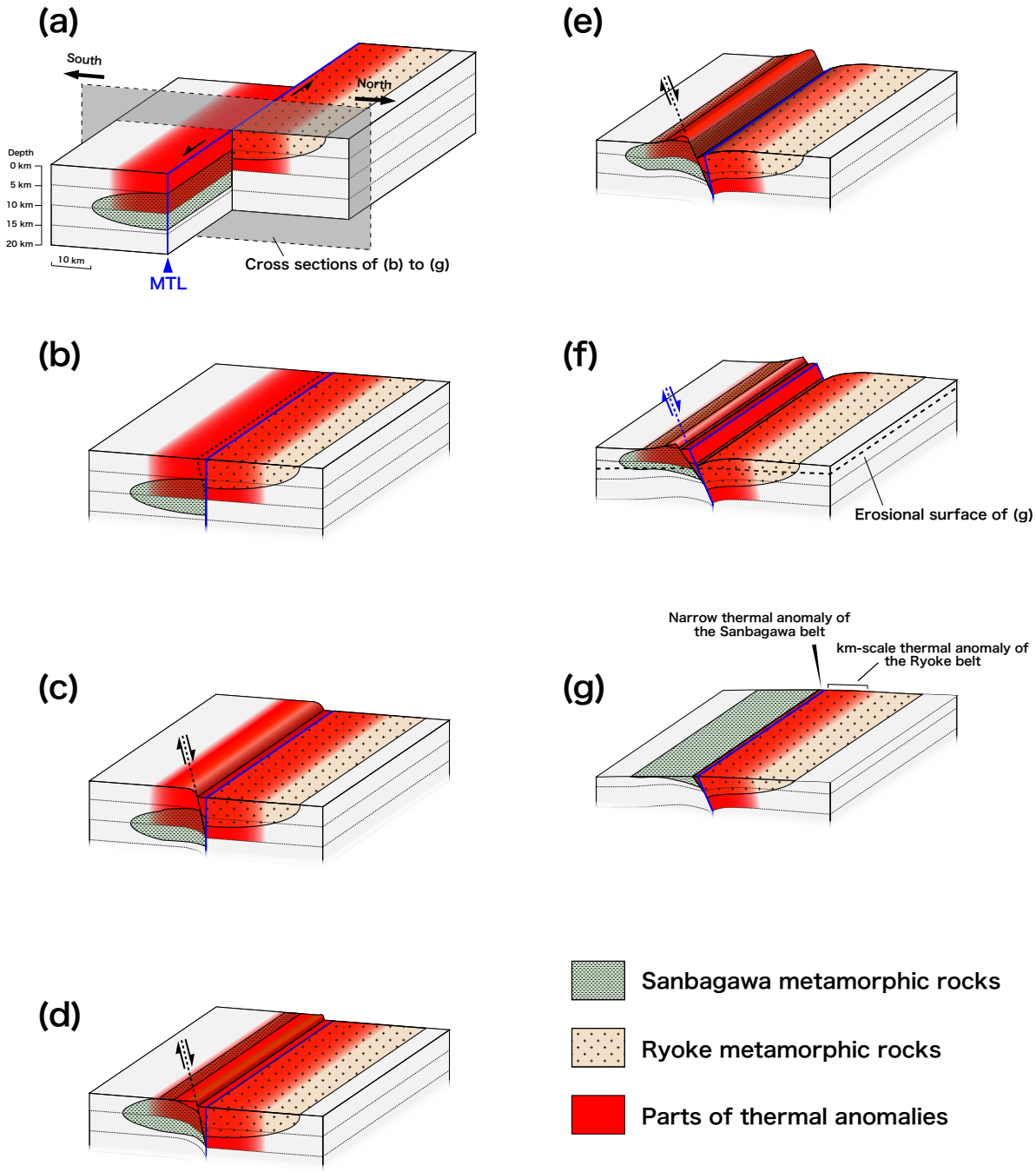

Figure 16. Schematic diagrams to show the tectonic evolution of the MTL, the Sanbagawa belt, and the Ryoke belt during period from (a-b) sinistral strike-slip faulting (> ~20 Ma), through (c-f) normal faulting of the MTL (~20 Ma–15 Ma) to (g) erosion.

Table 1. Results of Raman spectral analyses.

Sample	Horizontal distance from the surface of the MTL (m)	Vertical distance from the fault plane of the MTL (m)†	Rock type	N††	Average R2 (1σ)	T (ºC)
FIT1	3755	–	Schist	30	0.665 ± 0.010	346 ± 4
FIT2	3235	–	Schist	30	0.663 ± 0.013	347 ± 4
FIT3	3010	–	Schist	29	0.666 ± 0.008	346 ± 3
FIT4	2090	–	Schist	34	0.680 ± 0.007	341 ± 2
FIT5	1680	–	Schist	30	0.680 ± 0.013	341 ± 4
FIT6	1310	–	Schist	30	0.670 ± 0.018	345 ± 6
FIT7	1090	–	Schist	29	0.669 ± 0.021	345 ± 7
FIT8	980	–	Schist	30	0.661 ± 0.019	348 ± 7
FIT9	690	–	Schist	28	0.675 ± 0.023	343 ± 8
FIT10	610	–	Schist	31	0.662 ± 0.036	348 ± 13
FIT11	440	365	Schist	30	0.673 ± 0.018	344 ± 6
FIT12	170	141	Schist	50	0.568 ± 0.039	382 ± 15
FIT13	125	104	Schist	30	0.595 ± 0.031	372 ± 11
	Drilling depth from ITA (m)					
CIT1	570.10	54	Schist	30	0.620 ± 0.034	362 ± 13
CIT2	564.10	50	Schist	31	0.620 ± 0.023	362 ± 8
CIT3	478.70	2.68	Damaged rock	69	0.553 ± 0.071	389 ± 28
CIT4	475.50	0.89	Fault breccia	40	0.542 ± 0.072	393 ± 29
CIT5	475.30	0.78	Fault breccia	50	0.582 ± 0.041	377 ± 16
CIT6	475.25	0.75	Fault breccia	80	0.578 ± 0.036	378 ± 14
CIT7	474.95	0.59	Fault breccia	94	0.520 ± 0.084	402 ± 34
CIT8	474.35	0.25	Damaged rock	49	0.682 ± 0.062	341 ± 21

†Vertical distance from the fault plane of the MTL were calculated as the fault plane has 56 º northward dip which was determined from several outcrops of the MTL around ITA by Shigematsu *et al.* (2012).

††N, number of measurements.

Table 2. Material parameters and initial conditions for thermal calculations.

c	Specific heat	1000	$Jkg^{-1}K^{-1}$
$\kappa = k/c\rho_r$	Thermal diffusivity	9.3×10^{-7}	m^2s^{-1}
k	Thermal conductivity	2.5	$Wm^{-1}K^{-1}$
ρ_r	Density of rock	2700	kgm^{-3}
ρ_f	Density of fluid	1000	kgm^{-3}
G	Geothermal gradient	25	$°Ckm^{-1}$
$h = T_0/G$	Depth	13.6	km
g	Gravity	9.8	$kgms^{-2}$
e	Proportion of total work converted into heat	0.9	
T_0	Initial temperature	340	ºC

Part 3:
Thermal modeling of shear heating in the Ryoke belt around the MTL: implications for strength and displacement history of a major long-lived fault

Abstract

Documentation of the thermal structure around major faults can help constrain the fault strength operating when they move. A broad thermal anomaly more than several km-scale can be recognized in the Ryoke belt around the Median Tectonic Line (MTL) on the basis of previously reported fission track dating. One-dimensional heat conduction modeling for the dating in the Ryoke belt shows that this thermal anomaly can be accounted for by shear heating that developed during strike-slip faulting with a coefficient of friction > 0.22. This implies that the MTL is a relatively strong fault capable of significant amounts of shear heating. Constraints on displacement rates and duration imply displacements of several hundreds of km on the MTL.

1. Introduction

Long-lived major faults extend over hundreds of kilometers and are widely distributed in a variety of crustal domains such as continental strike-slip faults, oceanic transform faults, and subduction boundaries. These faults play a significant role in regional tectonic evolution and large-scale crustal deformation. Making reliable estimations of the strengths of major faults, in other words, the shear stresses (τ) or coefficients of friction (μ) acting on them, is an important part of developing a better understanding of crustal strengths and the generation of large earthquakes, and the extent to which shear heating associated with movement on faults is a significant heat source for regional metamorphism [e.g., *Scholz*, 1980; *Molnar and England*, 1990]. However, despite considerable research on this important topic, there is still no good consensus on the strength of these major tectonic boundaries.

Deformation experiments show that mechanical work during fault movement is largely converted into heat energy typically with an efficiency (e) of more than 90% [e.g., *Lockner and Okubo*, 1983]. The amount of heat energy can be expressed as

$$\dot{Q} = e\tau V = e\mu\sigma_n V \quad (1)$$

where $\dot{Q}$ is the heat flow per unit area by a fault movement ($Jm^{-2}s^{-1}$), τ is the average shear stress (Pa), V is the slip rate of the fault movement (ms^{-1}), μ is the coefficient of friction, and σ_n is the normal stress (Pa). Quantification of heating generated by fault movement (shear heating) therefore has the potential to help in estimating the shear stresses that operate on faults when they move and also rates of displacement.

Rock deformation experiments show that the shear stress needed to cause displacement in fault zones is largely independent of rock type [*Byerlee*, 1978] and predict significant amounts of shear heating along long-lived faults. Nevertheless, detailed studies for surface heat flow measurements [e.g., *Brune et al.*, 1969; *Lachenbruch and Sass*, 1980] and thermochronology [*d'Alessio et al.*, 2003] in the vicinity of the major San Andreas Fault (SAF) have not revealed any clear evidence for the expected shear heating. These results are commonly used to infer the SAF is a weak fault that supports lower shear stress than that expected based on *Byerlee's Law*. This mismatch between experimental work and observation of natural faults is commonly referred to as the *"Stress–Heat flow Paradox"*.

A number of physical mechanisms have been proposed to explain the weakness of major faults including dynamic weakening models for the reduction of the dynamic friction value during slip by such as dynamic thermal pore pressure enhancement [e.g., *Sibson*, 1973], acoustic fluidization [*Melosh*, 1996], or dynamic lubrication [e.g., *Brodsky and Kanamori*, 2001], and explanations have also been proposed based on the presence of weak material along the fault [e.g., *Moore and Rymer*, 2007] or the influence of low permeability structures that cause elevated pore pressures along the fault [e.g., *Rice*, 1992]. An alternative explanation is that faults such as the SAF do support stresses consistent with *Byerlee's Law* and the lack of a thermal anomaly is due to relatively rapid transport of heat away from the fault zone by heat advection due to crustal fluid circulation. The result of such a process is likely to be that any thermal anomaly present would be spread over such a wide area that it is no longer observable [e.g., *O'Neil and Hanks*, 1980; *Williams and Narasimhan*, 1989; *Scholz*, 2000].

The Median Tectonic Line (MTL)—the largest on-land fault in Japan—separates the Ryoke high-*T/P* type metamorphic belt with granitic rocks to the north from the Sanbagawa belt associated with subduction-type high-*P/T* metamorphism to the south (Figure 1). The size and duration of movement recognized along the MTL make this a

good candidate for a comparison with the SAF.

In three regions of the Ryoke belt (RM-, RC- and RN-traverses in figure 1), the presence of relatively young apatite fission track (Ap-FT) ages localized close to the MTL has been interpreted as evidence for shear heating [*Tagami et al.*, 1988]. Recently reported FT and (U–Th)/He ages also show relatively young ages close to the MTL, and *Sueoka et al.* [2011, 2012] interpret these ages as the result of locally rapid erosion of the Ryoke belt rather than shear heating. I cannot exclude this possibility, however, there is no evidence for the large accommodating faults associated with the putative large differential uplift. In addition, microstructural studies of mylonitic rocks from the Ryoke belt nearby the MTL give evidence for high differential stresses compatible with a high-integrated strength for the fault [*Okudaira and Shigematsu*, 2012; *Shigematsu et al.*, 2012]. Strong faults will produce significant amounts of shear heating when they move and here I investigate the implications for fault strength, slip rate and accumulated displacement assuming that the thermal anomaly is due to such shear heating.

2. Outline of the MTL

The MTL stretches over a distance of >800 km and separates the Ryoke and Sanbagawa belts (Figure 1) [*Isozaki and Itaya*, 1990; *Takasu and Dallmeyer*, 1990; *Nakajima*, 1994; *Suzuki and Adachi*, 1998; *Wallis et al*, 2009]. The oldest recorded movements on the MTL are sinistral strike-slip in the Cretaceous [e.g., *Ichikawa*, 1980; *Miyata et al.*, 1980; *Takagi*, 1986; *Shimada et al.*, 1998]. A significant phase of normal faulting occurred in the middle Miocene (~20-15 Ma) [e.g., *Takagi et al.*, 1992; *Takahashi et al.*, 2006; *Fukunari and Wallis*, 2007]. The most recent movements are dextral strike-slip [e.g., *Huzita*, 1980; *Okada*, 1980; *Fukunari and Wallis*, 2007; *Kubota and Takeshita*, 2008].

3. Results of Fission Track Dating in the Ryoke Belt

Tagami et al. [1988] determined fission track (FT) ages in the Ryoke belt by using apatite (Ap) and zircon (Zr) samples collected from three traverses: the RN-, RC-, and RM-traverses (Figure 1). In all three traverses, Zr-FT ages are roughly constant at ~60 Ma. Far from the MTL, Ap-FT analyses yields a consistent slightly younger cooling age of ~54 Ma. However, close to the MTL, the Ap-FT ages reduce to ~11–29 Ma. *Tagami et al.* [1988] conclude that the reduction of Ap-FT ages is due to shear heating along the

MTL, but there has been no study trying to relate this to shear heating. Resetting of Ap-FT ages requires a temperature above the associated annealing zone of ~105 ºC [e.g., *Harrison and McDougall*, 1980]. No resetting of the Zr-FT ages was recognized implying that the temperature rise did not reach the annealing zone for Zr of around 240°C [e.g., *Hurford*, 1986]. Shear heating in the Ryoke belt, therefore, reached values between 105°C and 240°C. The thermal anomaly recorded in the RC-traverse is the broadest (~15 km; Figures 1 and 2) and this can be considered as the area with the largest amount of shear heating and/or the area with the best-preserved thermal anomaly. I therefore use the data of the RC-traverse for my calibrations.

4. Thermal Modeling

4.1. Calculation Equations for Thermal Modeling

A single fault movement is a geologically instantaneous event, and the associated shear heating causes rocks around the fault to experience high temperatures only during a very short period. In contrast, long-lived faults develop by repeated movements on geological time-scales, and the associated thermal anomaly represents the gradual accumulation of numerous individual heating events. Therefore, rocks around long-lived faults may undergo a series of pulses of heating on short time scales and a lower temperature more widely spread heating on longer time scales. Laboratory experiments show that FT ages in Ap can be completely reset by heating events as short as a few tens of minutes if the temperature exceeds ~400 ºC [*Green et al.*, 1986]. High temperatures can be generated for short time scales during a single fault movement. However, as discussed in part 2 distributions of temperatures high enough to affect FT in Ap are restricted to a zone a few cm wide (Figure 7c in PART 2). The width of this zone is insignificant where compared to the observed km-scale thermal anomalies, suggesting that to account for km-scale thermal anomalies such as those detected by *Tagami et al.* [1988] by shear heating requires consideration of fault movements on geological time scales. In addition, the long-term temperature profiles can be closely approximated by the results of continuous slip with main exceptions in the time immediately after movement and in areas very close to the faults zone (Figure 7d in PART 2). I therefore use following equation which assumed that a fault acts with a continuous slip rate to model the broad thermal anomaly in the Ryoke belt:

$$T(x,t) = \frac{\dot{Q}}{c\rho_r}\left(\frac{t}{\pi\kappa}\right)^{\frac{1}{2}} e^{-\frac{x^2}{4\kappa t}} - \frac{\dot{Q}|x|}{2c\rho_r\kappa} erf\,\frac{|x|}{2\sqrt{\kappa t}} + T_0 \qquad (2)$$

where $\dot{Q}$ is the heat flow per unit area caused by a fault movement with a constant slip rate (equation 1), c is specific heat, ρ_r is rock density, κ is thermal diffusivity, and T_0 is the initial temperature.

4.2. Parameter Constraints and Estimates

I determined the $\dot{Q}$ and t required by using equation (2) to reproduce thermal profiles that correlate with the distributions of the young and old Ap-FT ages (broken lines in Figure 2). The annealing temperature of apatite FT is taken to be 105 ºC. I then seek the relationships between V and μ (or τ) that are required to reproduce the appropriate value of $\dot{Q}$ by using equation (1).

The material parameters and initial conditions for calculations are shown in Table 1. To estimate the values of the initial temperature (T_0) and the corresponding depth (h) I first examine the cooling history. The Ap-FT ages imply that the MTL fault movements with shear heating occurred between ~54 Ma–17 Ma (Figure 2). This allowed me to place maximum values on t for the calculations of t_{max} = 37 million years (Figure 2). From the old Ap-FT age (54 Ma) and the annealing temperature (T_{ann} = 105 ºC), *Tagami et al.* [1988] estimated a cooling rate (R_c) of the Ryoke rocks of ~1.7 ºC/Ma from ~54 Ma to the present. By assuming a constant cooling rate and a geothermal gradient of G = 25 ºC/km (Table 1), I can estimate the temperature (T) and depth (h) relationships starting at 54 Ma and continuing until 17 Ma: $T_{54Ma} = T_{ann}$ =105 ºC and $h_{54Ma} = T_{54Ma} / G$ = 4.2 km; $T_{17Ma} = T_{54Ma} - R_c \times t_{max}$ = 42 ºC and $h_{17Ma} = T_{17Ma} / G$ = 1.7 km. A more complete calculation would include the effects of exhumation associated with decreasing ambient temperatures and normal stress. However, this history is not well constrained and I am mainly concerned with order of magnitude estimates, so I use time-averaged values for T_0 and h: $T_0 = (T_{54Ma} + T_{17Ma}) / 2$ = 74 ºC and $h = (h_{54Ma} + h_{17Ma}) / 2$ = 2.9 km.

In addition to the well-documented strike-slip movements [e.g., *Ichikawa*, 1980; *Miyata et al.*, 1980], recent studies of the MTL have also revealed significant normal displacements [e.g. *Fukunari and Wallis*, 2007; *Kubota and Takeshita*, 2008]. Therefore, I estimated relationships between shear stress (τ) and coefficient of friction (μ) for both normal and strike-slip movement (Figure 3). I assume that one of the principal stresses

is vertical and equal to the overburden pressure ($\rho_r gh$, where g is the acceleration due to gravity; Table 1); for strike-slip faulting this is the intermediate principal stress (σ_2), which is assumed to be equal to the average of the maximum and minimum principal stresses ($\sigma_2 = \bar{\sigma} = (\sigma_1 + \sigma_3)/2$), and for normal faulting this is the maximum principal stress (σ_1). For simplicity, the angle between σ_1 and the orientation of the fault plane (θ) is assumed to be 45º for strike-slip faulting (Figure 3a) and taken to be 56º, which is the present attitude of the MTL [*Shigematsu et al.*, 2012] for normal faulting (Figure 3b). *Fukunari et al.* [2011] suggest that fluid pressure was significantly below lithostatic pressure during brittle deformation of the MTL based on a significant discrepancy between fluid inclusion isochores and the retrograde *P–T* paths for solid rock samples. Therefore, I take the pore fluid pressure (P_f) to be hydrostatic pressure at the depth (h): $P_f = \rho_f gh$, where ρ_f is the density of fluid (Figure 3 and Table 1). I estimate the values of τ that correspond to a range of possible values of μ from 0.1 representing weak faults to *Byerlee's Law* ($\tau = 0.6 \times (\sigma_n - P_f) + 50$ for $\sigma_n - P_f \leq 200$ MPa) representing the upper limit on the strength (Figure 3). For strike-slip faulting, this range of values of μ corresponds to average values of shear stress τ from 5 MPa to 44 MPa (Figure 3a). Values of τ for normal faulting were estimated to be from 4 MPa to 19 MPa (Figure 3b).

5. Results of Thermal Modeling

The amount of shear heating is proportional to both shear stress (τ) or coefficient of friction (μ) and rate of displacement (V) (equation 1). In addition, the effects of shear heating are cumulative and so the peak-attained temperature (T) is proportional to both the duration of slip (t) and the rate of displacement (V) (equation 2). The thermochronological data from the Ryoke belt give maximum values for the duration of shear heating (t_{max} = 37 million years; Figure 2), so it is possible to consider the thermal results in terms of coefficient of friction (μ) and total displacement ($V \times t$).

The model results for cases of both strike-slip and normal faulting are shown in Figures 4a and 4b respectively. The results of normal faulting show that even for high values of μ operating on the MTL, displacement rates have to exceed 10 mm/year (Figure 4b) to account for the observed thermal anomaly. This rate is the maximum observed value for long-term displacement on major normal faults [e.g., *Hodges et al.*, 1998]. In addition, the total displacement on such normal faults would have to exceed 100 km. Such large extensional displacements on normal faults should cause

exhumation of lower crustal material. This is not seen and I conclude that the shear heating effects cannot be accounted for by normal displacements on the MTL alone.

Large displacements can be achieved by strike-slip faults without causing burial or exhumation of the footwall material. The present day rate of displacement on the MTL is 5 mm/year [e.g., *Tabei et al.*, 2002, 2003]. In cases of strike-slip faulting, this rate can account for the shear heating effects in the Ryoke belt if the MTL closely obeys *Byerlee's Law* (Figure 4a). If displacement rates were higher at the time of shear heating then weaker faults are also compatible with the data.

The MTL formed at the rear of a Cretaceous convergent plate boundary. *Jarrard* [1986] compile slip-rate data for similar strike-slip faults that are commonly found at the rear of oblique convergent margins and show that for moderate rates of plate convergence the rate of displacement is a function of obliquity. For degrees of obliquity less than ~50 degrees there is a range of slip rates up to ~20 mm/year (Figure 5a) [*Jarrard,* 1986].

The motion of plates in the Pacific realm is quite well known for the period of time relevant to my study (54-17 Ma) [e.g., *Engerbretson*, 1985]. To compare to the results of *Jarrard* [1986], I re-calculated the motion vector for the Pacific plate from 54 Ma to the 17 Ma (Figure 5b) using the stage poles given in *Engerbretson* [1985] based on the global circuit of plate motions (rather than assuming a fixed hot spot reference frame). The results show that the obliquity of convergence did not exceeded 50 degrees with the possible exception of a short period of approximately 3 million years (50–48 Ma; Figure 5b).

This review of former plate motion and slip rates on strike-slip faults implies that rates of strike-slip movement on the MTL during the period of shear heating are unlikely to have exceeded 20 mm/year. Taking 20 mm/year as an upper bound for the long-term slip rate on the MTL implies that the recognized shear heating is compatible only for faults with a coefficient of friction > 0.22 (shaded areas in Figure 4a).

Maintaining a slip rate of 20 mm/year over the period recorded by the fission track ages ($\leq t_{max}$ = 37 million years) implies a strike-slip displacement on the MTL of 740 km. The true displacement on the MTL is not well known, but any estimate that implies a lower long-term slip rate or lesser amounts of displacement (and by implication shorter duration times) would imply a stronger fault. A minimum estimate for the displacement on the MTL can also be derived from my studies. The maximum effects of

shear heating occur for the strongest faults. Assuming the MTL obeys *Byerlee's Law* and setting the displacement rate at a level that just allows sufficient shear heating allows me to derive a minimum average slip rate or ~5 mm/year (Figure 4a). This is close to the present day observed value and implies a displacement of 185 km.

6. Discussion

6.1. Comparisons with Weak Fault Models of the MTL

The recognition of thermal anomalies associated with shear heating around the MTL [*Tagami et al.*, 1988] are in contrast to the San Andreas Fault, which lacks any clear thermal anomaly and imply the MTL is a relatively "strong" fault. These are in good agreement with stress estimates of ~280 MPa at 300 ºC based on recrystallized grain size of quartz in the Ryoke mylonites [*Okudaira and Shigematsu*, 2012]. However, several other studies have used microstructural observations of phyllonite in the Ryoke belt and measurements of gouge permeability in the Sanbagawa belt to infer that the MTL is a "weak" fault [e.g., *Wibberley and Shimamoto*, 2003, 2005; *Holdsworth*, 2004; *Jefferies et al.*, 2006a, 2006b; *Imber et al.*, 2008] with proposed values of $\mu \leq$ ~0.2—which require displacement rate more than 20 mm/year and total displacement of > 800 km to account for the relationships of μ–V (Figure 4a). Therefore, the evidence for low shear stresses on the MTL requires some explanation. High shear stresses and large amounts of shear heating should show an overall increase with depth up to the brittle-ductile transition at depths of several kilometers. The evidence for weak faulting may in part reflect the development of such features at relatively shallow depths. In addition, weak faults as discussed above may also reflect domains of weakness restricted in space and/or time. Reconciling these opposed inferences about the strength of large-scale faults is an important topic for future studies.

6.2. Importance of Large-scale Strike-slip Faulting along the MTL for Tectonic Development of Sanbagawa and Ryoke Belts

The results of the present study suggest that large-scale strike-slip faulting with a total displacement of several hundreds of kilometers has occurred along the MTL during late Cretaceous to Miocene. *Miyashiro* [1961] proposed that the high-pressure Sanbagawa and low-pressure Ryoke metamorphic belt represent one set of "paired metamorphic belts" and that similar features occur in many parts of the circum-Pacific

region. These two types of metamorphic belts can be correlated with the low heat flow subduction part of a plate boundary (Sanbagawa belt) and the high heat flow continental volcanic part (Ryoke belt) of modern convergent plate boundaries [*Miyashiro*, 1973]. However, a significant problem is that the Sanbagawa and Ryoke belts are adjacent and not separated by 100-200 km as in the modern system. It has been suggested that large-scale strike-slip faulting may have excised this forearc region [e.g., *Miyashiro*, 1972; *Brown*, 1998]. My results confirm the importance of large-scale strike-slip faulting along the MTL.

7. Conclusions

1. Previously reported thermochronological data from the Ryoke belt show kilometer-scale high-*T* domains adjacent to the MTL that can be interpreted as due to shear heating.
2. Thermal modeling shows that the effects of shear heating recorded around the MTL are best explained by a fault zone that has a coefficient of friction > 0.22 implying the MTL is a relatively strong long-lived major fault.
3. The thermal anomalies by shear heating around the MTL require large-displacements between 185 and 740 km. Such large displacements are best accounted for by strike-slip faulting.

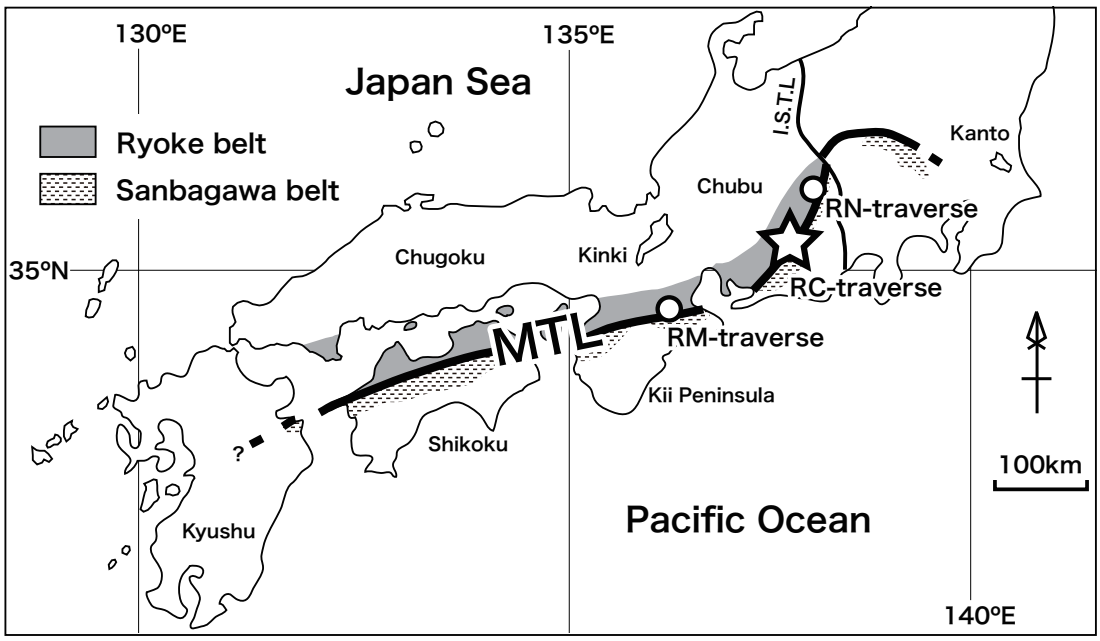

Figure 1. Distribution of the Median Tectonic Line, the Ryoke and Sanbagawa belts [after Isozaki, 1996]. Small circles (RM- and RN-traverses) and star symbol (RC-traverse) are the study areas by Tagami et al. [1988]. MTL, Median Tectonic Line; I.S.T.L, Itoigawa-Shizuoka Tectonic Line.

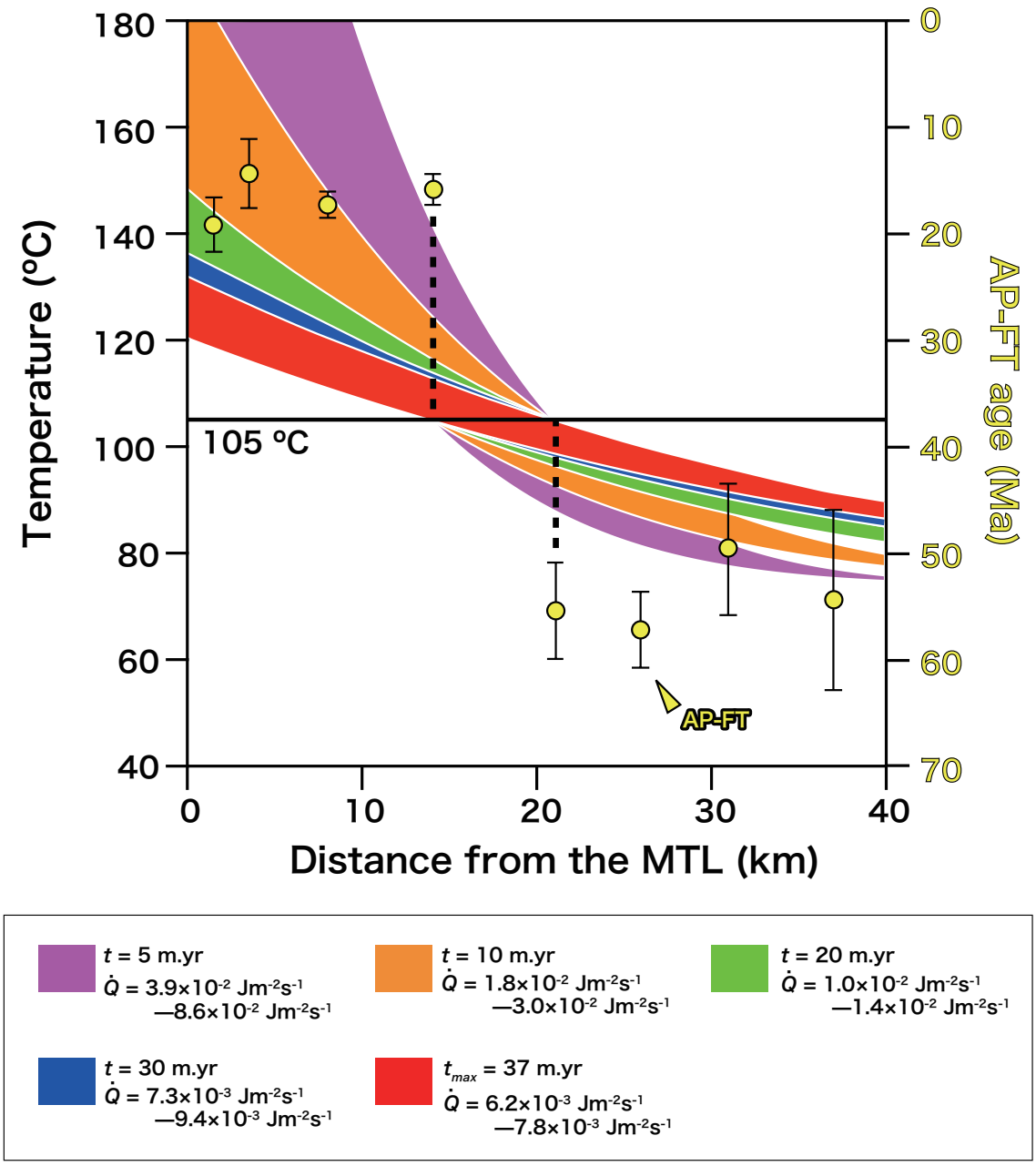

Figure 2. Temperature (left vertical axis) versus distance from the fault derived using equation (5) compared to apatite fission track ages (right vertical axis) given by Tagami et al. [1988] for the RC-traverse. The location of the RC-traverse is shown in Figure 1 with a star. Yellow circles are plots of fission track ages with 1σ error bars from Tagami et al. [1988]. Filled colored areas of temperature distributions show the calculation results compatible with temperatures above 105°C in the area with young apatite fission track ages and below 105 ºC in the area with old apatite fission track ages.

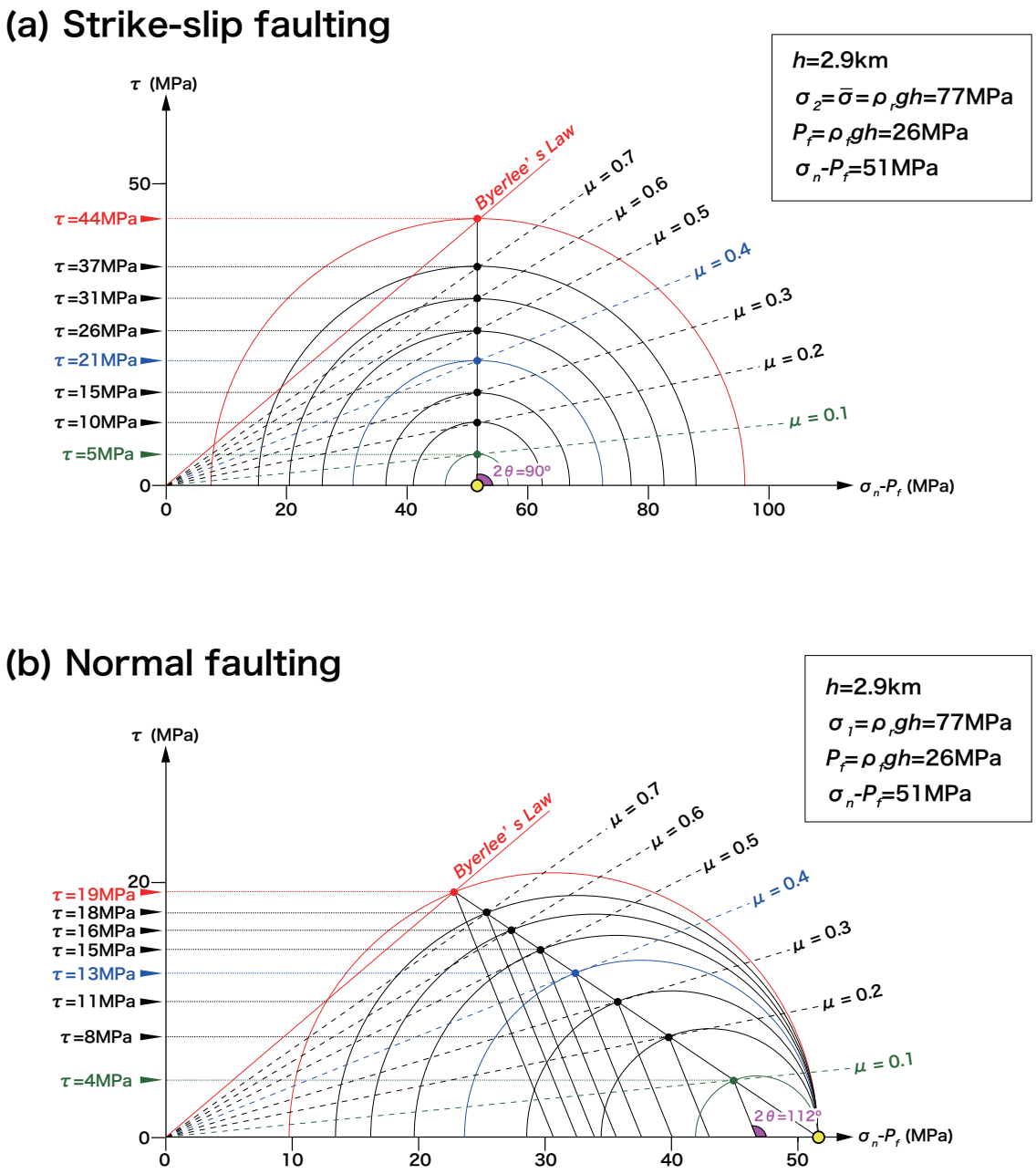

Figure 3. Mohr's circle diagrams to estimate relationships between coefficients of friction and shear stresses for calculations. (a) Strike-slip faulting. (b) Normal faulting.

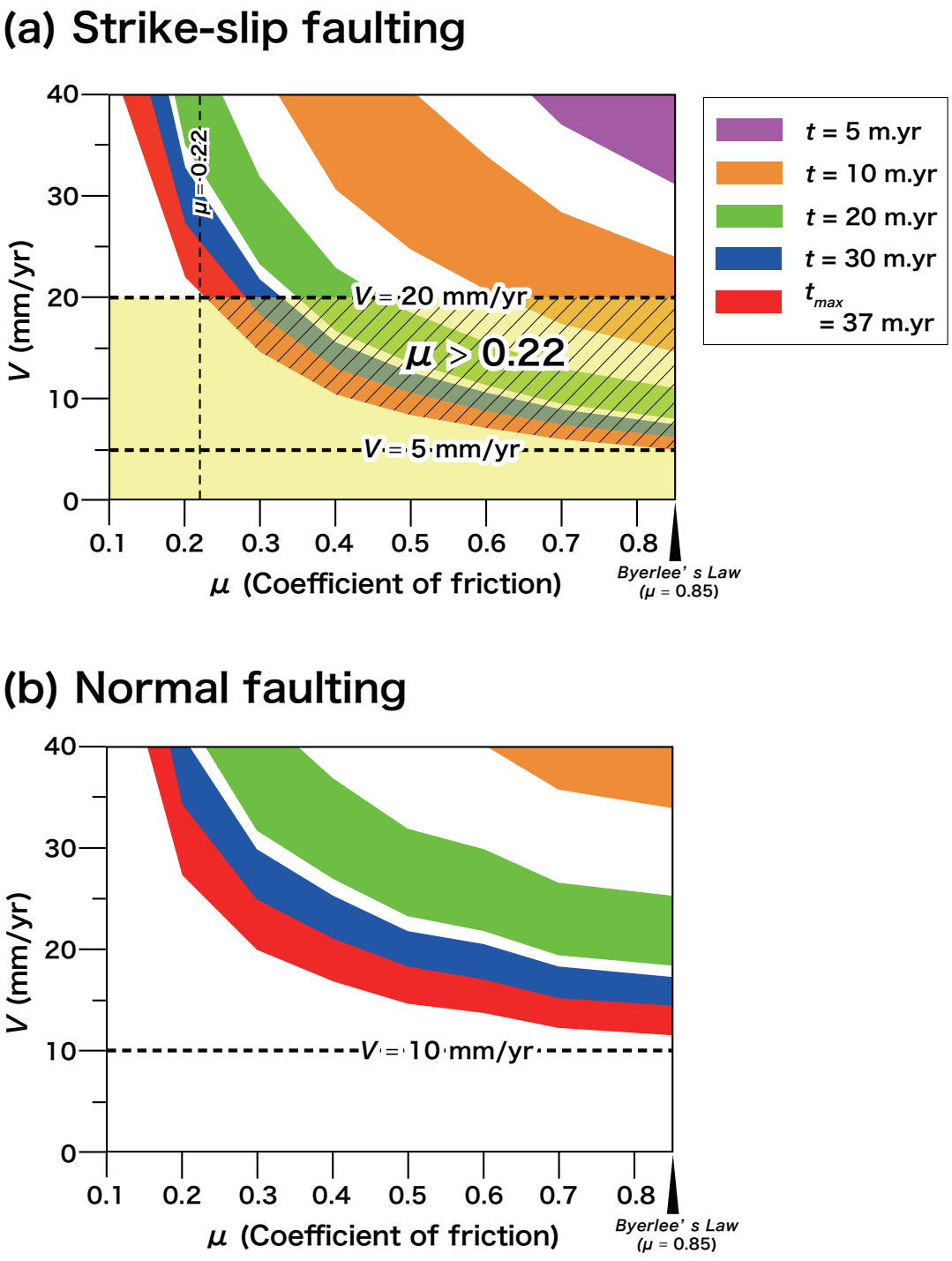

Figure 4. Relationships between μ and V calculated using equation (1) that are required to fit the profiles of Figure 2 in cases of both strike-slip and normal faulting. (a) Profiles for strike-slip faulting. (b) Profiles for normal faulting. Filled colors of the profiles correlate with those of Figure 2. In figure (a), the estimated range of possible slip rates (≤ 20 mm/year) is highlighted by light yellow shading. The intersection between the yellow shading and the curved domains represents the possible conditions of shear heating with an estimated μ greater than 0.22.

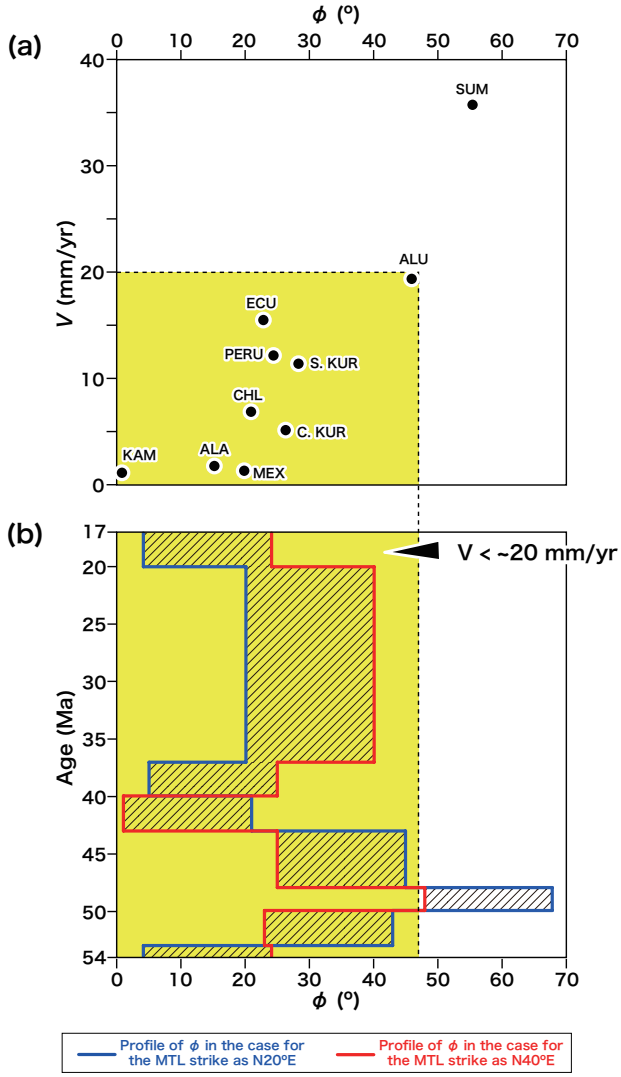

Figure 5. (a) Relationships between average convergent obliquities (φ) and strike-slip rates (V) of their forearc sliver plates modified from Jarrard [1986]. The convergence obliquity (φ) is the angle between convergence direction and the azimuth perpendicular to the arc. Strike-slip rates (V) are estimated from slip vector residuals. S. KUR, South Kurile; C. KUR, Central Kurile; KAM, North Kurile and Kamchatka; ALU, Aleutians; ALA, Alaska Peninsula; MEX, Mexico; ECU, Ecuador and Colombia; PERU, Peru; CHL, Chile; SUM, Sumatra. (b) Reconstructed obliquities (φ) between the subducted Pacific plate and the MTL during the interval 54 Ma–17 Ma by using the stage poles given in Engerbretson [1985] based on the global circuit of plate motions. The original location of the reference point of the MTL within the RC-traverse prior to the opening of the Japan Sea is taken to be 35ºN 140ºE by using a pole of rotation 34°N 129°E and an anticlockwise rotation angle of ~45° with respect to eastern Asia following Otofuji and Matsuda [1987]. φ is calculated using a strike of MTL of N20ºE (blue line) to N40ºE (red line) for the period 54 Ma–17 Ma [e.g., Hyodo and Niitsuma, 1986; Kinoshita and Ito, 1986; Shimada et al., 1998; Kimura, 1999]. These ranges are shown as shaded areas. Yellow filled areas show ranges of φ for strike-slip rates less than 20 mm/year, which is inferred from the relationships in figure (a).

Table 1. Material parameters and initial conditions for thermal calculations.

c	Specific heat	1000	$Jkg^{-1}K^{-1}$
$\kappa = k/c\rho_r$	Thermal diffusivity	9.3×10^{-7}	m^2s^{-1}
k	Thermal conductivity	2.5	$Wm^{-1}K^{-1}$
ρ_r	Density of rock	2700	kgm^{-3}
ρ_f	Density of fluid	1000	kgm^{-3}
G	Geothermal gradient	25	$°Ckm^{-1}$
g	Gravity	9.8	$kgms^{-2}$
e	Proportion of total work converted into heat	0.9	

ACKNOWLEDGMENTS

I am very grateful to Prof. S. Wallis for his abundant advice and assistance on this study. This work also benefited from discussions with Prof. M. Enami, Prof. M. Takeuchi, Dr. S. Shirono, and Dr. T. Terakawa. I am indebted to Prof. K. Fujimoto, Dr. N. Shigematsu for their help with borehole core analysis and discussions in Parts 2 and 3. I am also grateful to Dr. Y. Kouketsu for her constructive help with Raman spectral analyses in Part 2. Thanks are also due to Dr. S. Endo and Dr. M. Aoya for their useful suggestions and encouragements. I am grateful for invaluable help on many occasions to the members of petrology group at Nagoya University. I gratefully acknowledges the assistance of M. Kawahara, residents of Motoyama-town and of Iitaka-town during the field survey in Parts 1 and 2. This work was supported financially in part by Research Fellowship for Young Scientists (Mori: 23•3073) and for Grants-in-Aid for Scientific Research (Fujimoto: 20340136) from the Japan Society for the Promotion of Science, and by a grant from the Fukada Geological Institute.

REFERENCES

Agar, S. M. (1990), The interaction of fluid processes and progressive deformation during shallow level accretion: Examples from the Shimanto Belt of SW Japan, *J. Geophys. Res.,* 95(B6), 9133–9147, doi: 10.1029/JB095iB06p09133.

Aoki, K., K. Kitajima, H. Masago *et. al*. (2009), Metamorphic *P*-*T*-time history of the Sanbagawa belt in central Shikoku, Japan and implications for retrograde metamorphism during exhumation, *Lithos*, *113*(3-4), 393–407, doi:10.1016/j.lithos.2009.04.033.

Aoya, M. (2001), *P*-*T*-*D* Path of Eclogite from the Sambagawa Belt Deduced from Combination of Petrological and Microstructural Analyses, *J. Petrol., 42*(7), 1225–1248, doi:10.1093/petrology/42.7.1225.

Aoya, M. (2002), Structural position of the Seba eclogite unit in the Sambagawa Belt: Supporting evidence for an eclogite nappe. *Island Arc, 11*(2), 91–110, doi:10.1046/j.1440-1738.2002.00359.x.

Aoya, M., Y. Kouketsu, S. Endo, H. Shimizu, T. Mizukami, D. Nakamura, and S. Wallis (2010), Extending the applicability of the Raman carbonaceous-material geothermometer using data from contact metamorphic rocks, *J. Metamorph. Geol.*, *28*(9), 895–914, doi:10.1111/j.1525-1314.2010.00896.x.

Argles, T. W., J. P. Platt, and D. J. Waters (1999), Attenuation and excision of a crustal section during extensional exhumation: the Carratraca Massif, Betic Cordillera, southern Spain. *J. Geol. Soc.*, *156*, 149–162, doi:10.1144/gsjgs.156.1.0149.

Banno, S., T. Higashino, M. Otsuki, T. Itaya, and T. Nakajima (1978), Thermal structure of the Sanbagawa metamorphic belt in central Shikoku. *Journal of the Physical Earth*, *26*, 345–356.

Beyssac, O., B. Goff, C. Chopin, and J. N. Rouzaud (2002), Raman spectra of carbonaceous material in metasediments: a new geothermometer, *J. Metamorph. Geol.*, *20*(9), 859–871, doi:10.1046/j.1525-1314.2002.00408.x.

Beyssac, O., F. Brunet, J. P. Petitet, B. Goffe, and J. N. Rouzaud (2003), Experimental study of the microtextural and structural transformations of carbonaceous materials under pressure and temperature. *European Journal of Mineralogy*, *15(6)*, 937–951, doi:10.1127/0935-1221/2003/0015-0937.

Brodsky, E. E., and H. Kanamori (2001), Elastohydrodynamic lubrication of faults, *J. Geophys. Res.*, *106*(B8), 16357–16374, doi:10.1029/2001JB000430.

Brown, M. (1998), Unpairing metamorphic belts: P-T paths and a tectonic model for the Ryoke Belt, southwest Japan, *J. Metamorph. Geol.*, *16*(1), 3–22, doi:10.1111/j.1525-1314.1998.00061.x.

Brune, J. N., T. L. Henyey, and R. F. Roy (1969), Heat flow, stress, and rate of slip along the San Andreas fault, California, *J. Geophys. Res.*, *74*(15), 3821–3827, doi:10.1029/JB074i015p03821.

Buck, W. R. (1988), Flexural rotation of normal faults, *Tectonics*, *7*(5), 959–973, doi:10.1029/TC007i005p00959.

Byerlee, J. (1978), Friction of rocks, *Pure Appl. Geophys.*, *116*(4-5), 615–626, doi:10.1007/BF00876528.

Carslaw, H. S., and J. C. Jaeger (1959), *Conduction of heat in solids*, 2nd ed., 510 pp., Oxford Univ. Press, Oxford.

d'Alessio, M. A., A. E. Blythe, and R. Bürgmann (2003), No frictional heat along the San Gabriel fault, California: Evidence from fission-track thermochronology, *Geology*, *31*(6), 541–544, doi:10.1130/0091-7613(2003)031<0541:NFHATS>2.0.CO;2.

Doubrovine, P. V., B. Steinberger, and T. H. Torsvik (2012), Absolute plate motions in a reference frame defined by moving hot spots in the Pacific, Atlantic, and Indian oceans, *J. Geophys. Res*, *117*, B09101, doi:10.1029/2011JB009072

Engerbretson, D. C. (1985), Relative Motions Between Oceanic and Continental Plates in the Pacific Basin, *Geol. Soc. Amer. Spec. Pap.*, 206, 1–60, doi:10.1130/SPE206-p1.

Enami, M., S. R. Wallis, and Y. Banno (1994), Paragenesis of sodic pyroxene-bearing quartz schist: implications for the P-T history of the Sanbagawa belt, *Contrib. Mineral. Petrol.*, *116*(1-2), 182–198, doi:10.1007/BF00310699.

Faure, M. (1983), Eastward ductile shear during the early tectonic phase in the Sanbagawa belt. *J. Geol. Soc. Jpn.*, 89(6), 319–329, doi:10.5575/geosoc.89.319.

Faure, M. (1985), Microtectonic evidence for eastward ductile shear in the Jurassic orogen of S. W. Japan, *J. Struct. Geol.*, *7*(2), 175–186, doi:10.1016/0191-8141(85)90130-0.

Fukunari, T., and S. R. Wallis (2007), Structural evidence for large-scale

top-to-the-north normal displacement along the Median Tectonic Line in southwest Japan, *Island Arc*, *16*(2), 243–261, doi:10.1111/j.1440-1738.2007.00570.x.

Fukunari, T., S. R. Wallis, and T. Tsunogae (2011), Fluid inclusion microthermometry for *P–T* constraints on normal displacement along the Median Tectonic Line in Northern Besshi area, Southwest Japan, *Island Arc*, *20*(3), 426–438, doi:10.1111/j.1440-1738.2011.00778.x.

Green, P.F., I. R. Duddy, A. J. W. Gleadow, P. R. Tingate, and G. M. Laslett (1986), Thermal annealing of fission tracks in apatite: 1. A qualitative description, *Chemical Geology (Isotope Geoscience Section)*, *59*, 237–253, doi:10.1016/0168-9622(86)90074-6.

Hara, I., K. Hide, K. Takeda, E. Tsukuda, and T. Shiota (1977), Tectonic movement in the Sambagawa Belt, *In* HIDE K. *ed., The Sanbagawa Belt*, pp. 307–390, Hiroshima University Press.

Hara, I., T. Shiota, K. Hide *et al*. (1990), Nappe structure of the Sanbagawa belt, *J. Metamorph. Geol.*, *8*(4), 441–456, doi:10.1111/j.1525-1314.1990.tb00630.x.

Hara, I., T. Shiota, K. Hide, K. Kanai, M. Goto, S. Seki, K. Kaikiri, K. Takeda, Y. Hayasaka, T. Miyamoto, Y. Sakurai, and Y. Ohtomo (1992), Tectonic evolution of the Sambagawa schists and its implications in convergent margin processes, *J. Sci. Hiroshima Univ., Ser. C*, *9*, 495–595.

Harms, T. A., and R. Price (1992), The Newport fault: Eocene listric normal faulting, mylonitization, and crustal extension in northeast Washington and northwest Idaho. *Geological Society of America Bulletin*, *104*(6), 745–761, doi:10.1130/0016-7606(1992)104<0745:TNFELN>2.3.CO;2.

Harrison, T. M., and I. McDougall (1980), Investigations of an intrusive contact, northwest Nelson, New Zealand, 1, Thermal, chronological and isotopic constraints, *Geochim. Cosmochim. Acta.*, *44*, 1985–2003, doi:10.1016/0016-7037(80)90198-2.

Hide, K. (1954), Geological structure of the Shirataki mining district, Kochi Prefecture, *Geological report of the Hiroshima University*, *4*, 47–83.

Hide, K. (1961), Geologic structure and metamorphism of the Sanbagawa crystalline schists of the Bessi-Shirataki mining district in Shikoku, southwest Japan, *Geological report of the Hiroshima University*, *9*, 1–87.

Higashino, T. (1990), The higher grade metamorphic zonation of the Sambagawa metamorphic belt in central Shikoku, Japan, *J. Metamorph. Geol.*, *8*(4), 413–423, doi:10.1111/j.1525-1314.1990.tb00628.x.

Hodges, K., S. Bowring, K. Davidek, D. Hawkins, and M. Krol (1998), Evidence for rapid displacement on Himalayan normal faults and the importance of tectonic denudation in the evolution of mountain ranges, *Geology*, 26(6), 483–486, doi:10.1130/0091-7613(1998)026<0483:EFRDOH>2.3.CO;2.

Holdsworth, R. E. (2004), Weak Faults--Rotten Cores, *Science*, *303*(5655), 181, doi:10.1126/science.1092491.

Hurford, A. J. (1986), Cooling and uplift patterns in the Lepontine Alps South Central Switzerland and an age of vertical movement on the Insubric fault line, *Contrib. Mineral. Petrol.*, *92*(4), 413–427, doi:10.1007/BF00374424.

Huzita, K. (1980), Role of the Median Tectonic Line in the Quaternary tectonics of the Japanese Islands, *Mem. Geol. Soc. Jpn.*, *18*, 129–153.

Hyodo, H., and N. Niitsuma (1986), Tectonic Rotation of the Kanto Mountains, Related with the Opening of the Japan Sea and Collision of the Tanzawa Block since Middle Miocene, *J. Geomagn. Geoelectr.*, 38(5), 335–348, doi:10.5636/jgg.38.335.

Ichikawa, K. (1980), Geohistory of the Median Tectonic Line of Southwest Japan, *Mem. Geol. Soc. Jpn.*, *18*, 187–212.

Imber, J., R. E. Holdsworth, S. A. F. Smith, S. P. Jefferies, and C. Collettini (2008), Frictional-viscous flow, seismicity and the geology of weak faults: a review and future directions, *Geol. Soc. Spec. Publ.*, *299*, 151–173, doi:10.1144/SP299.10.

Isozaki, Y. (1996), Anatomy and genesis of a subduction-related orogen: A new view of geotectonic subdivision and evolution of the Japanese Islands, *Island Arc*, *5*(3), 289–320, doi:10.1111/j.1440-1738.1996.tb00033.x.

Isozaki, Y., and T. Itaya (1990), Chronology of Sanbagawa metamorphism, *J. Metamorph. Geol.*, *8*(4), 401–411, doi:10.1111/j.1525-1314.1990.tb00627.x.

Isozaki, Y., S. Maruyama, and F. Furuoka (1990), Accreted oceanic materials in Japan, *Tectonophysics*, *181*(1-4), 179–205, doi:10.1016/0040-1951(90)90016-2.

Itaya, T., and H. Takasugi (1988), Muscovite K-Ar ages of the Sanbagawa schists, Japan and argon depletion during cooling and deformation, *Contrib. Mineral. Petrol.*, *100*(3), 281–290, doi:10.1007/BF00379739.

Jarrard, R. D. (1986), Relations among subduction parameters, *Rev. Geophys.*, *24*(2), 217–284, doi:10.1029/RG024i002p00217.

Jefferies, S. P., R. E. Holdsworth, T. Shimamoto, H. Takagi, G. E. Lloyd, and C. J. Spiers (2006a), Origin and mechanical significance of foliated cataclastic rocks in the cores of crustal-scale faults: Examples from the Median Tectonic Line, Japan, *J. Geophys. Res.*, *111*, B12303, doi:10.1029/2005JB004205.

Jefferies, S. P., R. E. Holdsworth, C. A. J. Wibberley, T. Shimamoto, C. J. Spiers, A. R. Niemeijer, and G. E. Lloyd (2006b), The nature and importance of phyllonite development in crustal-scale fault cores: an example from the Median Tectonic Line, Japan, *J. Struct. Geol.*, *28*(2), 220–235, doi:10.1016/j.jsg.2005.10.008.

Johnston, D. C., and S. H. White (1983), Shear heating associated with movement along the Alpine Fault, New Zealand, *Tectonophysics*, *92*(1-3), 241–252, doi:10.1016/0040-1951(83)90092-6.

Katagiri, G., H. Ishida, and A. Ishitani (1988), Raman spectra of graphite edge planes, *Carbon*, *26(4)*, 565–571, doi:10.1016/0008-6223(88)90157-1.

Kawachi, Y. (1968), Large-scale overturned structure in the Sanbagawa metamorphic zone in central Shikoku. *J. Geol. Soc. Jpn.*, *74*(12), 607–616.

Kimura, K. (1999), The slip direction of thrust faults : A case study from a chert-clastic sequence in the Mino-Tamba Belt, central Japan, *J. Geol. Soc. Jpn.*, *105*(3), 208–226.

Kinoshita, O., and H. Ito (1986), Migration of Cretaceous igneous activity in Southwest Japan related to ridge subduction, *J. Geol. Soc. Jpn.*, *92*(10), 723–735.

Kojima, G., and T. Suzuki (1958), Rock structure and quartz fabric in a thrusting shear zone; the Kiyomizu tectonic zone in Shikoku, Japanl, *Journal of Science of the Hiroshima University* (*Series C*), *2*, 173–193.

Kubota, Y., and T. Takeshita (2008), Paleocene large-scale normal faulting along the Median Tectonic Line, western Shikoku, Japan, *Island Arc*, *17*(1), 129–151, doi:10.1111/j.1440-1738.2007.00607.x.

Lachenbruch, A. H., and J. H. Sass (1980), Heat Flow and Energetics of the San Andreas Fault Zone, *J. Geophys. Res.*, *85*(B11), 6185–6222, doi:10.1029/JB085iB11p06185.

Lahfid, A., O. Beyssac, E. Deville, F. Negro, C. Chopin, and B. Goffé (2010), Evolution of the Raman spectrum of carbonaceous material in low-grade

metasediments of the Glarus Alps (Switzerland), *Terra Nova*, *22*(5), 354–360, doi:10.1111/j.1365-3121.2010.00956.x.

Lockner, D. A., and P. G. Okubo (1983), Measurements of Frictional Heating in Granite, *J. Geophys. Res.*, *88*(B5), 4313–4320, doi:10.1029/JB088iB05p04313.

Maruyama, S., J. Liou, and M. Terabayashi (1996), Blueschists and eclogites of the world and their exhumation, *Int. Geol. Rev.*, *38*(6), 485–594, doi:10.1080/00206819709465347.

Melosh, H. J. (1996), Dynamical weakening of faults by acoustic fluidization, *Nature*, *379*(6566), 601–606, doi:10.1038/379601a0.

Miyashiro, A. (1961), Evolution of metamorphic belts, *J. Petrol.*, *2*(3), 277–311, doi:10.1093/petrology/2.3.277.

Miyashiro, A. (1972), Metamorphism and related magmatism in plate tectonics, *Am. J. Sci.*, *272*(7), 629–656, 10.2475/ajs.272.7.629.

Miyashiro, A. (1973), Paired and unpaired metamorphic belts, *Tectonophysics*, *17*(3), 241–254, doi:10.1016/0040-1951(73)90005-X.

Miyata, T., H. Ui, and K. Ichikawa (1980), Paleogene left-lateral wrenching on the Median Tectonic Line in southwest Japan, *Mem. Geol. Soc. Jpn.*, *18*, 51–68.

Mizukami, T., and S. R. Wallis (2005), Structural and petrological constraints on the tectonic evolution of the garnet-lherzolite facies Higashi-akaishi peridotite body, Sanbagawa belt, SW Japan, *Tectonics*, *24*(6), TC6012, doi:10.1029/2004TC001733.

Molnar, P., and P. England (1990), Temperatures, heat flux, and frictional stress near major thrust faults, *J. Geophys. Res.*, *95*(B4), 4833–4856, doi:10.1029/JB095iB04p04833.

Moore, D. E., and M. J. Rymer (2007), Talc-bearing serpentinite and the creeping section of the San Andreas fault, *Nature*, *448*(7155), 795–797, doi:10.1038/nature06064.

Nakajima, T. (1994), The Ryoke plutonometamorphic belt: crustal section of the Cretaceous Eurasian continental margin, *Lithos*, *33*(1-3), 51–66, doi:10.1016/0024-4937(94)90053-1.

O'Hara, K. (2004), Paleo-stress estimates on ancient seismogenic faults based on frictional heating of coal, *Geophys. Res. Lett.*, *31*(3), L03601, doi:10.1029/2003GL018890.

Okada, A. (1980), Quaternary faulting along the Median Tectonic Line of southwest Japan, *Mem. Geol. Soc. Jpn.*, *18*, 79–108.

Okamoto, K., S. Maruyama, and Y. Isozaki (2000), Accretionary complex origin of the Sanbagawa, high P/T metamorphic rocks, central Shikoku, Japan – layer parallel shortening structure and green stone geochemistry, *J. Geol. Soc. Jpn.*, *106*(1), 70–86.

Okudaira, T., and N. Shigematsu (2012), Estimates of stress and strain rate in mylonites based on the boundary between the fields of grain-size sensitive and insensitive creep, *J. Geophys. Res.*, *117*, B03210, doi:10.1029/2011JB008799.

O'Neil, J. R., and T. C. Hanks (1980), Geochemical Evidence for Water-Rock Interaction Along the San Andreas and Gatlock Faults of California, *J. Geophys. Res.*, *85*(B11), 6286–6292, doi:10.1029/JB085iB11p06286.

Osozawa, S., and T. Pavlis (2007), The high *P/T* Sambagawa extrusional wedge, Japan, *J. Struct. Geol.*, *29*(7), 1131–1147, doi:10.1016/j.jsg.2007.03.014.

Ota, T., M. Terabayashi, and I. Katayama (2004), Thermobaric structure and metamorphic evolution of the Iratsu eclogite body in the Sanbagawa belt, central Shikoku, Japan, *Lithos*, *73*(1-2), 95–126, doi:10.1016/j.lithos.2004.01.001.

Otofuji, Y., and T. Matsuda (1987), Amount of clockwise rotation of Southwest Japan —fan shape opening of the southwestern part of the Japan Sea, *Earth Planet. Sci. Lett.*, 85(1-3), 289–301, doi:10.1016/0012-821X(87)90039-2.

Otsuki, K. (1978), On the relationship between the width of shear zone and the displacement along fault, *J. Geol. Soc. Jpn*., *84*(11), 661–669, doi:10.5575/geosoc.84.661.

Rahl, J. M., K. M. Anderson, M. T. Brandon, and C. Fassoulas (2005), Raman spectroscopic carbonaceous material thermometry of low-grade metamorphic rocks: calibration and application to tectonic exhumation in Crete, Greece, *Earth Planet. Sci. Lett.*, *240*(2), 339–354, doi:10.1016/j.epsl.2005.09.055.

Ramsay, J. G., M. Casey, and R. Klingfeld (1983), Role of shear in development of the Helvetic fold-thrust belt of Switzerland, *Geology*, *11*(8), 439–442, doi:10.1130/0091-7613(1983)11<439:ROSIDO>2.0.CO;2.

Rice, J. R. (1992), Fault stress states, pore pressure distributions, and the weakness of the San Andreas fault, in *Fault Mechanics and Transport Properties of Rocks*, edited by B. Evans and T. -F. Wong, pp. 475–503, Elsevier, New York.

Sakaguchi, A., F. Chester, D. Curewitz, O. Fabbri, D. Goldsby, G. Kimura, C. Li, Y. Masaki, E. J. Screaton, A. Tsutsumi, K. Ujiie, and A. Yamaguchi (2011), Seismic slip propagation to the updip end of plate boundary subduction interface faults: Vitrinite reflectance geothermometry on Integrated Ocean Drilling Program NanTro SEIZE cores, *Geology*, *39*(4), 395–398, doi:10.1130/G31642.1.

Scholz, C. H. (1980), Shear heating and the state of stress on faults, *J. Geophys. Res.*, *85*(B11), 6174–6184, doi: 10.1029/JB085iB11p06174.

Scholz, C. H. (2000), Evidence for a strong San Andreas fault, *Geology*, *28*(2), 163–166, doi:10.1130/0091-7613(2000)28<163:EFASSA>2.0.CO;2.

Scholz, C. H., J. Beavan, and T. C. Hanks (1979), Frictional metamorphism, argon depletion, and tectonic stress on the Alpine Fault, New Zealand, *J. Geophys. Res.*, *84*(12), 6770–6782, doi:10.1029/JB084iB12p06770.

Scholz, C. H., N. H. Dawers, J. Z. Yu, M. H. Anders, and P. A. Cowie (1993), Fault growth and fault scaling laws: preliminary results, *J. Geophys. Res.*, *98*(B12), 21951–21961, doi:10.1029/93JB01008.

Shigematsu, N., N. Koizumi, K. Fujimoto, N. Furuya, N. Tanaka, T. Takeshita, H. Mori, S. Wallis, and N. Kimura, (2009), Drilling of the Median Tectonic Line and the analysis of the internal structure of the fault zone using the borehole core, *Chishitsu News*, *662*, 16–22.

Shigematsu, N., K. Fujimoto, N. Tanaka, N. Furuya, H. Mori, and S. Wallis (2012), Internal structure of the Median Tectonic Line fault zone, SW Japan, revealed by borehole analysis, *Tectonophysics*, *532–535*, 103–118, doi:10.1016/j.tecto.2012.01.024.

Shimada, K., H. Takagi, and H. Osawa (1998), Geotectonic evolution in transpressional regime: time and space relationships between mylonitization and folding in the southern Ryoke belt, eastern Kii Peninsula, southwest Japan, *J. Geol. Soc. Jpn.*, *104*(12), 825–844, doi:10.5575/geosoc.116.45.

Shiota, T. (1991), Nappe Structure of the Sambagawa Belt in the Mt. Shiraga District, Central Shikoku, *Natural science research, Faculty of Integrated Arts and Sciences, the University of Tokushima*, *4*, 29–44.

Sibson, R. H. (1973), Interactions between temperature and pore-fluid pressure during earthquake faulting and a mechanism for partial or total stress relief, *Nature*, *243*(126), 66–68, doi:10.1038/physci243066a0.

Sueoka, S., B. P. Kohn, Y. Ikeda, K. Kano, H. Tsutsumi, and T. Tagami (2011), Uplift and Denudation History of the Akaishi Range Based on Low-temperature Thermochronologic Methods, Chigaku Zasshi, 120(6), 1003–1012, doi:10.5026/jgeography.120.1003.

Sueoka, S., B. P. Kohn, T. Tagami, H. Tsutsumi, N. Hasebe, A. Tamura, and S. Arai (2012), Denudation history of the Kiso Range, central Japan, and its tectonic implications: Constraints from low-temperature thermochronology, Island Arc, 21(1), 32–52, doi:10.1111/j.1440-1738.2011.00789.x.

Suzuki, K., and M. Adachi (1998), Denudation history of the high *T/P* Ryoke metamorphic belt, southwest Japan: constraints from CHIME monazite ages of gneisses and granitoids, *J. Metamorph. Geol.*, *16*(1), 23–37, doi:10.1111/j.1525-1314.1998.00057.x.

Tabei, T., M. Hashimoto, S. Miyazaki, K. Hirahara, F. Kimata, T. Matsushima, T. Tanaka, Y. Eguchi, T. Takaya, and Y. Hoso (2002), Subsurface structure and faulting of the Median Tectonic Line, southwest Japan inferred from GPS velocity field, *Earth, Planets Space*, *54*(11), 1065–1070.

Tabei, T., M. Hashimoto, S. Miyazaki, and Y. Ohta (2003), Present-day deformation across the southwest Japan arc: Oblique subduction of the Philippine Sea plate and lateral slip of the Nankai forearc, *Earth, Planets Space*, *55*(10), 643–647.

Tagami, T. (2012), Thermochronological investigation of fault zones, *Tectonophysics*, *538–540*, 67–85, doi:10.1016/j.tecto.2012.01.032.

Tagami, T., N. Lal, R. B. Sorkhabi, and S. Nishimura (1988), Fission track thermochronologic analysis of the Ryoke belt and the Median Tectonic Line, Southwest Japan, *J. Geophys. Res.*, *93*(B11), 13705–13715, doi:10.1029/JB093iB11p13705.

Takagi, H. (1986), Implications of mylonitic microstructures for the geotectonic evolution of the Median Tectonic Line, central Japan, *J. Struct. Geol.*, *8*(1), 3–14, doi:10.1016/0191-8141(86)90013-1.

Takagi, H., H. Takeshita, K. Shibata, S. Uchiumi, and M. Inoue (1992), Middle Miocene normal faulting along the Tobe Thrust in western Shikoku. *J. Geol. Soc. Jpn.*, *98*(11), 1069–1072, doi:10.5575/geosoc.98.1069.

Takahashi, M., H. Hayashi, K. Kasahara, and H. Kimura (2006), Geologic interpretation of the seismic reflection profile along the western margin of Kanto Plain-With

special reference to the Yoshimi metamorphic rocks and western extension of the Tonegawa Tectonic Line. *J. Geol. Soc. Jpn.*, *112*(1), 33–52, doi:10.5575/geosoc.112.33.

Takasu, A. (1989), *P-T* histories of peridotite and amphibolite tectonic blocks in the Sanbagawa metamorphic belt, Japan, *In* Daly J.S., Cliff R.A. & Yardley B.W. (eds), Evolution of Metamorphic Belts. *Geol. Soc. London, Spec. Publ.*, *43*, 533–538, doi:10.1144/GSL.SP.1989.043.01.51.

Takasu, A., and R. D. Dallmeyer (1990), $^{40}Ar/^{39}Ar$ mineral age constraints for the tectonothermal evolution of the Sambagawa metamorphic belt, central Shikoku, Japan: a Cretaceous accretionary prism, *Tectonophysics*, *185*(1-2), 111–139, doi:10.1016/0040-1951(90)90408-Z.

Takasu, A., S. R. Wallis, S. Banno, and R. D. Dallmeyer (1994), Evolution of the Sambagawa metamorphic belt, Japan, *Lithos*, *33*(1-3), 119–133, doi:10.1016/0024-4937(94)90057-4.

Takeshita, T., and K. Yagi (2004), Flow patterns during exhumation of the Sambagawa metamorphic rocks, SW Japan, caused by brittle-ductile, arc-parallel extension, in *Vertical Coupling and Decoupling in the Lithosphere*, edited by J. Grocott, K. J. W. McCaffrey, G. Taylor, and B. Tikoff, *Geol. Soc. Spec. Publ.*, *227*, 279–296, doi:10.1144/GSL.SP.2004.227.01.14.

Takeuchi, M. (1996), Geology of the Sanbagawa, Chichibu and Shimanto Belts in the Kii peninsula: Yoshino area in Nara prefecture and Kushidagawa area in Mie prefecture, *Bulletin of the Geological Survey of Japan*, *47*(4), 223–244.

Wallis, S. R. (1990), The timing of folding and stretching in the Sanbagawa belt, the Asemigawa region, central Shikoku, *J. Geol. Soc. Jpn.*, *96*(5), 345–352, doi:10.5575/geosoc.96.345.

Wallis, S. R. (1998), Exhuming the Sanbagawa metamorphic belt: the importance of tectonic discontinuities, *J. Metamorph. Geol.*, *16*(1), 83–95, doi:10.1111/j.1525-1314.1998.00072.x.

Wallis, S. R., R. Anczkiewicz, S. Endo, M. Aoya, J. P. Platt, M. Thirlwall, and T. Hirata (2009), Plate movements, ductile deformation and geochronology of the Sanbagawa belt, SW Japan: tectonic significance of 89–88 Ma Lu–Hf eclogite ages, *J. Metamorph. Geol.*, *27*(2), 93–105, doi:10.1111/j.1525-1314.2008.00806.x.

Wallis, S. R., S. Banno, and M. Radvanec (1992), Kinematics, structure and relationship to metamorphism of the east-west flow in the Sanbagawa Belt, southwest Japan, *Island Arc*, *1*(1), 176–185, doi:10.1111/j.1440-1738.1992.tb00068.x.

Wallis, S., Y. Moriyama, and T. Tagami (2004), Exhumation rates and age of metamorphism in the Sanbagawa belt: new constraints from zircon fission track analysis, *J. Metamorph. Geol.*, *22*(1), 17–24, doi:10.1111/j.1525-1314.2003.00493.x.

Wang, A., P. Dhamenincourt, J. Dubessy, D. Guerard, P. Landais, and M. Lelaurain (1989), Characterization of graphite alteration in an uranium deposit by micro-Raman spectroscopy, X-ray diffraction, transmission electron microscopy and scanning electron microscopy, *Carbon*, *27*(2), 209–218, doi:10.1016/0008-6223(89)90125-5.

Weijermars, R. (1985), Mapping of major fold closures from minor structures; a review of the relative merits of vergence, facing and S-Z concepts, *Geol. Rundsc.*, *74*(3), 611–622, doi:10.1007/BF01821216.

Wibberley, C. A. J., and T. Shimamoto (2003), Internal structure and permeability of major strike-slip fault zones: the Median Tectonic Line in Mie Prefecture, Southwest Japan, *J. Struct. Geol.*, *25*(1), 59–78, doi:10.1016/S0191-8141(02)00014-7.

Wibberley, C. A. J., and T. Shimamoto (2005), Earthquake slip weakening and asperities explained by thermal pressurization, *Nature*, *436*, 689–692, doi:10.1038/nature03901.

Williams, C. F., and T. N. Narasimhan (1989), Hydrogeologic constraints on heat flow along the San Andreas fault: A testing of hypotheses, *Earth Planet. Sci. Lett.*, *92*(2), 131–143, doi:10.1016/0012-821X(89)90041-1.

Yamada, R., T. Matsuda, and K. Omura (2007), Apatite and zircon fission-track dating from the Hirabayashi-NIED borehole, Nojima Fault, Japan: Evidence for anomalous heating in fracture zones, *Tectonophysics*, *443*(3-4), 153–160, doi:10.1016/j.tecto.2007.01.014.

Yamaguchi, K., N. Kano, and N. Koizumi (2009), Surveys of the subsurface structure around the integrated groundwater observation stations, *Chishitsu News*, *662*, 23-31.

Yamamoto, H., K. Okamoto, Y. Kaneko, and M. Terabayashi (2004), Southward extrusion of eclogite-bearing mafic-ultramafic bodies in the Sanbagawa belt, central Shikoku, Japan, *Tectonophysics*, *387*(1-4), 151–168, doi:10.1016/j.tecto.2004.06.014.